presented by

Dipl.–Phys. Juan José Gracia Calvo

born in Freiburg, Germany

Oral examination: 17th of July, 2002

Time-dependent Accretion Flows
onto Black Holes

Referees:　　　　　Prof. Dr. Max Camenzind

　　　　　　　　　Prof. Dr. Wilhelm Kley

Zusammenfassung

Akkretion spielt in einer Reihe von astrophysikalischen Systemen, wie Aktive galaktische Kerne (AGN) und Röntgenbinärsystemen (BHXB), eine entscheidende Rolle. Das Standardscheiben Modell kann die beobachteten Spektren dieser Objekte nicht befriedigend erklären. Sie weisen außer einer Schwarzkörperkomponente, die allgemein der Standardscheibe zugeschrieben wird, noch eine weitere harte Komponente auf, die einem Potenzgesetz folgt. Diese letztere wird dadurch erklärt, daß sich in unmittelbarer Nähe der Standardscheibe heißes, optisch dünnes Gas befindet, welches durch radiale Advektion statt durch Strahlungsprozesse kühlt.

Diese Arbeit geht der Frage nach, ob eine innere optisch dünne Scheibe selbstkonsistent radial an eine außenliegende Standardscheibe angeschlossen werden kann. Ein erstes Resultat ist, daß dies in der Tat prinzipiell für einen weiten Bereich von Übergangsradien möglich ist. Allerdings entwickelt sich der Akkretionfluss so, daß der Übergangsradius langsam auswärts driftet, bis dieser ein Maximum erreicht, welches in Übereinstimmung mit vorhergehenden stationären Arbeiten ist. Als weiteres wichtiges Ergebnis findet man, daß der Übergangsbereich instabil ist. Oszillierende Moden von Rayleigh-Instabilitäten dringen in die heiße Scheibe ein, so daß hydrodynamische Größen, ebenso wie das resultierende Spektrum, hochvariabel sind. Die charakteristische Frequenz der Oszillationen ist von der Größenordnung der Keplerschen Umlauffrequenz und macht diese somit zu einem möglichen Kandidaten zur Erklärung der quasi-periodischen Oszillationen, welche man in den Lichtkurven einiger BHXBs beobachtet.

Abstract

Accretion onto compact objects play a fundamental role in a number of astrophysical systems like active galactic nuclei (AGN) and black hole X-ray binaries (BHXB). The standard thin disk model fails to reproduce the spectra of these systems. They exhibit a blackbody-like component, generally attributed to the cold standard disk, and a hard power law-like component extending to several $100\,\mathrm{keV}$, which cannot be accounted for by the standard disk. This situation can be remedied by assuming that the accretion flow consists not only of the cold standard disk, but also of a hot optically thin plasma in the immediate vicinity. This hot flow cools through advection rather than through radiation.

This work addresses the question whether an inner hot optically thin disk can be self-consistently connected to an outer cold standard disk. We come to the conclusion that radial transitions between the two flow types are in principle possible for a wide range of transition radii, which depend on the flow parameters. But while the flow evolves in time, the transition radius drifts radially outward until this reaches its outermost allowed location, which is in agrement with previous steady models. A second major result is, that the transition region is highly unstable. Oscillating modes of the Rayleigh-instability leak into the inner hot flow and make its hydrodynamical and spectral properties highly variable. The characteristic frequency of the oscillations is near to the local keplerian orbital frequency, which makes them a potential candidate for the high-frequency quasi-periodic oscillations present in the X-ray light-curves of BHXB's.

La inspiración existe,

pero tiene que encontrarte trabajando.

Pablo Ruiz Picasso

Contents

Chapter 1

Introduction

Accretion onto a central object is believed to be one of the most effective energy release mechanisms in astrophysics. Ambient matter is thereby captured by a gravitating body out of the surrounding medium. On the way down the gravitational potential of the central object matter is compressed and possibly sheared, which leads to heating through dissipative processes. If the central object is a compact object, like a neutron star or a black hole, a large fraction of the infalling rest mass energy equivalence will be transfered to heat and eventually radiated away with an efficiency $\eta = L/\dot{M}c^2$, where L is the radiative luminosity, $\dot{M}$ the rate by which mass is accreted and c the speed of light.

At high luminosities, the flow and particularly the accretion rate will be controlled by the outward momentum transfered from the radiation to the accreting matter by scattering and absorption. A fundamental upper limit for the radiative luminosity of steady spherical accretion flows is the Eddington luminosity, L_{Edd}, which results from the equilibrium between outward oriented radiation pressure and inward oriented gravitational force. The corresponding Eddington accretion rate is (e.g. Frank et al., 1985)

$$\dot{M}_{Edd} = 1.39 \times 10^{18} \left(\frac{M}{M_\odot} \right) \mathrm{g\,s^{-1}} = 2.09 \times 10^{-8} \left(\frac{M}{M_\odot} \right) \mathrm{M_\odot\,yr^{-1}}, \qquad (1.1)$$

where a constant radiation efficiency $\eta = 1/10$ has been assumed.

In the case of a maximally rotating black hole, the efficiency can be up to $\eta = 0.42$, whereas nuclear fission releases only an relative small fraction $\eta \sim 0.01$ of the energy. It is therefore a widely accepted paradigm that active galactic nuclei (hereafter AGN) harbor supermassive black hole as their central engine. Even our quiet and normal own galaxy has such a black hole with mass $M = 2.6 \times 10^6 M_\odot$ (Eckart and Genzel, 1997). There is now also solid evidence for the presence of black holes in a number of X-ray binaries (see de Zeeuw, 2001, for a review). The spectra we observe from such objects is ultimately reprocessed radiation from the powering accretion disk.

An accretion disk is an integral part of a number of astrophysical objects. Some kind of accretion disk will emerge whenever matter with non-negligible
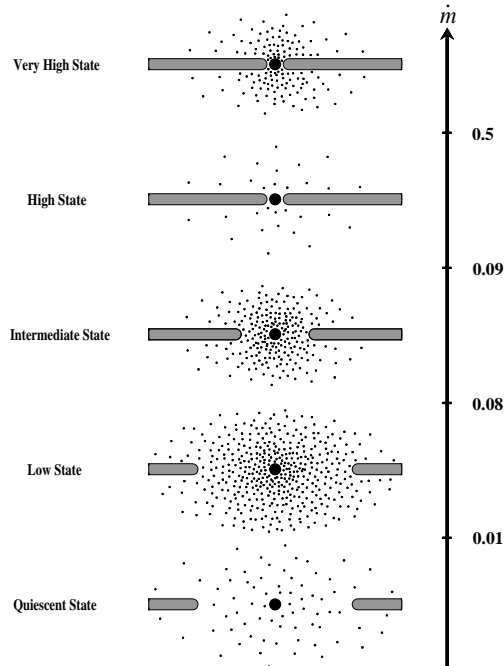
Figure 1.1: Configuration of the accretion flow in different spectral states shown schematically as a function of mass accretion rate $\dot{m}$. The ADAF is indicated by dots and the standard disk by the horizontal bars. The spectral states correspond to a series of increasing accretion rate $\dot{m}$ and simultaneous decreasing of the transition radius from the inner ADAF to the outer standard disk. Figure adopted from Esin et al. (1997).

amounts of angular momentum falls under the influence of a central gravitating body. These objects differ in the nature of the central body, particularly in its mass M. But the underlying physical processes should be very similar. If accretion process is considered from a purely hydrodynamical point of view, the properties of the accretion flow scale with the mass accretion rate $\dot{M}$. They take a very simple form, which is independent of the mass of the central body, if the accretion rate is expressed in units of the Eddington mass accretion rate $\dot{M}_{Edd}$, i.e. $\dot{m} = \dot{M}/\dot{M}_{Edd}$, and all length-scales R_* are expressed in units of the gravitational radius $R_g = GM/c^2$, i.e. $R = R_*/R_g$.

Only by taking into account additional physics, like magnetic fields or detailed radiative transfer, which may not necessarily scale with mass, is the symmetry broken. Nonetheless accretion onto stellar mass black holes should be a good model for the physical processes operating in accretion disk of AGN. The former are easier accessible to observation, both, with respect to the coverage of the continuum spectrum and also with respect to the shorter timescales of variability of the source.

The standard thin disk model proposed by Shakura and Sunyaev (1973) assumes that the half thickness of the disk, H, is small compared to the radius
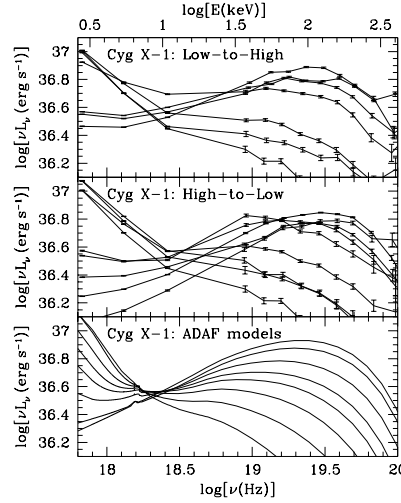
Figure 1.2: Broadband simultaneous RXTE and BATSE spectra of Cyg X-1 observed during its state transition in 1996. The top panel shows the spectra at different times during the low to high transition, the middle panel during the high to low transition. The bottom panel shows a transition sequence predicted by the model of Esin et al. (1997) with a transition radius decreasing monotonically from $100\,R_g$ (upper line at $100\,keV$) to $3\,R_g$ (lower line at $100\,keV$). Figure adopted from Esin et al. (1998).

R, i.e $H/R \ll 1$. This assumption leads to a nearly keplerian angular velocity with a small radial drift superimposed. This assumption is only consistent, if pressure gradients are negligible, such that gravitational and centrifugal forces balance. This in turn means that the temperature of the flow is low and the gas must cool efficiently, e.g. by optically thick blackbody emission. The standard disk has ever since been successfully applied to "high-luminosity-low-energy" systems like proto-stellar disks or cataclysmic variables, but it completely failed to reproduce the high-energy X-ray continuum emission of black hole candidate systems like Cyg X-1. Thorne and Price (1975) demonstrated that the hard spectrum of Cyg X-1 could be explained if the inner part of the accretion disk consisted of a hot, optically thin gas instead of a cold, optically thick gas predicted by the standard disk. This two-zone model has essentially survived to the present day. The originally proposed hot solution of Shapiro et al. (1976) later turned out to be viscously and thermally unstable. It has meanwhile been substituted by the hot advection dominated accretion flow (ADAF) proposed by Narayan and Yi (1995a), Ichimaru (1977) and its relativistic generalization (e.g. Peitz and Appl, 1997). A summary of the properties of the standard disk and some ADAF models will be discussed in chapter 3.

Black hole X-ray binaries (BHXB) are known to exhibit a number of distinct X-ray spectral states (for review see e.g. Tanaka and Shibazaki (1996); Liang (1998)). The *low/hard* state is characterized by a power-law spectrum with an exponential cut-off at $\sim 100\,keV$. The total luminosity is generally below
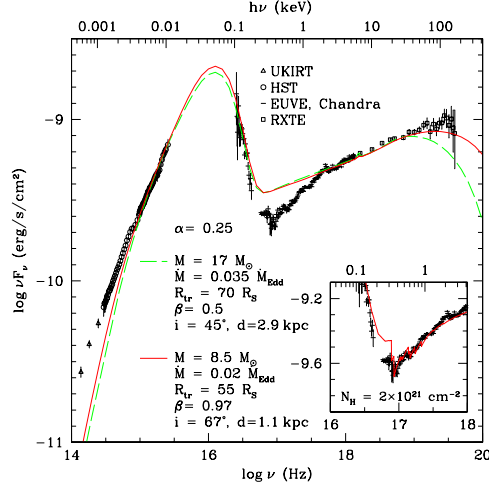
Figure 1.3: Model spectra of the source XTE J1118-480 in the low state for two different sets of parameters. The inset incorporates the effect of a warm absorber. See Esin et al. (2001) for details. Figure adopted from Esin et al. (2001).

$0.1\,L_{Edd}$. In the *high/soft* state the spectrum is dominated by a thermal, soft blackbody component of $\sim 1\,\mathrm{keV}$, whereas the luminosity clearly exceeds that of the *low/hard* state. Additionally a low-luminosity power-law component may be present. The *quiescence/off* state is dominated by a distinctly non-blackbody spectrum with a photon index somewhat lower than in the low state. The luminosity is orders of magnitude lower than in the other states. This state is observed in a sub-class of BHXB, the so called soft X-ray transients (SXT). Some systems (as Cyg X-1) are seen to undergo state transitions forth and back between the low and high state, thereby exhibiting the *intermediate* state. SXT spend most of their time in quiescence, but occasionally undergo wild outbursts to the low and even high state.

Narayan et al. (1996, 1997a) were able to show that the spectra of SXT could be reproduced by a two-zone accretion flow. This consists of an inner optically thin ADAF part, extending from the black hole horizon out to a transition radius at $\sim 10^4\,\mathrm{R_g}$, and an outer thin disk beyond that radius. The accretion rate was estimated to $\dot{m} = 10^{-3}$. Esin et al. (1997) extended the model to higher accretion rates and showed that the other spectral states are naturally explained by the same model. In this model the spectral states of BHXB are identified with a series of increasing mass accretion rate through quiescence, low, intermediate and high state, respectively. Simultaneously the transition radius decreases from $\sim 10^3 - 10^4 \mathrm{R_g}$ down to $\sim 3\mathrm{R_g}$ in the same order, as illustrated in figure 1.1. This model was very successfully applied to the state transitions observed in Cyg X-1. Both high/low and low/high transitions were modeled by a varying mass accretion rate and transition radius as shown in figure 1.2. Meanwhile this model has been extended to include, among others,

the iron fluorescence line Fe K$_\alpha$ and a hot ADAF-like corona above and below the standard disk (see Esin et al., 2001, and references therein). This model reproduces the spectra of BHXB very accurately (e.g. figure 1.3).

While these models work very well, they are not global solutions to an accretion flow. The analytical scaling laws for hot ADAF and standard disk are concatenated at and arbitrary transition radius. They do not include any physical transition mechanism nor any assertion if such a transition is physically possible at this particular radius. The former question has not been widely studied in the literature. It is also not part of this work and will only be briefly touched upon in the final discussion. The latter has been recently addressed by a number of articles Honma (1996); Manmoto et al. (2000); Manmoto and Kato (2000). These authors studied the availability of ADAF-SSD transition models in the steady limit. They identified certain connection conditions that must be satisfied at such a transition and showed that these conditions can be met for a range of flow parameters. Their results are summarized and re-examined in chapters 3 and 5.

This work presents a time-dependent generalization of the steady model of Manmoto and Kato (2000) discussed in chapter 2. Due to the steady nature of their model, Manmoto and Kato could not make any statements concerning the generic time-dependent behavior of ADAF-SSD transition models nor concerning their stability. Both questions are addressed in chapter 6 of this work. A recipe to calculate simple spectra along with the short-comings of this procedure is presented in chapter 7. Finally, we discuss the results and make our conclusion in the final chapter 8.

Chapter 2

Theory of Accretion Flows

In the first part of this chapter we present the general form of a conservation law and apply this to deduce the basic equations of hydrodynamics. The next steps will be to reduce this system to a feasible level by making further assumptions appropriate for accretion flows. We begin with symmetry considerations and vertical integration to reduce the dimension of the problem and the number of independent variables. Next we fill in the missing pieces like external forces, sources and sinks of energy, etc. The inclusion of radiative processes forces us to formulate an additional equation for the radiative energy density u. In the last sections of this chapter we finally formulate the full set of equations and, for clearer notation and easier discussion, its steady limit.

2.1 General conservation laws

The laws of fluid dynamics are well established and can be formulated in many equivalent ways (for an extensive introduction see eg. Landau and Lifshitz, 1959). For instance they can be deduced from the observation that the behavior of a physical system is completely determined by conservation laws. This corresponds to the statement that during the evolution of a fluid a certain number of properties, such as mass, generalized momentum and energy are 'conserved'. In deriving the laws of fluid dynamics we closely follow Hirsch (1988a).

2.1.1 Scalar conservation law

Let us consider a quantity per unit volume U, acting in a volume V with closed surface S. The quantity U varies through the effect of fluxes $\boldsymbol{F}$, which reveal the contributions from the surrounding points, and through sources Q. The flux vector contains two components, a diffusive contribution $\boldsymbol{F}_D$ and a convective part $\boldsymbol{F}_C$. The general form of a conservation law states that the variation per unit time of the quantity U within the volume V

$$\frac{\partial}{\partial t} \int_V U \, dV \tag{2.1}$$

is equal to the net contribution of the incoming fluxes through the surface S

$$-\oint_S \boldsymbol{F} \cdot d\boldsymbol{S} \tag{2.2}$$

plus contributions of the sources Q. These sources can be divided into two classes, volume sources Q_V, acting within the volume V, and surface sources $\boldsymbol{Q}_S$, emanating from the bounding surface S. The contribution to the variation of U is then

$$\int_V Q_V \, dV + \oint_S \boldsymbol{Q}_S \cdot d\boldsymbol{S}, \tag{2.3}$$

where the surface element normal $d\boldsymbol{S}$ points outward.

Collecting terms the general form of the conservation law for the scalar quantity U is

$$\frac{\partial}{\partial t} \int_V U \, dV + \oint_S \boldsymbol{F} \cdot d\boldsymbol{S} = \int_V Q_V \, dV + \oint_S \boldsymbol{Q}_S \cdot d\boldsymbol{S}. \tag{2.4}$$

Employing Gauss's theorem for continuous fluxes and surface sources this yields

$$\frac{\partial}{\partial t} \int_V U \, dV + \int_V \boldsymbol{\nabla} \cdot \boldsymbol{F} \, dV = \int_V Q_V \, dV + \int_V \boldsymbol{\nabla} \cdot \boldsymbol{Q}_S \, dV. \tag{2.5}$$

The last equation is valid for an arbitrary volume V which leads us to the differential form of the conservation law

$$\frac{\partial U}{\partial t} + \boldsymbol{\nabla} \cdot \boldsymbol{F} = Q_V + \boldsymbol{\nabla} \cdot \boldsymbol{Q}_S. \tag{2.6}$$

An essential aspect of the conservation law (2.4) lies in the fact, that in absence of volume sources Q_V, the variation of U is given uniquely by flux contribution through the surface S and not by fluxes in the volume V.

Separating the flux vector into its two contributions $\boldsymbol{F}_D$ and $\boldsymbol{F}_C$ we obtain a more familiar expression of the general conservation law. The convective flux vector $\boldsymbol{F}_C$ attached to the quantity U in a flow with velocity $\boldsymbol{v}$, is the amount of U transported with flow, and is given by

$$\boldsymbol{F}_C = \boldsymbol{v} U. \tag{2.7}$$

The diffusive flux is defined as the contribution present in the fluid at rest, due to molecular thermal agitation. It can be expressed by a generalized gradient law:

$$\boldsymbol{F}_D = -\kappa \rho \boldsymbol{\nabla} u, \tag{2.8}$$

where ρ is the specific mass of the fluid, u the quantity U per unit mass, i.e. $U = \rho u$, and κ a diffusivity constant. Equation (2.6) can than be stated as

$$\frac{\partial \rho u}{\partial t} + \boldsymbol{\nabla} \cdot (\rho \boldsymbol{v} u) = \boldsymbol{\nabla} \cdot (\kappa \rho \boldsymbol{\nabla} u) + Q_V + \boldsymbol{\nabla} \cdot \boldsymbol{Q}_s. \tag{2.9}$$

This is the general form of a transport equation for the quantity $U = \rho u$. As seen from equation (2.6) the surface sources have the same effect on the system as a flux term, and therefore we might consider them, at least from a mathematical point of view, as additional sources. However this classification into fluxes and sources is generally preferred, since it allows a clear physical interpretation of all contributions to the evolution of the quantity U.

2.1.2 Vector conservation law

If the conserved property is described by a vector $\boldsymbol{U}$, then the Flux becomes a tensor F, the volume sources a vector $\boldsymbol{Q}_V$ and finally the surface sources become a tensor Q_s, also. The general form of a conservation law for vector quantities is then

$$\frac{\partial}{\partial t} \int_V \boldsymbol{U}\, dV + \int_V \boldsymbol{\nabla}\!\cdot\!\mathsf{F}\, dV = \int_V \boldsymbol{Q}_V\, dV + \int_V \boldsymbol{\nabla}\!\cdot\!\mathsf{Q}_S\, dV, \qquad (2.10)$$

where we have applied Gauss's theorem. Again this is valid in an arbitrary volume V and we gain the corresponding general conservation law for vector quantities in differential form as

$$\frac{\partial \rho \boldsymbol{u}}{\partial t} + \boldsymbol{\nabla}\!\cdot\!(\rho \boldsymbol{v}\otimes\boldsymbol{u}) = \boldsymbol{Q}_V + \boldsymbol{\nabla}\!\cdot\!\mathsf{Q}_s. \qquad (2.11)$$

Where $\boldsymbol{u}$ is defined by $\boldsymbol{U} = \rho\boldsymbol{u}$. We will not make further use of the diffusive flux tensor $F_{D_{ij}} = -\rho\kappa\partial_i u_j$ and thus drop it. The convective component of the flux tensor is given by

$$\mathsf{F}_C = \boldsymbol{v}\otimes\boldsymbol{U} = \rho\boldsymbol{v}\otimes\boldsymbol{u}. \qquad (2.12)$$

2.2 Navier-Stokes Equations

The law of mass conservation is a general statement of kinetic nature, that is, independent of the nature of the fluid or of the forces acting on it. It expresses the empirical fact that, in a fluid system, mass cannot disappear from the system nor be created. The general conservation law then becomes in differential form

$$\partial_t \rho + \boldsymbol{\nabla}\!\cdot\!(\rho\boldsymbol{v}) = 0. \qquad (2.13)$$

In order to formulate the conservation law for momentum, it is necessary to define the sources influencing the variation of momentum. It is known, from Newton's laws, that in a physical system these sources are the forces acting on it. The forces consist of the external volume forces $\boldsymbol{f}_e$ and the internal forces $\boldsymbol{f}_i$. The latter depend on the nature of the fluid considered, i.e. on the assumptions made about the deformations within the fluid and their relation to internal stresses. We will assume that the fluid is Newtonian, and therefore the total internal stresses $\mathsf{\Pi}$ are taken to be

$$\mathsf{\Pi} = -p\mathsf{I} + \tau, \qquad (2.14)$$

where I is the unit tensor. Here the isotropic pressure tensor component $p\mathsf{I}$ is introduced and τ is the viscous stress tensor equal to (Landau and Lifshitz, 1959, chapter 2)

$$\tau_{ij} = \mu\sigma_{ij} = \mu\left((\partial_i v_j + \partial_j v_i) - \frac{2}{3}(\boldsymbol{\nabla}\!\cdot\!\boldsymbol{v})\delta_{ij}\right), \qquad (2.15)$$

where σ is the shear tensor and μ is the dynamic viscosity of the fluid. The kinematic viscosity ν is defined by $\nu = \mu/\rho$. This relation is valid for a Newtonian fluid in thermodynamic equilibrium.

After having specified the forces acting on the fluid we obtain the differential form of momentum conservation

$$\partial_t(\rho\boldsymbol{v}) + \boldsymbol{\nabla}\cdot(\rho\boldsymbol{v}\otimes\boldsymbol{v}) = -\boldsymbol{\nabla}p + \boldsymbol{\nabla}\cdot\tau + \rho\boldsymbol{f}_e. \tag{2.16}$$

This equation is commonly referred to as the *Navier-Stokes equation of motion*. For an ideal fluid without internal stresses, that is an inviscid flow, this reduces to the *Euler equation of motion*.

The energy content of a system is measured by its internal energy per unit mass ε, i.e. the specific energy. The first law of thermodynamics states that the sources of variation of the specific energy are the work of the internal forces acting on the system $\boldsymbol{\nabla}\cdot(\Pi\cdot\boldsymbol{v})$ and the heat transmitted to the system q_h. Using the momentum equation we obtain the conservation of energy in its differential form

$$\partial_t(\rho\varepsilon) + \boldsymbol{\nabla}\cdot(\rho\varepsilon\boldsymbol{v}) = -p\boldsymbol{\nabla}\cdot\boldsymbol{v} + (\tau\cdot\boldsymbol{\nabla})\cdot\boldsymbol{v} + \boldsymbol{\nabla}\cdot(\kappa\boldsymbol{\nabla}T) + q_h \tag{2.17}$$

The diffusive component (see equation 2.7) of the energy flux is given by heat transfer $-\boldsymbol{\nabla}\cdot(\kappa\boldsymbol{\nabla}T)$. Heat sources q_h could include radiation, chemical processes or other physical phenomena. This last equation can also be formulated as an equation for the entropy s

$$\rho T\{\partial_t s + (\boldsymbol{v}\cdot\boldsymbol{\nabla})s\} = (\tau\cdot\boldsymbol{\nabla})\cdot\boldsymbol{v} + \boldsymbol{\nabla}\cdot(\kappa\boldsymbol{\nabla}T) + q_h. \tag{2.18}$$

The system of Navier-Stokes equations has still to be supplemented by a specification of the kinematic viscosity ν as a function of the other flow variables. Further more, equations of state $p(\varepsilon, \rho)$ and $T(\varepsilon, \rho)$ have to be specified to close the system. In many instances a compressible fluid can be considered as a perfect gas, even if viscous effects are taken into account, and the equation of state is written

$$p(\varepsilon, \rho) = (\gamma - 1)\varepsilon\rho, \qquad T(\varepsilon, \rho) = \frac{\bar{\mu}m_p}{k}(\gamma - 1)\varepsilon, \tag{2.19}$$

where $\gamma = C_p/C_V$ is the ratio of specific heats, $\bar{\mu}m_p$ the mean molecular weight times the proton mass and k the Boltzmann constant. For convenience we define the adiabatic and the isothermal sound-speeds, c_{ad} and c_s, as

$$c_{ad}^2 = \left(\frac{\partial p}{\partial \rho}\right)_s = \gamma\frac{p}{\rho}, \qquad c_s^2 = \left(\frac{\partial p}{\partial \rho}\right)_T = \frac{p}{\rho}. \tag{2.20}$$

Finally we define some convenient quantities as internal energy density e and momentum density $\boldsymbol{p}$ by

$$e = \rho\varepsilon, \qquad \boldsymbol{p} = \rho\boldsymbol{v}. \tag{2.21}$$

2.3 Symmetries and vertical integrated equations

Unless otherwise noted we work in cylindrical coordinates (R, ϕ, z). This is a the natural choice for disk like flows from an analytical point of view and is also appropriate for numerical simulations. Cylindrical coordinates are in general problematic for numerical computations as the Jacobian diverges at the rotation axes. We do not calculate our models down to the axes, but only to the event horizon of the Schwarzschild black hole at $R = R_g$, so this is no issue.

For the rest of this work we make the assumption that all physical variables are constant in azimuthal direction, i.e. all derivatives with respect to the azimuthal coordinate vanish, i.e. $\partial_\phi = 0$. This allows us to reduce the dimension of the problem by dropping the azimuthal coordinate. It is thus not possible to resolve local disturbances in azimuthal direction, like spiral arms or turbulence (which might very well be a source of viscosity). We assume further that the flow is symmetric with respect to the equatorial plane and limit our analysis to positive values of z.

The accretion flow is assumed to be confined within an constant angle $\theta = \pi/2$ around the equatorial plane. This is equivalent to assuming that the vertical extent of the disk H is less than the radial coordinate, i.e. $H/R \leq 1$. Such disks are sometimes referred to as slim disks. This assumption is less restrictive than $H/R \ll 1$ usually made in standard thin disk theory. In a formal sence we expand the equations into a taylor series in H/R and drop terms of the order $\mathcal{O}(H/R)^2$.

The radial structure of the disk is calculated from vertically integrated variables. The vertical integration scheme is used to decouple the vertical and radial directions. We assume that the radial and azimuthal velocity components together with their radial gradients are independent of the vertical coordinate z and equal to the respective value at the equatorial plane, i.e.

$$v_R(R, z) \simeq v_R(R, z = 0), \qquad \frac{\partial v_R}{\partial R}(R, z) \simeq \frac{\partial v_R}{\partial R}(R, z = 0) \tag{2.22}$$

and equivalently for the azimuthal component v_ϕ. The vertical integration is then understood as integration over vertical coordinate with radius dependent limits $z = H(R)$. Frequently used vertically integrated variables are

$$\Sigma(R) \equiv \int_{-H(R)}^{H(R)} \rho \, dz = 2 \int_0^H \rho \, dz \simeq 2 \, H(R) \, \rho(R, z = 0) \tag{2.23}$$

$$P(R) \equiv \int_{-H(R)}^{H(R)} p \, dz = 2 \int_0^H p \, dz \simeq 2 \, H(R) \, p(R, z = 0) \tag{2.24}$$

$$E(R) \equiv \int_{-H(R)}^{H(R)} e \, dz = 2 \int_0^H e \, dz \simeq 2 \, H(R) \, e(R, z = 0) \tag{2.25}$$

The same vertical integration is performed on the Navier-Stokes equations. We further assume that vertical integration and partial derivation are interchangeble and thus move the integral through the derivatives. We hence obtain a set of

vertical integrated equations which is formally identical to (2.13-2.17), but uses (Σ, P, E) instead of (ρ, p, e). In general we denote vertical integrated quantities with uppercase letters, while the respective volume densities are denoted with a lowercase letter.

The vertical structure of the disk und thus the disk-height H is calculated under the assumption of vertical hydrostatic equilibrium, i.e. the vertical pressure gradient is balanced by vertical tidal acceleration towards the midplane (see eqs. 2.31, 2.32)

$$\partial_z p = -\rho \partial_z \Psi = \rho \Omega_K^2 z. \tag{2.26}$$

Let H be the disk-height and the pressure gradient approximated by $\partial_z p \approx p/H$, hence $H^2 = p/(\rho \Omega_K^2)$, and using the definition (2.20) of the isothermal sound speed c_s, we obtain an explicit expression for H

$$H = \frac{c_s}{\Omega_K}. \tag{2.27}$$

Thus vertical and radial structure are completedly decoupled.

We decompose the vector of momentum density $\Sigma \boldsymbol{v}$ into three components, namely, radial momentum $P_R = \Sigma v_R$, angular momentum $L = \Sigma l = \Sigma v_\phi R$ and vertical momentum $\Sigma v_z = 0$, which vanishes by virtue of the assumed vertical structure. Hence we drop the vertical momentum equation and retain the two equations

$$\partial_t p_R + \boldsymbol{\nabla} \cdot (p_R \boldsymbol{v}) = -\partial_R P + \Sigma(\Omega^2 - \Omega_K^2)R + (\boldsymbol{\nabla} \cdot \tau)_R \tag{2.28}$$

$$\partial_t L + \boldsymbol{\nabla} \cdot L\boldsymbol{v} = (\boldsymbol{\nabla} \cdot \tau)_\phi R, \tag{2.29}$$

for numerical integration.

2.4 Physical essentials

2.4.1 Viscosity prescription

Molecular viscosity turns out to be in disagreement with observed properties of accretion disk. Angular momentum transfer by molecular viscosity alone is much too ineffective. Thus cannot be the only source of viscous stresses in the astrophysical flows.

If one assumes the existence of a small-scale chaotic magnetic field in the accretion disks, which may be sufficiently small as to not affect the dynamics of the flow, several other sources of viscosity come to mind: magneto-hydrodynamic and plasma instabilities (Stone and Balbus, 1996), small scale convective turbulence (Kley et al., 1993; Klahr et al., 1999), etc. But up to now there is no convincing theory describing viscous processes in such plasmas. We have to rely on phenomenological prescription for viscosity in astrophysical flows of interest.

Shakura and Sunyaev (1973) proposed the so called α-parameterization, which has ever after been the standard formulation used in accretion disk theory. Purely on dimensional grounds they suggested

$$\nu = \alpha c_s H, \tag{2.30}$$

where α is a pure positive number. The idea is that viscosity is generated by turbulent motion. The diameter of such turbulent cells cannot be larger than the typical disk height H. On the other hand, turbulent motion cannot be supersonic for longer periods of time, otherwise energy would be dissipated very fast and the typical turbulence velocity would drop below the sound speed. Hence we conclude that α is smaller than unity by definition, i.e. $\alpha \leq 1$.

We note that the α-ansatz can only be an effective spatially and time-averaged modeling of viscosity. Though this is an ongoing debate, there seems at least to be consensus on the fact that viscous transport of angular momentum an energy does vary strongly in time and space. Not only is the magnitude of α uncertain, but also the sign and therefore the direction of transport (see also Stone and Balbus, 1996; Klahr et al., 1999; Arlt and Rüdiger, 2001; Rüdiger et al., 2002, for recent studies on the subject).

2.4.2 External force

The only external force we consider is the gravitational attraction of the central black hole due to its gravitational potential Ψ. The gravitational force is then given by $\rho \boldsymbol{f}_e = -\rho \boldsymbol{\nabla} \Psi$. To simulate relativistic effects we adopt the pseudo-Newtonian potential

$$\Psi = -\frac{GM}{r - 2\mathrm{R_g}}, \tag{2.31}$$

where M is the mass of the black hole, $\mathrm{R_g}$ its gravitational radius given by $\mathrm{R_g} = GM/c^2$ and $r = (R^2 + z^2)^{1/2}$ the distance from the central object. This potential represents the dynamical aspects of general relativistic effects in the Schwarzschild metric quite well[1] (Paczynsky and Wiita, 1980) and greatly simplifies the basic equations. The keplerian angular velocity Ω_K in the equatorial plane is

$$\Omega_K^2 = \frac{1}{R}\frac{\partial \Psi}{\partial R} = \frac{1}{R}\frac{GM}{(R - 2\mathrm{R_g})^2}. \tag{2.32}$$

Ω_K is the angular velocity of a test particle in orbit around the central mass. The gravitational force vector $\rho \boldsymbol{f}_e$ has no component along the azimuthal direction and the vertical momentum equation has been dropped as discussed in section 2.3. Thus the only remaining component is radial

$$(\rho \boldsymbol{f}_e)_R = -\rho\, \Omega_K^2\, R. \tag{2.33}$$

---

[1]in the sense that equation (2.31) reproduces exactly the locations of the marginally bound orbit $r_{mb} = 4\,\mathrm{R_g}$ and the marginally stable orbit $r_{ms} = 6\,\mathrm{R_g}$ of a Schwarzschild black hole. The efficiency of energy conversion η is in good numerical agreement, e.g. at the marginally stable orbit we have $\eta = 0.0625$ using the pseudo-Newtonian potential, whilst the correct result in the Schwarzschild metric gives $\eta = 0.057$.

We note that the fluid elements in an accretion flow will, in general, not move like test particles along geodesics, but rather feel the effective gravity

$$g_{eff} = -\Omega_K^2 R + \Omega^2 R \approx -\frac{1}{\rho}\partial_R p \qquad (2.34)$$

where the second term ΩR^2 is due to the centrifugal force.

2.4.3 Convective turbulence

Anticipating the discussion in section 3.3 we include an additional cooling term into the energy equation. We will show that accretion flows may be subject to convective instability, that is, though the bulk motion will always be radially inward towards the central black hole, turbulent convective motion may be superimposed. Convective eddies have at least a 2-dimensional structure, more likely even 3-dimensional. These clearly cannot be resolved by 1-dimensional height integrated modelling. On the other hand convection will transport energy and possibly angular momentum, even after volume and time averaging. While in 3-dimensional simulations this is included automatically, we must model such processes in an appropriate way and include corresponding terms into the respective 1-dimensional height integrated equations.

It is natural to assume that the cooling rate due to turbulent convective motion Q_{trb}^+ is given by the divergence of the turbulent energy flux $\boldsymbol{F}_{trb}$, i.e.

$$Q_{trb}^+ = -\boldsymbol{\nabla}\cdot\boldsymbol{F}_{trb}. \qquad (2.35)$$

This has been studied extensively in stellar dynamics, but only recently applied to accretion flows (Honma, 1996; Manmoto et al., 2000). We follow Manmoto et al. (2000) and assume that the turbulent energy flux is proportional to the (negative of the) entropy gradient,

$$\boldsymbol{F}_{trb} = -K_T \rho T \boldsymbol{\nabla} s = -K_T \nabla e + K_T \gamma \frac{e}{\rho}\boldsymbol{\nabla}\rho. \qquad (2.36)$$

K_T is the turbulent diffusion constant which we parameterize as

$$K_T = \alpha_T \frac{c_s^2}{\Omega_K}, \qquad (2.37)$$

with $\alpha_T \leq 1$ as a dimensionless parameter. This is done purely on dimensional grounds, in analogy to the Shakura-Sunyaev viscosity model.[2]

2.4.4 Radiative cooling

The fluid cools via radiation or is heated by external radiation fields. The intensity to which gas of temperature T (in local thermodynamical equilibrium)

---

[2]Another possibility is to derive α_T from mixing length theory. One result is, that $\alpha_T(\alpha)$ is a function of α (Narayan et al., 2000). See also appendix A

exposes its reservoir of internal energy to the radiation field u, is given by the radiative energy density of a black body of temperature T, i.e.

$$u_{BB} = a_R T^4, \tag{2.38}$$

where a_R is the Stefan-Boltzmanm radiation density constant.

The rate q_{rad} at which gas transfers energy to or from the radiation field u is proportional to the difference of the energy density of the black body and the radiation field. It can be stated as (Mihalas and Mihalas, 1984)

$$q_{rad}^- = 2c\tau_P(a_R T^4 - u). \tag{2.39}$$

The constant of proportionality τ_P is the Planck-mean of the optical depth τ_ν, i.e.

$$\tau_P = \rho\, l \int_0^\infty \kappa_\nu \, \frac{4\pi}{c} \frac{B_\nu(T)}{a_R\, T^4} \, d\nu = \rho\, l\, \kappa_P, \tag{2.40}$$

where ν is the photon frequency, B_ν the Planck function, l the path length and κ_P the Planck-mean of the absorption coefficient κ_ν. For numerical evaluation we use (Cox and Guili, 1968)

$$\kappa_P = 0.24 \times 10^{25}\, \rho\, T^{-7/2}. \tag{2.41}$$

2.5 Radiative transfer in a nutshell

The radiative cooling rate q_{rad} depends on the energy density u of the radiation field. Full radiative transfer requires evolution of 6-dimensional fields, three spatial coordinates, the photon frequency ν and two angles describing the direction of photon propagation. The evolution of the radiation field in absence scattering is described by the radiative transfer equation

$$\left\{ \frac{1}{c}\frac{\partial}{\partial t} + \frac{\partial}{\partial s} \right\} I_\nu = \epsilon_\nu - \kappa_\nu\, I_\nu, \tag{2.42}$$

where I_ν is the intensity of the radiation field at frequency ν, ϵ_ν the emissivity and κ_ν the absorption coefficient. The three quantities I_ν, ϵ_ν, κ_ν, are in general functions of $(\boldsymbol{x}, t; \boldsymbol{n}, \nu)$, where $\boldsymbol{x}$ is the spatial coordinate and $\boldsymbol{n}$ a unit vector pointing along the direction of propagation.

The task of solving the radiative transfer equation (2.42) is considerably lessened by assuming that all relevant radiative processes are isotropic, i.e. independent of the direction $\boldsymbol{n}$, such that integration over directions is trivial.

Furthermore the detailed spectral distribution is unimportant for our purposes. We are only interested in the total energy density u of the radiation field and its impact on disk dynamics through cooling effects. We thus integrate the radiative transfer equation over frequency. This is not trivial by itself, as the material functions ϵ_ν and κ_ν depend strongly on microscopic atomic processes.

We limit ourselves to free-free electron scattering processes and neglect effects from individual quantum mechanical transitions within atoms. This allows us to use simple analytical expressions for the material functions.

The last and most important assumption is that the diffusion approximation is taken to be valid. If the mean-free-path length λ is considerably smaller than the physical scale of the region of interest $l \gg \lambda$, then photons traveling through the medium will undergo multiple scattering events and reach an equilibrium state with the surrounding medium where the evolution of the radiation energy density can be described by a diffusion equation, i.e.

$$\frac{\partial u}{\partial t} + \boldsymbol{\nabla}\cdot\boldsymbol{F}_{diff} = q^+_{src}, \tag{2.43}$$

where $q^+_{src} = q^-_{rad}$ is the rate at which thermal energy is supplied to the radiation field by the surrounding gas (see equation 2.39). The diffusive radiative flux is

$$\boldsymbol{F}_{diff} = -\frac{c\lambda}{3\tau_R}\boldsymbol{\nabla}u. \tag{2.44}$$

Formally the diffusion equation is obtained from the moment formalism. The radiative transfer equation (2.42) is multiplied with powers of the directional vector $\boldsymbol{n}$ and integrated over the unit-sphere. This procedure yields one equation for every moment u_ν, $\boldsymbol{F}_\nu$, etc. The first moment equation is

$$\frac{\partial u_\nu}{\partial t} + \boldsymbol{\nabla}\cdot\boldsymbol{F}_\nu = \oint (\epsilon_\nu - \kappa_\nu\, I_\nu)\,\mathrm{d}\omega \tag{2.45}$$

$$u_\nu = \oint I(\boldsymbol{x},t,\boldsymbol{n},\nu)\,d\omega \tag{2.46}$$

$$\boldsymbol{F}_\nu = \oint I(\boldsymbol{x},t,\boldsymbol{n},\nu)\cdot\boldsymbol{n}\,d\omega. \tag{2.47}$$

If the medium is isotropic the radiative flux can be approximated, under the further assumption of large optical depth, by

$$\boldsymbol{F}_\nu = -\frac{c}{3\kappa_\nu}\boldsymbol{\nabla}u_\nu = -\frac{c\lambda}{3\tau_\nu}\boldsymbol{\nabla}u_\nu. \tag{2.48}$$

A final integration over frequency yields our expression (2.44). See any textbook on radiative transfer for a detailed discussion on the topic (eg. Mihalas and Mihalas, 1984; Gracia, 1998).

We decompose $\boldsymbol{F}_{diff}$ into fluxes along the radial direction F_{rad} and along the vertical direction. In our height integrated scheme the latter can be easily calculated using $\lambda = H$ and yields the escape rate (Honma, 1996)

$$q^-_{esc} = \frac{2c\,H}{1 + 3/4\,\tau_R}\,u. \tag{2.49}$$

This is the rate at which the radiation field within the accretion disk looses energy or photons through its upper and lower surface (hence the factor 2).

The unusual denominator in (2.49) has purely technical reasons. Formally the diffusion approximation is only valid in the limit of large optical depth $\tau_\nu \gg 1$. For numerical computations one can still adopt it if a flux-limiter is used. For small optical depth $\tau \ll 1$ the last expression without the 1 in the denominator would diverge and thus lead to unphysical infinite propagation speeds of photons. The flux limiter ensures that photon propagation speed does not exceed the speed of light.

The radial (i.e. along the unit vector $\hat{\boldsymbol{e}}_{\boldsymbol{r}}$) diffusive flux is explicitly included into the calculations as

$$\boldsymbol{F}_{rad} = -\frac{cH}{3\tau_R}\nabla_R u\, \hat{\boldsymbol{e}}_{\boldsymbol{r}}. \tag{2.50}$$

Collecting terms and performing the vertical integration $U = 2Hu$, the radiative transfer equation takes the form

$$\frac{\partial U}{\partial t} + \boldsymbol{\nabla}\cdot\boldsymbol{F}_{rad} = Q^+_{src} - Q^-_{esc}, \qquad \boldsymbol{F}_{rad} = -\frac{cH}{3\tau_R}\nabla_R U, \tag{2.51}$$

$$Q^+_{src} = Q^-_{rad} = 2c\tau_P(2H\, a_R T^4 - U), \qquad Q^-_{esc} = \frac{2c\,H}{1 + 3/4\,\tau_R}\, U. \tag{2.52}$$

2.6 The final system

Assuming axial symmetry and neglecting special relativistic corrections, transonic accretion flows with radiation field can be described by the set of time-dependent Navier-Stokes-Equations – namely, continuity, radial momentum, angular momentum and energy equation – and a radiative transfer equation, which read

$$\partial_t\Sigma + \boldsymbol{\nabla}\cdot\Sigma\boldsymbol{v} = 0 \tag{2.53}$$

$$\partial_t\Sigma v_R + \boldsymbol{\nabla}\cdot\Sigma v_R\boldsymbol{v} = -\partial_R P + \Sigma(\Omega^2 - \Omega_K^2)R + (\boldsymbol{\nabla}\cdot\tau)_R \tag{2.54}$$

$$\partial_t\Sigma l + \boldsymbol{\nabla}\cdot\Sigma l\boldsymbol{v} = (\boldsymbol{\nabla}\cdot\tau)_\phi\, R, \tag{2.55}$$

$$\partial_t E + \boldsymbol{\nabla}\cdot E\boldsymbol{v} + P\boldsymbol{\nabla}\cdot\boldsymbol{v} = Q^+_{vsc} + Q^+_{trb} - Q^-_{rad}, \tag{2.56}$$

$$\partial_t U + Q^-_{diff} = Q^+_{src} - Q^-_{esc} \tag{2.57}$$

where $\Sigma = 2H\rho$ is the vertically integrated surface density with scale-height $H = c_s/\Omega_K$; $P_R = \Sigma v_R$ the radial momentum; $\Omega = v_\phi/R$ the angular velocity; $L = \rho l = \rho\Omega R^2$ the angular momentum; E vertically integrated internal energy density; U vertical integrated radiative energy density, respectively.

The total pressure P is given by the sum of gas pressure, radiative pressure, turbulent pressure and possibly magnetic pressure

$$P = P_g + P_{rad} + P_{trb} + P_{mag}, \tag{2.58}$$

where we do not consider magnetic fields ($P_{mag} = 0$) and neglect turbulent pressure ($P_{trb} = 0$). Three equations of state are needed, e.g. for gas pressure P_g, temperature T and radiative pressure P_{rad}. We adopt

$$P_g(\varepsilon, \Sigma) = (\gamma - 1)\, E = (\gamma - 1)\,\Sigma\varepsilon, \tag{2.59}$$

$$T(\varepsilon, \Sigma) = \frac{\bar{\mu}m_h}{k}(\gamma - 1)\varepsilon = \frac{\bar{\mu}m_h}{k}(\gamma - 1)\frac{E}{\Sigma}, \tag{2.60}$$

$$P_{rad} = \frac{1}{3}U. \tag{2.61}$$

For convenience we define the adiabatic c_{ad} and the isothermal sound-speed c_s

$$c_{ad}^2 = \left(\frac{\partial P}{\partial \Sigma}\right)_s = \gamma\frac{P}{\Sigma}, \qquad c_s^2 = \left(\frac{\partial P}{\partial \Sigma}\right)_T = \frac{P}{\Sigma}. \tag{2.62}$$

Gravitation enters through the keplerian angular velocity Ω_K of the pseudo-Newtonian potential

$$\Omega_K^2 = \frac{1}{R}\partial_R\Psi = \frac{1}{R}\frac{GM}{R(R - \mathrm{R_g})}. \tag{2.63}$$

Viscous stresses are described by the viscous stress tensor $\tau = \mu\sigma$, which is the product viscosity μ times shear tensor σ, i.e.

$$\tau_{ij} = \mu\sigma_{ij} = \mu[(\partial_i v_j + \partial_j v_i) - \frac{2}{3}(\boldsymbol{\nabla}\cdot\boldsymbol{v})\delta_{ij}]. \tag{2.64}$$

With the symmetry assumptions the only non-zero components are τ_{RR} and $\tau_{R\phi}$. Unless otherwise noted we consider both components in our numerical calculations. In the literature it is common practice to neglect the τ_{RR} component. This is usually a save approximation, unless one encounters large gradients in the radial velocity – which is exactly the case in the transition region we are interested in. We adopt the α-viscosity (Shakura and Sunyaev (1973)) and set

$$\mu = 2\Sigma\nu = 2\Sigma\alpha c_s H \tag{2.65}$$

The sources and sink for internal energy and radiative energy are viscous heating Q_{vsc}^+, radiative cooling Q_{rad}^-, turbulent convective transport Q_{trb}^+, and thermal emission Q_{src}^+, radiative losses through vertically escaping photons Q_{esc}^- and radial diffusion Q_{diff}^-

$$Q_{vsc}^+ = (\tau\cdot\boldsymbol{\nabla})\cdot\boldsymbol{v} \tag{2.66}$$

$$Q_{rad}^- = 2c\tau_P(2H\,a_R T^4 - U) \tag{2.67}$$

$$Q_{trb}^+ = -\boldsymbol{\nabla}\cdot\boldsymbol{F}_{trb}, \quad \boldsymbol{F}_{trb} = -K_T\rho T\boldsymbol{\nabla}S = -K_T\boldsymbol{\nabla}E + K_T\gamma\varepsilon\boldsymbol{\nabla}\Sigma \tag{2.68}$$

$$Q_{src}^+ = Q_{rad}^- \tag{2.69}$$

$$Q_{esc}^- = \frac{2c\,H}{1 + 3/4\,\tau_R}U \tag{2.70}$$

$$Q_{diff}^- = \boldsymbol{\nabla}\cdot\boldsymbol{F}_{rad}, \qquad \boldsymbol{F}_{rad} = -\frac{cH}{3\tau_R}\nabla_R U\,\hat{\boldsymbol{e}_r}. \tag{2.71}$$

In deriving these equations we assumed the vertical structure of the flow to be in hydrostatic equilibrium, i.e. the vertical pressure gradient is balanced by vertical tidal acceleration towards the disk midplane. The vertical disk height can then be calculated to

$$H = \frac{c_s}{\Omega_K} \tag{2.72}$$

as discussed in section 2.4.1. This system represents the time-dependent generalization of Manmoto and Kato (2000).

2.7   The steady limit

In this section we discuss the steady limit of equations (2.53) through (2.57). We assume that the flow has reached some equilibrium state $\partial_t = 0$. Many important properties of accretion flows reveal themselves in this limit.

First consider the continuity equation (2.53). With $\partial_t \Sigma = 0$ and the symmetry $\partial_\phi = \partial_z = 0$ this yields

$$\frac{1}{R} \frac{d\Sigma v_R}{dR} = 0. \tag{2.73}$$

We integrate over a cylindrical volume centered at $R = 0$, of height H and radius R and recover the accretion rate $\dot{M}$ as

$$\dot{M} = -4\pi R H \rho v_R = -2\pi R \Sigma v_R. \tag{2.74}$$

The accretion rate is constant in space and time (by virtue of the assumption of steadiness). In a mathematical sense the accretion rate is an eigenvalue of the problem and does only depend on the boundary conditions, i.e. on the mass flux at the boundaries (formally at infinity). It is independent of the structure or operating microphysics of the flow. Furthermore, a steady or even quasi-steady accretion flow will always adjust its structure such that equation (2.74) holds. By virtue of the constant accretion rate, the radial infall velocity v_R and surface density Σ are no longer independant of each other.

It is common practice to measure the accretion rate in units of the Eddington acretion rate $\dot{M}_{Edd}$ as proposed in the introduction, i.e. $\dot{m} = \dot{M}/\dot{M}_{Edd}$. The Eddington accretion rate is the limit at which outward radiation drag by Thomson-scattering compensates inward accelaration due to gravity (Frank et al., 1985), i.e.

$$\dot{M}_{Edd} = \frac{1}{\eta} \frac{L_{Edd}}{c^2} = \frac{1}{\eta} \frac{4\pi GM}{\kappa_{es} c}, \tag{2.75}$$

where M is the mass of the central object, $\eta \approx 1/10$ the efficiency of rest-mass to radiation conversion and κ_{es} the Thomson-scattering cross section.

The angular momentum equation in the steady limit can be expressed as[3]

$$\frac{1}{R} \frac{\partial}{\partial R} (R\Sigma l v_R) = \frac{1}{R} \frac{\partial}{\partial R} \left(2\Sigma \nu R^3 \frac{\partial \Omega}{\partial R} \right). \tag{2.76}$$

Integrating over radial coordinate and substituting the accretion rate $\dot{M}$ this yields

$$\dot{M}(l - l_0) = -4\pi \Sigma \nu R^3 \frac{\partial \Omega}{\partial R}, \tag{2.77}$$

where l_0 is formally an integration constant and can be identified with the specific angular momentum swallowed by the black hole at the inner disk boundary.

---

[3]We have neglected the τ_{RR} component of the stress tensor for illustrative purpose. This is usually a safe asumption away from the transition region. For numerical computations this component is always taken into account and turns out to be very important in the transition region.

Angular momentum transport by viscosity is given by the right hand side and is oriented down the angular velocity gradient. Hence viscosity tries to drive the system towards a state of uniform rotation. For $\Omega \propto \Omega_K$ angular momentum is transported inward.

The steady limit of the energy equation is

$$\boldsymbol{\nabla}\cdot E\boldsymbol{v} + P\boldsymbol{\nabla}\cdot\boldsymbol{v} \equiv Q_{adv}^- = Q_{vsc}^+ + Q_{trb}^+ - Q_{rad}^-, \qquad (2.78)$$

where we have defined the advective cooling rate Q_{adv}^-, i.e. the amount of entropy carried with the flow towards the black hole. The turbulent convective cooling rate Q_{trb}^+ has been totally neglected in the literature until recently (Manmoto et al., 2000). The two main solution types of accretion disks, namely the standard thin disk (Shakura and Sunyaev, 1973) and advection dominated accretion flows (Narayan and Yi, 1994), are recovered by neglecting different cooling channels, advective cooling Q_{adv}^- and radiative cooling Q_{rad}^-, respectively. This will be elaborated on in the next chapter.

In our model the steady version of radiative transfer reads

$$Q_{diff}^- = Q_{src}^+ - Q_{esc}^-. \qquad (2.79)$$

Hence energy which is transfered from the plasma to the radiation field, i.e $Q_{src}^+ = Q_{rad}^-$, will be either radiated away through the surface of the disk Q_{esc}^- or transported radially by diffusion of photons due to Q_{diff}^-.

Chapter 3

Standard Disk and Advection Dominated Accretion Flow

Accretion disk theory has a long history. This chapter will try to discuss some important models. Different assumptions or targeted physical applications lead to different equations and thus different solutions. Their exact derivation has been thoroughly discussed in the literature and will only be sketched. Most important are the properties of the various accretion models and later chapters will draw heavily on them.

3.1 Shakura-Sunyaev Standard Disk

Shakura and Sunyaev (1973) found a self-consistent analytic solution for geometrically thin ($H/R \ll 1$) and optically thick ($\tau \gg 1$) accretion discs, which generally is referred to as the "standard thin disk" or "Shakura Sunyaev Disk" (SSD). This solution was generalized to the Kerr-metric for rotating Black Holes by Novikov and Thorne (1973) and Riffert and Herold (1995). The standard thin disk model successfully fits the emission properties of "low energy accreting systems", i.e. systems where hard spectral components are absent. Here I briefly summarize the essential features of the solution (see Frank et al., 1985, for a detailed review).

The gas moves along nearly keplerian orbits, with a very small radial velocity component due to viscous stresses superimposed (e.g. $v_R^2 \ll v_K^2$). Formally the keplerian velocity is a solution of the radial Euler equation (2.54) if the radial acceleration $v_R \partial v_R / \partial R$ and the radial pressure gradient $\rho^{-1} \partial p / \partial R$ are negligible compared to the gravitational and centrifugal forces. In the Schwarzschild or Kerr metric stable keplerian orbits exist only outside of the marginally stable circular orbit R_{ms}, and therefore the inner disk edge is located at (assuming an non-rotating black hole)

$$R_{in} = R_{ms} = 6\,\mathrm{R_g}. \tag{3.1}$$

Following Shakura and Sunyaev (1973) the vertically integrated viscous stresses are parameterized by $\nu = \alpha c_s H$ in cold disks. A no-torque condition is (artificially) assumed at the inner edge. We define an auxiliary function $\mathcal{F}(R)$ by

$$\mathcal{F}(R) = 1 - \frac{l_K(R_{in})}{l_K} = 1 - \left(\frac{R_{in}}{R}\right)^{1/2}. \tag{3.2}$$

Using the assumption of keplerian orbits, rather than merely circular orbits, reduces the viscous stress tensor component τ_ϕ^R to

$$\tau_\phi^R = \nu R \frac{d\Omega_K}{dR} = -\frac{3}{2} \nu \, \Omega_K \tag{3.3}$$

and the angular momentum equation yields an algebraic expression for Σv_R. v_R can then be eliminated with the continuity equation and we finally get a non-linear diffusion equation for the surface density Σ

$$\frac{3}{R} \frac{d}{dR} \left(R^{-1/2} \frac{d}{dR} (\nu \Sigma R^{-1/2}) \right) = 0, \tag{3.4}$$

where ν is still a function of radius.

To make further progress we need to specify an equation of state

$$c_s^2 = \frac{kT}{\mu m_p} + \frac{4\sigma}{3c} T^4 \tag{3.5}$$

including gas pressure on the left and radiation pressure on the right and find some expression for the temperature T. If the disk is in vertical hydrostatic equilibrium this can be related to opacity τ by

$$\frac{4\sigma T^4}{3\tau} = \frac{3GM\dot{M}}{8\pi R^3} \mathcal{F}(R) \tag{3.6}$$

$$\tau = \Sigma \kappa_R. \tag{3.7}$$

The final system is still algebraic and can be solved for every radius. Again, see Frank et al. (1985, eq. (5.45)) for explicit scalings.

As has been noted before, the standard thin disk has an inner edge at R_{in}. Thus the maximal energy which can be extracted is the binding energy at the last stable orbit and the total outward energy flux is given by

$$W_{SSD} = \frac{3}{2} \frac{GM\dot{M}}{R_{in}} > 0. \tag{3.8}$$

3.2 Advection Dominated Accretion Flow

In deriving the SSD we have assumed that local radiative cooling is very efficient. Advection Dominated Accretion Flows (hereafter ADAF) are in some respect the opposite limiting case. It is assumed that local radiative cooling

is *not* the dominant cooling channel. Viscous heating will then be stored as internal energy in the disk and will be advected with the accretion flow towards the central object. The gas will be driven to higher temperature which will lead to vertical thickening of the disk. Pressure forces will also become important and the effective gravity will increase accordingly and the disk material will likely rotate sub-keplerian such that the radial infall velocity will no longer be negligible.

First steps to understand such flows have been done by Narayan and Yi (1994) (hereafter NY) who presented the following self similar solutions for optically thin accretion flows. Mathematically they extend from $R = 0$ to $R = \infty$, while physically appropriate boundary conditions must be imposed. Later global solutions (Peitz and Appl, 1997; Chen et al., 1995; Narayan and Yi, 1995a,b) turned out to be in very good agreement away from the boundaries. The basic properties can all be easily studied in the NY solutions and provide us with a thorough understanding of such advective accretion flows.

Following NY we consider the following system of partial differential equations

$$\frac{d}{dR}(\rho R H v_R) = 0, \tag{3.9}$$

$$v_R \frac{dv_R}{dR} - \Omega^2 R = -\Omega_K^2 - \frac{1}{\rho}\frac{d}{dR}(\rho c_s^2), \tag{3.10}$$

$$v_R \frac{d}{dR}(\Omega R^2) = \frac{1}{\rho R H}\frac{d}{dR}\left(\frac{\alpha \rho c_s^2 R^3 H}{\Omega_K}\frac{\partial \Omega}{\partial R}\right), \tag{3.11}$$

$$\Sigma v_R T \frac{ds}{dR} = \frac{3 + 3\epsilon}{2} 2\rho H v_R \frac{dc_s^2}{dR} - 2c_s^2 H v_R \frac{d\rho}{dR} = Q_{vsc}^+ - Q_{rad}^-. \tag{3.12}$$

In (3.12), the left-hand side is the advected entropy, where T is the temperature and s the entropy, while the right-hand side gives the difference between energy input per unit area due to viscous dissipation Q_{vsc}^+ and the energy loss through radiative cooling Q_{rad}^-. For convenience we have defined a parameter $\epsilon = (5/3 - \gamma)/(\gamma - 1)$, where γ is the ratio of specific heats; note that $\epsilon = 0$ in the limit $\gamma = 5/3$ and $\epsilon = 1$ when $\gamma = 4/3$.

Next we assume that a fixed fraction $f \equiv (Q_{vsc}^+ - Q_{rad}^-)/Q_{vsc}^+$ of dissipated energy is radiated away. Therefore the parameter f measures the degree to which the flow is advection-dominated. In the extreme limit of no radiative cooling we have $f = 1$, while in the opposite limit of very efficient cooling $f = 0$. It is convenient to introduce a new parameter $\acute{\epsilon} \equiv \epsilon/f$. Substituting the viscous dissipation rate for Q_{vsc}^+ the right-hand side of (3.12) yields

$$Q_{vsc}^+ - Q_{rad}^- = \frac{2\alpha\rho c_s^2 R^2 H}{\Omega_K}\left(\frac{\partial \Omega}{\partial R}\right)^2 - Q_{rad}^- = f\frac{2\alpha\rho c_s^2 R^2 H}{\Omega_K}\left(\frac{\partial \Omega}{\partial R}\right)^2. \tag{3.13}$$

We seek a self-similar solution for this system of ordinary differential equations, i. e. all relevant quantities should scale with powers of radius. The only characteristic time-scale is the keplerian angular velocity $\Omega_K \propto R^{-3/2}$ with associated

keplerian orbital velocity $v_K \propto R^{-1/2}$. Narayan and Yi (1994) showed that equations (3.9) - (3.12) permit a self-similar solution (see also Ichimaru, 1977; Spruit et al., 1987) of the form

$$\rho = \rho_0 \, R^{-3/2}, \qquad v_R = v_0 \, R^{-1/2}, \qquad \Omega = \Omega_0 \, R^{-3/2}, \qquad c_s^2 = c_0^2 \, R^{-1}, \quad (3.14)$$

where the constants satisfy the following relations

$$\rho_0 = -\frac{\dot{M}}{4\pi c_0^2 v_0}, \qquad \Omega_0^2 = \acute{\epsilon} \, c_0^2, \qquad v_0 = -\frac{3}{2} \, \alpha c_0^2. \qquad (3.15)$$

The overall normalization is fixed by

$$c_0^2 = \frac{2(5 + 2\acute{\epsilon})}{9} \frac{g(\alpha, \acute{\epsilon})}{\alpha^2} \approx \frac{2}{5 + 2\acute{\epsilon}} \qquad (3.16)$$

$$g(\alpha, \acute{\epsilon}) \equiv \left[1 + \frac{18\alpha^2}{(5 + 2\acute{\epsilon})^2} \right]^{1/2} - 1. \qquad (3.17)$$

In equation (3.16) the first relation gives the exact solution, while the second corresponds to the limit when $\alpha \ll 1$.

3.2.1 Properties of the self-similar ADAF solution

In the limit of very efficient cooling $f \to 0$ and $\acute{\epsilon} = \infty$, the solution given in equations (3.14)–(3.17) corresponds to a standard thin accretion disk with $v_R, c_s \ll v_K$ and $\Omega \to \Omega_K$. Its properties have been discussed in the previous chapter.

In the opposite limit where f is a reasonable fraction of unity and $\epsilon \sim \acute{\epsilon} < 1$, equation (3.16) shows that the sound speed is comparable to the Keplerian speed v_K, which means, that the temperature of the accreting gas is nearly virial. The disk height H is comparable to R and the flow is quasi-spherical [1].

The radial velocity of the accreting gas is proportional to α and is determined by how fast angular momentum can be transported outwards by viscous processes. Since $v_R \sim \alpha c_s^2/v_K$ the radial velocity tends to be much larger in ADAFs than in thin disks. This underlines the importance of inertial terms in our equations. The Bernoulli parameter Be can be calculated to

$$\frac{\mathrm{Be}}{v_K^2} = \frac{1}{v_K^2} \left(\frac{1}{2} v_R^2 + \frac{1}{2} \Omega^2 R^2 - \Omega_K^2 R^2 + \frac{\gamma}{\gamma - 1} c_s^2 \right) \approx \frac{3\epsilon - \acute{\epsilon}}{5 + 2\acute{\epsilon}}. \qquad (3.18)$$

It is well known, that Be is conserved in adiabatic flows in the absence of viscosity. Therefore, whenever Be is positive and gas could flow somehow adiabatically outward, it would reach infinity with a net positive energy. On the other hand if Be is negative gas cannot escape spontaneously to infinity. Equation (3.18) shows that Be is positive in advection-dominated flows for all values

[1]In the limit $\acute{\epsilon} \to 0$, which corresponds to $\gamma \to 5/3$, Ω vanishes and the solution matches on to the Bondi spherical accretion solution (see Chakrabarti, 1990).

of α and for any $\gamma < 5/3$ as long as $f > 1/3$. This gave much cause to controversial discussion in the literature, whether powerful outflows like wind or jets could originate from ADAFs (eg. Blandford and Begelman, 1999; Yuan et al., 2002).

Another very similar quantity is the vertically integrated total energy flux W which in our case is given by

$$
\begin{aligned}
W &= -\dot{m}\,Be + W_{vsc} \qquad\qquad\qquad\qquad\qquad (3.19)\\
&= -\dot{m}\left(\frac{1}{2}v_R^2 + \frac{1}{2}\Omega^2 R^2 - \Omega_K^2 R^2 + \frac{\gamma}{\gamma-1}c_s^2\right) - 4\pi R^3 H\mu\frac{d\Omega}{dR}\Omega
\end{aligned}
$$

This quantity will later proof very useful in understanding the properties of ADAF-SSD transitions. From conservation of energy immediately follows that W must be constant throughout the disk. Kato and Nakamura (1998) showed that if one neglects the left-most radial kinetic energy term, W vanishes, i.e. there is no net energy flux through the disk. On the other hand as the radial kinetic energy flux is directed inward, we conclude

$$
W_{ADAF} < 0. \qquad\qquad\qquad (3.20)
$$

Advection-dominated accretion flows as proposed by NY do show a net inward energy flux.

Another interesting property of advection-dominated flows is revealed after close examination of the entropy equation (3.12). The gradient of the entropy, which is given by

$$
\Sigma T\frac{ds}{dR} = -\frac{7}{4\pi}\alpha\dot{M}\epsilon c_0^2 R^{-9/2} < 0 \qquad\qquad (3.21)
$$

is negative and entropy increases toward smaller radii. ADAFs therefore satisfy the Schwarzschild criterion for convection and are subject to possible convective instabilities. This issue of convective energy transport and its consequences for the total energy flux W will be discussed in section 3.3.

3.2.2 Real world advection-dominated flows

As has been already mentioned earlier this self-similar solution extends formally from $R = 0$ to $R = \infty$. Real world accretion flows have a finite radial extent. Some physical boundary conditions must be imposed on the inner edge, which is usually the event horizon of the black hole, and on the outer edge. This will modify the structure of the flow. Numerical simulations like those presented in figure 3.1 show that away from the boundaries the self-similar solution is a very good approximation to global solutions with proper boundary conditions. As has been explicitly shown by Narayan et al. (1997b) the influence of the outer boundary decays rapidly for any physically reasonable prescription at the outer boundary as shown in figure 3.1.

Small deviations arise from several reasons. First, numerical simulations usually mimic the influence of the central black hole by adopting a different so called
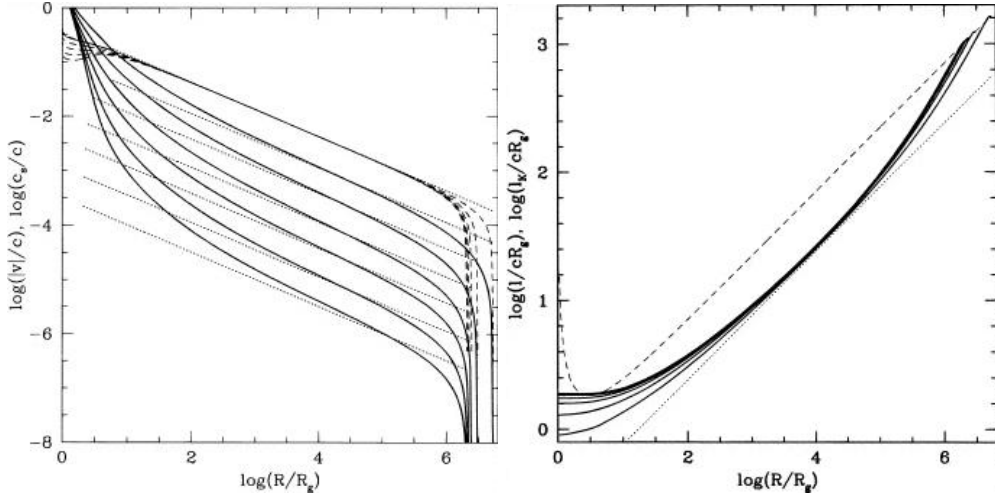
Figure 3.1: Global ADAF solutions with SSD outer boundary conditions for six values of $\alpha = (0.001, 0.003, 0.01, 0.03, 0.1, 0.3)$. In the left panel α increases from bottom to top. Solid lines show variation of radial velocity v_R. Dashed lines show isothermal sound speed c_s. The dotted lines correspond to the expected self-similar solution. The right panel illustrates the variation of specific angular momentum $l = \Omega R^2$ as solid lines. Here, α decrease from bottom to top. The dotted line represents the expected self-similar value and the short dashed line the keplerian specific angular momentum l_K. Figures adopted from Narayan et al. (1997b).

pseudo-Newtonian potential $\Psi = 1/(R - 2R_g)$ which has been first introduced by Paczynsky and Wiita (1980). Thus the self-similarity is broken at the inner edge and the flow becomes transonic at small radii. This is what one would expect anyway. Second, this solution is purely analytical. To keep things easy one neglects all but the $r-\phi$ components of the viscous stress tensor τ. The $r-\phi$ component is responsible for the transport of angular momentum. Numerical simulation usually include additionally at least the $r-r$ component because of technical reasons. This enlarges somewhat the energy dissipation rate and in return the flow is hotter.

Self-similar ADAF solutions are in principal available for any physically meaningful set of $(\dot{m}, \alpha, \gamma, f)$. Up to now the fraction f of advected energy has been assigned arbitrarily. In general f will be a function of radius and determined by the relative efficiency of advective and radiative cooling. The later depends strongly on the optical depth τ and thus the accretion rate $\dot{M}$. The previously presented solutions are thus not self-consistent.

Rees et al. (1982) noted that there is an upper limit to the mass accretion rate, such that only below this limit is optically thin advection-dominated accretion possible. Above the limiting $\dot{M}$, the cooling is too efficient and the only configuration allowed for the flow is the SSD. After global self-consistent solutions became available, several authors (eg. Chen et al., 1995; Narayan and Yi, 1995b; Honma, 1996; Kato and Nakamura, 1998) reported various approxima-
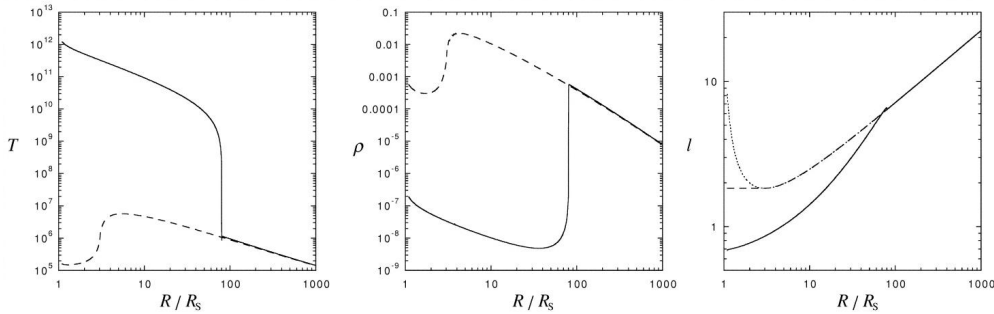
Figure 3.2: Stationary ADAF-SSD transition models obtained by Manmoto and Kato (2000). The dashed lines correspond to SSD solutions, while the solid lines to ADAF-SSD transition models. The transition is located at $R_{tr} = 80\,R_S$, where $R_S = 2R_g$ is the Schwarzschild radius. Left: Temperature, T. Middle: Density, ρ. Right: Specific angular momentum, l, in units of cR_S. The dotted line in the right panel represents the Keplerian angular momentum l_K. Figure adopted from (Manmoto and Kato, 2000).

tions for the critical accretion rate which depend on the details of included radiative processes. On the other hand they share the basic proportionality

$$\dot{m}_c \propto \alpha^2 R^{-1/2} \tag{3.22}$$

Turning this relation around we get, for a fixed accretion rate, a critical radius R_c beyond which only SSD solutions are available. Below this R_c, both, ADAF and SSD solutions are possible. It is widely believed that nature chooses advection-dominated flow wherever possible (Narayan and Yi, 1995b). This was the first theoretical hint to possible coexistence and transitions from and inner ADAF to an outer SSD.

3.3 ADAF with convection

The previous section showed that ADAFs are generally subject to convective instabilities. In that case one would expect some turbulent motion superimposed on the radial infall. This turbulent motion will also transport energy. We follow Manmoto et al. (2000) and Narayan and Yi (1994) and assume that the turbulent energy flux is proportional to the (negative of) the entropy gradient[2]

$$F_{trb} = -\rho K_T T \frac{ds}{dR}, \tag{3.23}$$

where K_T is an unknown diffusion constant which we parameterize as

$$K_T = \alpha_T \frac{c_s^2}{\Omega_K}. \tag{3.24}$$

---

[2]This is similar to the prescription used to model convective heat transport in stellar interiors.

37

This has been done purely on dimensional grounds in analogy to the Shakura-Sunyaev model of viscosity. $\alpha_T < 1$ is a dimensionless parameter. We stick to the notation of the previous section and write the flux F_{trb} and the turbulent heating rate Q_{trb}^+ as

$$F_{trb} = -3(1 + \epsilon)\frac{\alpha_T \rho c_s^2}{\Omega_K}\frac{dc_s^2}{dR} + \frac{2\alpha_T c_s^4}{\Omega_K}\frac{d\rho}{dR}, \tag{3.25}$$

$$Q_{trb}^+ = -\frac{1}{R}\frac{d}{dR}(2RHF_{trb}) \tag{3.26}$$

Our new entropy equation including turbulent convective transport Q_{trb}^+ reads

$$Q_{adv}^- = f\, Q_{vsc}^+ + Q_{trb}^+. \tag{3.27}$$

Again this system of equations permits a self-similar solution (see Manmoto et al., 2000) of the form (3.14) where the constants satisfy the following relations

$$\rho_0 = -\frac{\dot{M}}{4\pi c_0^2 v_0}, \qquad \Omega_0^2 = \left(1 - \frac{2}{3}\frac{\alpha_T}{\alpha}\right)\acute{\epsilon}\, c_0^2, \qquad v_0 = -\frac{3}{2}\alpha c_0^2. \tag{3.28}$$

The overall normalization is fixed by

$$c_0^2 = \frac{2[5 + \acute{\epsilon} - (4/3)(\alpha_T/\alpha)\acute{\epsilon}]}{9}\frac{g(\alpha, \acute{\epsilon})}{\alpha^2} \tag{3.29}$$

$$g(\alpha, \acute{\epsilon}) \equiv \left[1 + \frac{18\alpha^2}{(5 + 2\acute{\epsilon} - (4/3)(\alpha_T/\alpha)\acute{\epsilon})^2}\right]^{1/2} - 1. \tag{3.30}$$

This reduces to the original self-similar solution of NY in the limit of $\alpha_T = 0$. Alternatively one can also redefine the parameter $\acute{\epsilon} \equiv (\epsilon/f)\left(1 - (2/3)(\alpha_T/\alpha)\right)$ and use the relations (3.14)- (3.17). The primary effect of convective energy transport is thus to reduce the value of the parameter $\acute{\epsilon}$. This means that the various properties of ADAFs become even more pronounced.

3.3.1 Properties of the extended convective ADAF solution

The one crucial difference of the NY models from convective ADAFs is revealed after examination of the vertically integrated energy flux W_{trb} due to convective energy transport. This is given by

$$W_{trb} = 4\pi RH\, F_{trb} = \dot{m}\, 2\epsilon\frac{\alpha_T}{\alpha}v_K^2. \tag{3.31}$$

This quantity is rather large, such that the total energy flux

$$W = -\dot{m}\, Be + W_{vsc} + W_{trb} \tag{3.32}$$

is also positive. The exact value (see Manmoto et al., 2000) is somewhat lengthy and we merely state that

$$W_{ADAF} > W_{SSD} > 0 \tag{3.33}$$

for a wide range of parameters. An ADAF with convection can therefore supply a SSD with enough energy on its inner boundary. Manmoto and Kato (2000) were the first to obtain stationary self-consistent models with ADAF-SSD transitions (see figure 3.2). Their main result could be confirmed with our time-dependent approach (see chapter 5) while new generic time-dependent properties of such models are described in chapter 6 of this work.

Some authors (e.g. Narayan et al., 2000) do also consider energy dissipation by convective micro-turbulence as a source of energy and model this after the viscous dissipation such that

$$Q^+ = Q^+_{vsc} + Q^+_{trb} = (\alpha + \alpha_T)\frac{2\rho c_s^2 R^2 H}{\Omega_K}\left(\frac{\partial\Omega}{\partial R}\right)^2. \qquad (3.34)$$

This modifies the result only quantitatively and the conclusions still apply, if α and α_T are not too small, eg. > 0.05. For the opposite case, where α and α_T are small, Narayan et al. (2000) together with Quataert and Gruzinov (2000) found a new branch of accretion flows, where convection totally dominates the flow properties. This Convection Dominated Accretion Flow (CDAF) is briefly described in the appendix A.

Chapter 4

Numerical Aspects

In this chapter we discuss briefly some aspects of the numerical techniques to solve the proposed system of coupled differential equations. Most of the material presented in this part is standard textbook knowledge and can be read up in e.g. (Potter, 1973; Hirsch, 1988a).

4.1 Discretization

Following (Potter, 1973) let us consider a system defined by the state vector $\boldsymbol{u}(x,t)$, in the space domain $\mathcal{R} = \mathcal{R}(x)$. If $\boldsymbol{u} = \boldsymbol{u}^0$ is defined at time $t = 0$, and if $\boldsymbol{u}$ is defined on the surface $\mathcal{S}$ of $\mathcal{R}$ for all times t, we wish to determine $\boldsymbol{u}$ for all times t in $\mathcal{R}$. The state of the system may be obtained as a solution of the initial value equation

$$\frac{\partial \boldsymbol{u}}{\partial t} = L\boldsymbol{u}. \tag{4.1}$$

In general L is a non-linear spatial differential operator. For numerical computations some discretization procedure has to be applied to equation (4.1), both spatial and in time.

The state will be calculated at discrete points in space x_j , ie. on a grid, where the grid spacing Δx is given by $x_{j+1} = x_j + \Delta x$. Hence at each grid point j the spatially discretized equations

$$\frac{\partial \boldsymbol{u}_j}{\partial t} = L\boldsymbol{u}_j \tag{4.2}$$

have to be solved. These equations may be coupled to (1) adjacent grid points through the operator L, as will be discussed later, and (2) to different components or state variables $^\alpha u$ of the state vector $\boldsymbol{u}$. These could for example be density ρ, velocity v or energy e.

The state vector is further only calculated at discrete times t^n, where time is advanced in discrete time-steps Δt, such that $t^{n+1} = t^n + \Delta t$. One possible time discretization is as follows:

$$\boldsymbol{u}^{n+1} = \boldsymbol{u}^n + L\boldsymbol{u}^n(1 - \theta)\Delta t + L\boldsymbol{u}^{n+1}\theta\Delta t, \tag{4.3}$$

where $\boldsymbol{u}^n$ and $\boldsymbol{u}^{n+1}$ are the state vectors at adjacent time-points, while θ is an interpolation parameter $0 \leq \theta \leq 1$. In the special case when $\theta = 0$, the new state vector $\boldsymbol{u}^{n+1}$ is defined explicitly by the known state $\boldsymbol{u}^n$. In this case the method is called *explicit*, while otherwise if $\theta \neq 0$ the method is called *implicit*. Further if $\theta = 1/2$ this method is generally called *Crank-Nicolson scheme*, which is of second-order accuracy in time.

Explicit schemes are only stable if the size of the time step is restricted by the famous *Courant-Friedrichs-Levy condition*, which says, that no information is allowed to travel more than one grid zone within a single time step. Dependent on the problem under consideration information could propagate with the velocity of the flow or the sound speed, to mention two examples. Implicit schemes with $\theta > 1/2$ are generally stable for any size of the time step. Hence the Crank-Nicolson scheme is only marginally stable. It is common practice to use a θ somewhat larger then the critical value, to retain approximately second-order accuracy, while avoiding unstable numerical schemes. We employ $\theta = 0.61$.

The operator L will in general include derivatives of the state vector $\boldsymbol{u}$ with respect to the coordinate x, which are not available algebraically. Therefore spatial derivatives have to be discretized also. The underlying idea of the *finite difference method* is to estimate the derivative by the ratio of the differences at adjacent points according to the definition

$$u_x \equiv \frac{\partial u}{\partial x} \equiv Du = \lim_{\Delta x \to 0} \frac{u(x + \Delta x) - u(x)}{\Delta x}. \tag{4.4}$$

If Δx is small but finite the expression of the right-hand side will be a approximation to the exact value of u_x. By reducing Δx the approximation will be improved while the truncation error will tend to zero. The power of Δx with which the error tends to zero is called the *order of the difference approximation*. The procedure to generate difference approximation of any order is based upon Taylor series expansion of $u(x + \Delta x)$ (Hildebrand, 1956).

Following (Hirsch, 1988a, ch. 4.2) we define a number of difference operator by their action on the state variable u_j evaluated at node j.

Displacement operator E:
$$E^t u_j = u_{j+t}$$

Central difference operator δ:

$$\delta u_j = u_{j+1/2} - u_{j-1/2}$$

It is easily seen, that $\delta = E^{1/2} - E^{-1/2}$, where the half-valued displacements are to be interpreted as interpolation between grid nodes.[1] Then one simple discretization for the derivative operator is

$$\Delta x D = \delta, \tag{4.5}$$

---

[1] or as in our case onto the corresponding intermediate staggered grid

such that the derivative of the state variable is evaluated at node j through

$$(u_x)_j = Du_j = \frac{\delta u_j}{\Delta x} = \frac{u_{j+1/2} - u_{j-1/2}}{\Delta x}. \tag{4.6}$$

This representation is second-order accurate in space. Similar expressions for multiple derivatives like $(u_{xx})_j$ can be derived by multiple application of the last expression. This is very nicely illustrated and generalized to higher-order accuracies in (Hirsch, 1988a). Our code uses second-order accurate approximations for all spatial derivatives.

Another method, which is specially well-suited for conservation laws, is the *finite volume method*. From section 2.1 we know that conservation laws can generally be stated as

$$\frac{\partial}{\partial t} \int_V u \, dV + \oint_S \boldsymbol{f} \cdot d\boldsymbol{S} = \int_V Q \, dV, \tag{4.7}$$

where u is a state and $\boldsymbol{f}$ the associated flux. This is also true for any subdivision of the total volume V into smaller regions Ω_j. Moreover, if two sub-volumes Ω_A and Ω_B have a common surface, the fluxes from A to B, f_{AB}, and B to A, f_{BA}, through the interface will exactly cancel each other as $f_{AB} = -f_{BA}$. This effectively suppresses the growth of numerical truncation errors due to internal volume sources of the finite difference method.

The numerical computational domain is discretized by subdivision into discrete control volumes Ω_j. The surface integral is the evaluated as sum over all sides of the control volume, ie.

$$\frac{\partial}{\partial t}(u_j \, \Omega_j) + \sum_{sides} (\boldsymbol{f} \cdot \boldsymbol{S}) = Q_j \, V_j. \tag{4.8}$$

There are a number of possible choices for the approximation of the fluxes f. The obvious choice would be to average the fluxes, e.g $f_{AB} = \frac{1}{2}(f_{j-1/2} + f_{j+1/2})$. This central scheme has the drawback, that odd- and even-numbered nodes are separated, which introduces strong oscillations between adjacent nodes as discussed in (Hirsch, 1988a, ch. 6.2.1).

Another possibility is to approximate the flux at the cell interfaces by the flux upstream of the interface. This is call a *upwind* scheme. One of its properties is that it does not propagate information to upwind nodes, but only in the downwind direction and thus preserves physical causality. The simplest such scheme is the donor-cell scheme, where f_{AB} is taken to be equal to the flux of the donor-cell. Higher-order schemes introduce interpolations of the upwind flux. We employ second-order van Leer-slope (Stone and Norman, 1992) with a slope limiter called *MUSCL* (monotonic upwind-scheme for conservation laws, see Hirsch, 1988b, chapter 21). Though in principal all fluxes could be treated with this scheme, we only employ it for advection of the flow variables, ie. $\boldsymbol{\nabla} \cdot (u\boldsymbol{v})$.
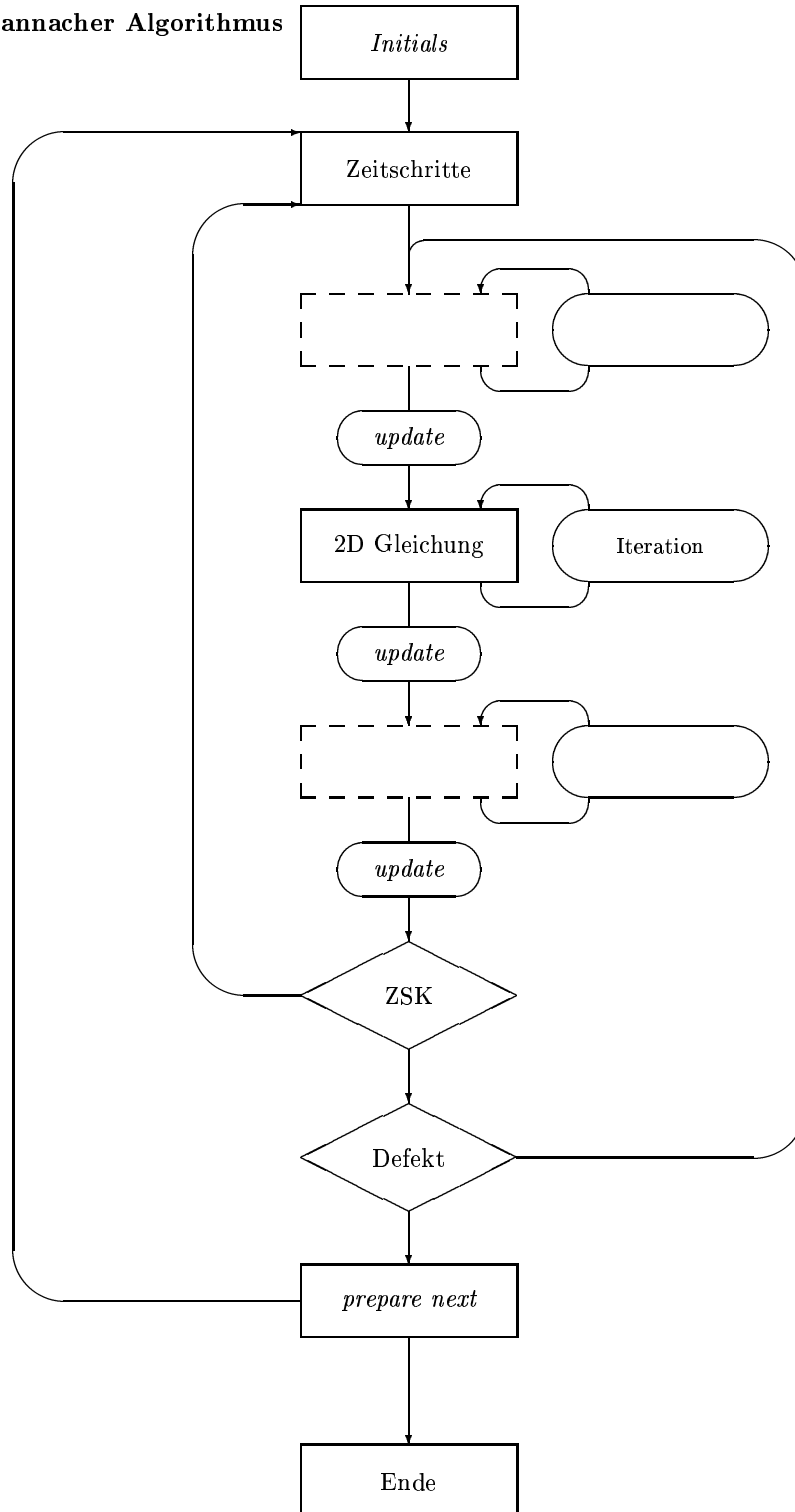
Figure 4.1: The Hujeirat-Rannacher algorithm as implemented in Nemesis. Figure courtesy Keller.

4.2 Physical splitting and time-step control

Hujeirat and Rannacher introduced a new algorithm (see Hujeirat and Rannacher, 1998; Hujeirat, 1998, for a slightly modified version thereof) to solve the Navier-Stokes equations which consist of the so called physical splitting. The implicit finite difference or finite volume method can be summarized as

$$\mathsf{A}\boldsymbol{U} = \boldsymbol{b}, \tag{4.9}$$

where $\boldsymbol{U}$ is a vector containing the state vector at the new time-step $\boldsymbol{u}_j^{n+1}$ for all nodes j, $\boldsymbol{b}$ contains the state vector at the old time-step $\boldsymbol{u}_j^n$ and possibly additional sources for all nodes j. The matrix A is build up to represent the discretization of the differential operator L and also contains the time advancement through Δt. The solver is required to invert the matrix A yielding A^{-1} to solve for the new state vector. A is a sparse matrix, because the discrete version of operator L only includes a finite number of next neighbors arranged along the diagonal of A, while the coupling between the state variables $^{\alpha}u$ is represented as off-diagonal entries. Direct solvers for sparse matrices are computationally very costly.

If the time-step Δt is low, the off-diagonal entries will have only small weight in the computations of $\boldsymbol{U}$. So the idea of the physical splitting is to divide the vector $\boldsymbol{U}$ up into smaller units $^{\beta}U$ (where each $^{\beta}U$ contains one or more state variables $^{\alpha}u_j$) depending on the strength on the coupling between them. The same is done with the matrix A, thus obtaining a number of sub-matrices $^{\beta}\mathsf{A}$. The matrices $^{\beta}\mathsf{A}$ have very simple structure and are only populated around the diagonal, at least in the best case where $\beta = \alpha$. Hence they can be inverted very efficiently. In this way we reduced the large problem (4.9) into smaller portions, e.g.

$$\begin{array}{rcl} ^{\rho}\mathsf{A}\,^{\rho}\boldsymbol{U} & = & ^{\rho}\boldsymbol{b} \\ ^{v,e}\mathsf{A}\,^{v,e}\boldsymbol{U} & = & ^{v,e}\boldsymbol{b} \end{array} \tag{4.10}$$

where $\beta = \beta_1 = \rho$ would solve the continuity equation and $\beta = \beta_2 = (v, e)$ would solve the coupled momentum and energy equations, respectively. The drawback of this procedure is, that the coupling between the state variables $^{\alpha}u$ may be neglected. It is thus necessary (1) to update all dependant variables after each β-solver and (2) to globally iterate the whole system of β-solvers until the coupling between the state variables converges.

In this context we stress, that the order in which the equations are solved has a large impact on the convergence behavior. For instance. we solve in the order (l, ρ, e, p_R, u), where l is the angular momentum, ρ density, e internal energy, p_R radial momentum and u radiation density. Changing this scheme to (l, ρ, p_R, e, u) does not significantly change the convergence behavior, while the order (l, ρ, p_R, u, e) results in a average time-step, which is two orders of magnitude lower. The problem is further severed by the fact, that the optimal order depends on the type of application (e.g. cold disk, spherical flow, etc). As a rule of thumb one should evaluate the equation with the most couplings last. This would in our case be the energy equation. But in this particular

application of ADAF-SSD transitions, the radiative transfer is strongly coupled to energy equation in the transition region. There the balance of radiative cooling and turbulent convective heating is very delicate. The consequence is, that the time-step is very low if u is not solved for last.

The efficiency in terms of large time-steps Δt of this method will in general be lower than that of a full solver, which uses the full matrix A. On the other hand, the efficiency in terms of computing resources necessary to invert the matrices $^\beta\mathsf{A}$ may be considerably higher depending on the problem and the employed splitting of the equations. It is very difficult to estimate a priori the optimal time-step Δt where the algorithm is most efficient in terms of overall advanced physical simulation time over computational CPU-time. This is further complicated by the fact that the optimal Δt may change during the simulation as a result of changing flow properties. For example the flow might initially be very steady, but later self-consistently develop strong turbulence, which would require smaller time-step in order to lessen the number of iterations needed.

In order to circumvent this problem, one may use an adaptive time-step control. If the full system does not reach global convergence within a pre-defined number of iterations, the state variables are reset to their old values $\boldsymbol{u}^n$, the time-step Δt lessened and the global iteration restarted. On the other hand, if the system reaches convergence very fast for a number of consecutive time steps n, the time-step advancement Δt is increased. Another possibility to improve the efficiency is to make an explicit estimate for the new state variables before entering global iteration. Depending on the error of the explicit estimate compared to the implicit calculations, one can also increase or decrease the time-step advancement Δt.

This time-step control (in German *Zeitschritt Kontrolle, ZSK*) together with the physical splitting is, what we call the *Hujeirat-Rannacher algorithm*, which is illustrated in figure 4.1. The implementation of this algorithm by Keller (2000) is described in the next section.

4.3   The numerical code Nemesis

The numerical code we used has been developed by Christof Keller (ITA, Heidelberg) an was simply called *System1D*. Originally, it did not include an energy equation, neither for gas nor for radiation. We adapted the code to our needs and implemented the missing energy equations. This branch of the code has meanwhile been named *Nemesis*.[2]

The code consists of three main parts, illustrated in figure 4.2. The first one implements a tensor product grid (TPG) on a staggered mesh. The module `Mesh` is responsible for the initialization of the grid. It also provides many

---

[2]simply because it is the final fate of the gas to vanish into the blackhole (and because it gave me sometimes such hard time, also ;-)
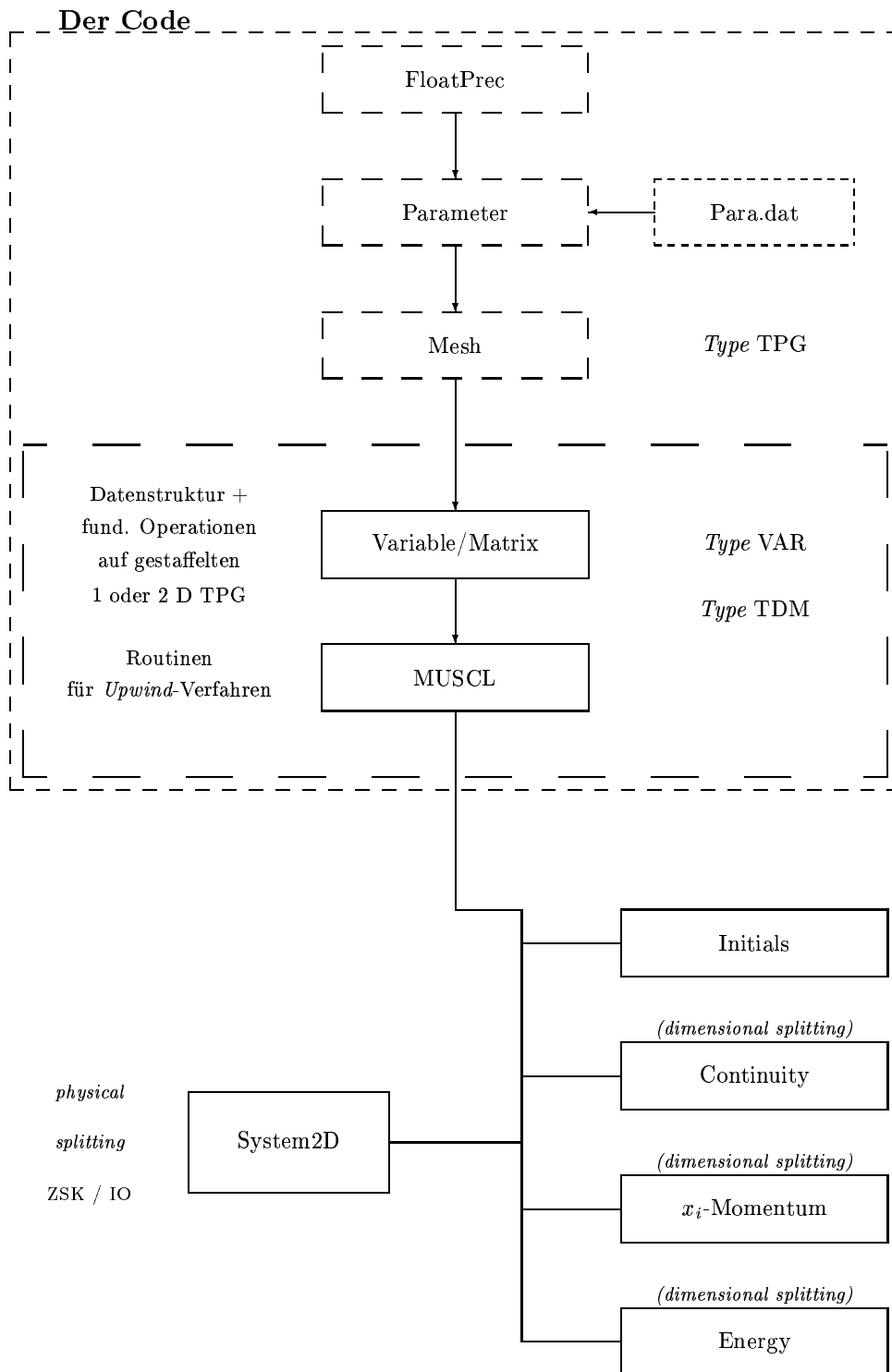
Der Code

FloatPrec

Parameter ← Para.dat

Mesh — *Type* TPG

Datenstruktur +
fund. Operationen
auf gestaffelten
1 oder 2 D TPG

Variable/Matrix — *Type* VAR

Type TDM

Routinen
für *Upwind*-Verfahren

MUSCL

Initials

(dimensional splitting)

Continuity

physical

splitting

System2D

ZSK / IO

(dimensional splitting)

x_i-Momentum

(dimensional splitting)

Energy

Figure 4.2: Structure of the numerical code Nemesis. Figure courtesy Keller.

additional properties of the grid, like volume, face surface area, etc, for the individual nodes. These are made available to the upper layers.

The second part consists of two modules. The first called `Var2D` implements scalar type variables, centered on the grid nodes, and vector type variables, living on the zone edges. The second called `Matrix` does likewise for band matrices. These modules do also provide a large range of operators which act on the data type. The range of operators starts from simple ones as the product of two variables or interpolation onto the staggered mesh, and ends with complicated calculation like the Jacobian of the general diffusion operator. The advective scheme, implemented as a finite volume method, is split off into the module `Muscl` (Monotonic Upstream-centered Scheme for Conservation Laws). Note that these three modules and the underlying `Mesh` do in principal support 2-dimensional data space. This has not been tested and at the moment the second dimension is only one zone wide.

The third part consists of the physical equations to be solved. Every equation is implemented in separate module (called `Continuity`, `Momemtx2`, `AngMom`, `Energy` and `Radiation`), which provides calculation of the defects and a local solver. The calculation of the shear tensor and its various derivatives is split off into the module `Viscosity`. They totally rely upon the underlying modules `Var2D` and `Matrix` to do the dirty work.

These three parts are framed by the main module `System2D` which, after some initialization, enters the main loop and does also provide the times-step control system.

4.4   Test problems

The foundations of the code have been extensively tested by Keller (2000, 2002). It was originally meant to be applied to cold disks, which are very well described by cylindrical geometry. The largest uncertainty at the beginning of this work, was how the code would cope with essentially spherical flows like Bondi accretion or quasi-spherical flows like ADAFs or slim disks, generally. Another possible pitfall was the behavior of the code at critical sonic points, where the flow undergoes a transition from sub-sonic to super-sonic. At the sonic point the nominator and denominator, N and D, of the derivative of velocity, diverge simultaneously. For numerical stationary models this is a non-trivial problem (see e.g. Peitz and Appl, 1997). The last question is how the code operates when large gradients, like in ADAF-SSD transitions, are present.

We thus present a selection of two test problems. The first is the spherical Bondi accretion, where a central mass spherically accretes matter from infinity. This tests the quality of the spherical flows in cylindrical coordinates, and the behavior at the sonic point. The analytical solution to this problem is discussed in detail by Chakrabarti (1990).

The second test is an ADAF, where the outer boundaries are taken to be SSD-like. Therefore large gradient are present near the outer boundary. The flow is
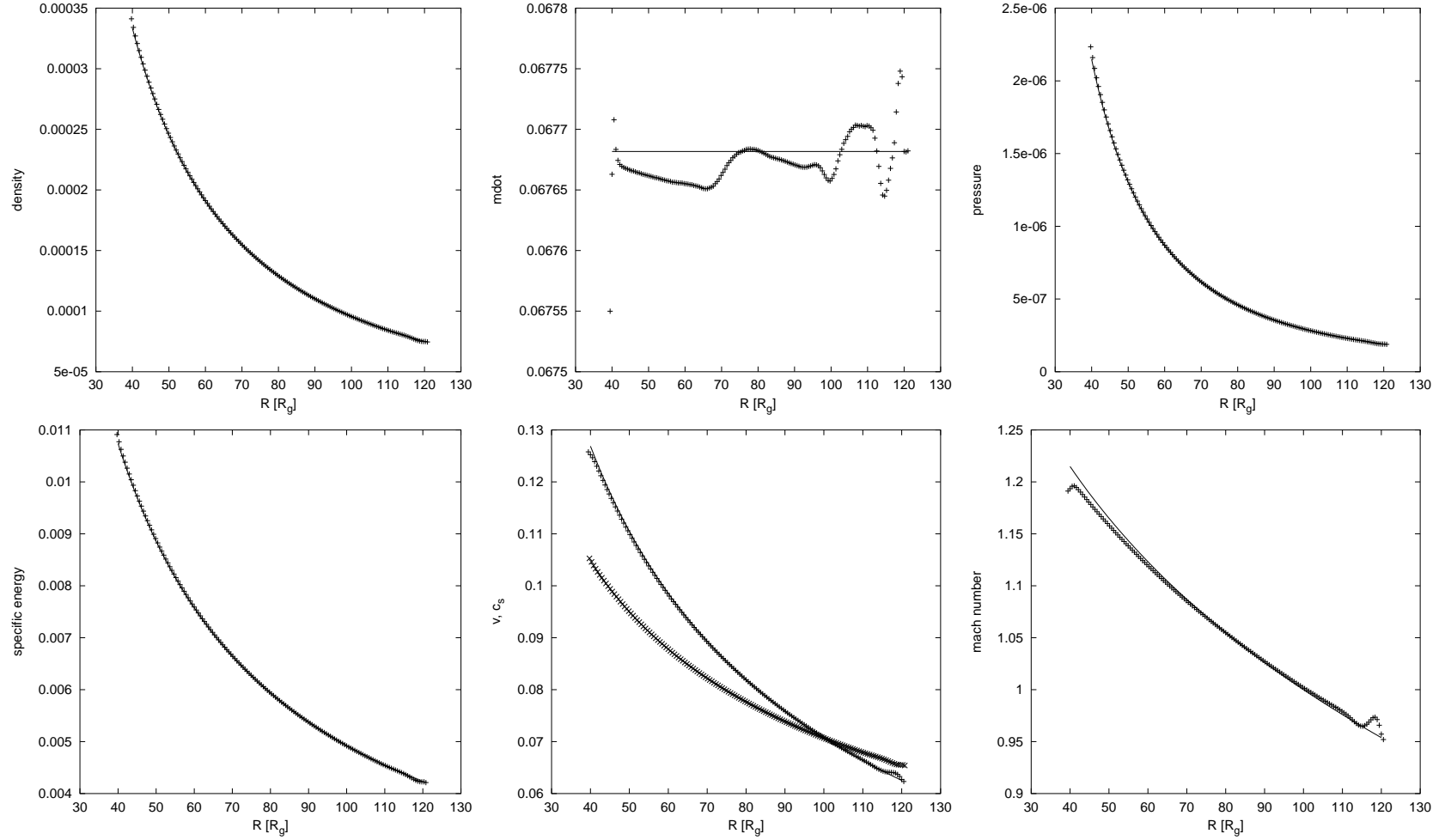
Figure 4.3: Test problem: spherical Bondi-accretion. Comparison between numerical computation (*crosses*) and analytical solution (*lines*). The individual panels show from left to right and top to bottom: density ρ, accretion rate $\dot{m} = 4\pi\, v\, \rho R^2$, pressure p, specific internal energy $\varepsilon = \rho/e$, infall velocity v and sound speed c_s, mach number $m = v/c_s$.
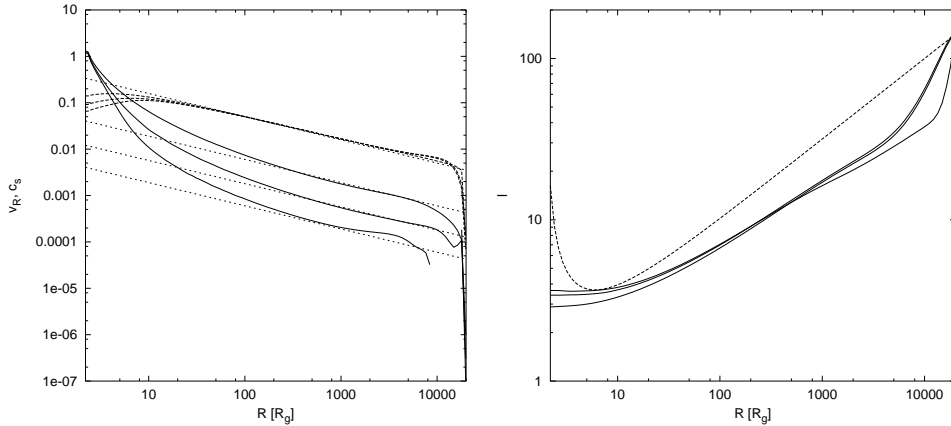
Figure 4.4: Test problem: Global transonic ADAF solutions with SSD outer boundary conditions for three values of $\alpha = (0.01, 0.03, 0.1)$. α increases from bottom to top in both panels. The left panel shows radial velocity v_R (*solid*) and sound speed c_s (*dotted*), and the analytical values of the self-similar solution (Narayan and Yi, 1994), respectively. The right panel shows specific angular momentum l (*solid*) and for comparison the keplerian counterpart l_K. This figure can be directly compared to figure 3.1

also transonic and quasi-spherical, such that all three uncertainties are present simultaneously. Narayan et al. (1997b) studied this problem numerically.

Our numerical calculations are illustrated in the figures 4.3 and 4.4. For the Bondi problem the primary variables density and energy density (which is pressure times a numerical factor, only) are very well represented by the numerical results. The radial velocity is underestimated a bit in the inner parts. This discrepancy is best seen in the mach number M. The accretion rate is not constant at first glance, but the relative deviation from the analytical value is better than 3×10^{-4} and of the order of the demanded numerical accuracy. There are no problems at the sonic point. The small bumps near the outer boundary can be explained by the fact that we use constant values at the boundary's ghost cells. Linear extrapolation, or, if available, analytical values improve this significantly.

The results of the second test problem shown in figure 4.4 can be directly compared to the numerical models of Narayan et al. (1997b), shown in figure 3.1. The fluid velocity and sound speed are, away from the boundaries, very well described by the self-similar solution of Narayan and Yi (1994). The specific angular momentum in the inner part shows the same behavior as the models found by Narayan et al. (1997b). Only at the outer boundary l drops too fast. This simulations did only run for short time. It is a common observation, that our code needs fairly long to relax the specific angular momentum near the outer boundary. This is due to the larger azimuthal revolution time of the flow.

Chapter 5

Stationary ADAF-SSD Transitions

There have been a number of arguments to suggest that an accretion flow around a black hole may undergo a transition from a standard disk on the outer part to an ADAF on the inner part. The transition radius R_{tr} between the two zones has been estimated in some X-ray binaries by inferring the location of the innermost radius of the standard disk, either by fitting the soft component in the spectrum or from the width of the Hα line wings. The transition radius has also been estimated from the hard component of black hole X-ray binary (BHXB) spectra. Narayan et al. (1997a) showed that the spectra of quiescent BHXBs are well reproduced by an ADAF model with a large transition radius, $R_{tr} \sim 10^3 - 10^4 \, R_g$.

ADAF and SSD have very different dynamical and energetic structure. It is not evident that they can coexist in a small volume. The next section will discuss the requirements that an ADAF must satisfy in order to connect to an outer standard disk. Then we present numerical simulations of such ADAF-SSD transitions and look in detail into the dynamical and energetic structure of the transition region. In the last section we discuss the allowed range for the location of the transition radius. Throughout this chapter we will concentrate on the quasi-stationary structure of the accretion flow. The discussion of the time-dependent behavior will be reserved for the next chapter.

5.1 Connection conditions

Again we note that the physical state of accreting gas in an ADAF is very well described by the self-similar solution found by Narayan and Yi (1994) (e.g., Chen et al., 1995). If an inner ADAF is to be connected to an outer SSD, it must satisfy certain connection conditions. Three of them have been identified in the literature (e.g., Manmoto et al., 2000).
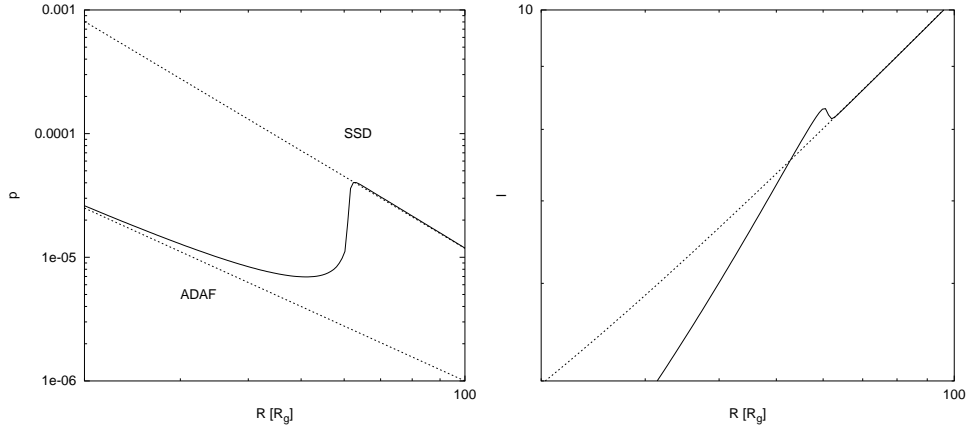
Figure 5.1: Numerical calculations of the structure of the transition region. Left panel: pressure p in the transition region. Dashed lines illustrate the trend of the analytical solutions. Right panel: specific angular momentum l (*solid*)and the keplerian value l_K (*dashed*). Whenever the transition region is narrow, pressure takes both, a minimum and a maximum, near the transition. This results in super-keplerian rotation in the transition region. (See text for detailed discussion.)

According to the self-similar solution, the temperature of the accreting gas is close to the virial temperature and the radial velocity is approximately α times the free-fall velocity. This is a direct consequence of the advective nature of the accretion flow. On the other hand these quantities are orders of magnitude smaller at the same radius for a standard disk. So the first and most evident connection condition is that thermodynamical quantities like temperature and dynamical like radial velocity must change by orders of magnitude in the transition region. This is somewhat realized in global stationary ADAF models where thin standard disk-like outer boundary conditions are imposed. See for example the results of Narayan et al. (1997b) and our results in figures 3.1 and 4.4, respectively.

The second requirement concerns the rotation of the flow. Let us denote the finite radial extent of the transition region by δ. Abramowicz et al. (1998) noted that the accreting gas in an ADAF near the transition radius must rotate at super-keplerian angular velocity whenever the transition region is narrow, i.e. $\delta \ll \mathrm{R_{tr}}$. As can be seen in figure 5.1, the pressure takes necessarily two extrema – and thus vanishing gradient – in the transition region. After neglecting the inertial term in the radial force balance, $\partial_R P = \Sigma(\Omega^2 - \Omega_K^2)R$, it follows that the angular velocity crosses the keplerian value twice. Hence we have $\Omega > \Omega_K$ in the transition region.

The last and most important requirement is that an ADAF which is connected to an outer SSD must have an outward energy flux (Kato and Nakamura, 1998). The total energy flux passing through a cylindrical surface at radius R is positive and equal to $(3/2)(GM\dot{M}/R)$ for every steady thin disk model (see eq 3.8).

This quantity, in contrast, is negative for the self-similar ADAF solution (see eq 3.20). Hence an ADAF that is connected to a SSD at radius R_{tr} must have a positive total energy flux larger than $(3/2)(GM\dot{M}/R_{tr})$. Otherwise the ADAF cannot connect thermally to the outer standard disk, since radiation losses will inevitably occur at the transition radius.

Honma (1996) was the first to construct steady state models which satisfy the connection condition. Later Manmoto et al. (2000) and Manmoto and Kato (2000) extended his work and presented self-consistent stationary models with ADAF-SSD transitions. This present work reanalyzes their results and continues further along this track to study the generic time-dependency of such models in the next chapter.

5.2   Dynamics of the transition

The most important ingredient for ADAF-SSD transitions is energy transport by turbulent convection (see eqs 3.31 and 3.33). This makes the total outward energy flux of convective ADAFs positive and satisfies the third connection condition for a wide range of parameters.

We study the dynamics of ADAF-SSD transition using numerical simulations. As a first step we do not solve the full system of equations (2.53 - 2.72), but ignore radiative transfer. The transition radius is treated as a free parameter. While solving the energy equation (2.56) we neglect radiative losses in the ADAF ($R < R_{tr}$), and further assume that viscous heating and radiative losses exactly balance in the SSD, i.e. $Q_{rad}^- = Q_{vis}^+$ for $R > R_{tr}$. We call this the "dynamical approach" as it reproduces locally the dynamical structure of ADAF and SSD solutions, respectively. Turbulent convection is taken into account, but has only small impact on the dynamical structure of the flow away from the transition. This global model is clearly not self-consistent, though Manmoto and Kato (2000) showed that this procedure describes very accurate the dynamics of ADAF-SSD transitions if the transition radius is known *a priori*. In the next section 5.3 we contrast the dynamical approach with the solution of the full system of equations and discuss its impact on the energetics of the transition region.

We calculated ADAF-SSD transition models with different transition radii R_{tr} and for comparison additionally pure SSD models extending down to the event horizon. Figure 5.2 illustrates the numerical results. The SSD behaves as expected. At the marginally stable orbit (where l_K is minimal) the disk is truncated and gas flows essentially in free-fall into the black hole. Here the inertial terms in the radial momentum and energy equations become dominant, so that both temperature and density drop.

ADAF-SSD models reproduce very accurate pure SSD models in the outer parts. Inward of the transition they agree very well with transonic ADAF solutions. At the transition radius the disk thickens in vertical direction. Density drops by
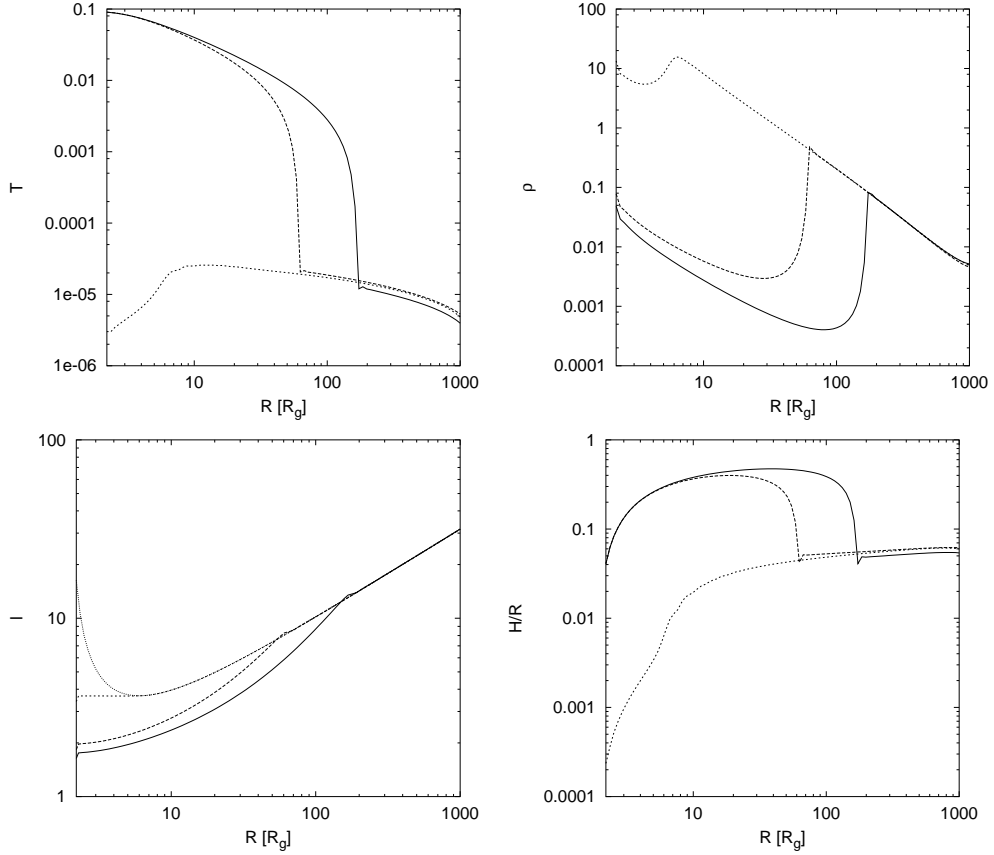
Figure 5.2: ADAF-SSD transition models for different transition radii $R_{tr} = 0$, i.e. pure SSD models (*short dashed*), $R_{tr} = 60 R_g$ (*dashed*) and $R_{tr} = 160 R_g$ (*solid*). The individual panels show temperature T (upper left), density ρ (upper right), relative disk height H/R (lower right), specific angular momentum l and the keplerian specific angular momentum l_K (lower left), respectively.

several orders of magnitude, thereby radiative processes become very inefficient and the temperature increases accordingly. In the transition region gas rotates at super-keplerian velocities as expected (see also figure 5.1 for a close-up), immediately inward of the transition the specific angular momentum l drops far below l_K. The flow is no longer stabilized by rotation so that the radial velocity also increases by several orders of magnitude such that pressure support is reached.

The radial extent of the transition region δ depends on the adiabatic index γ (Manmoto and Kato, 2000). In general we assume an ideal gas with $\gamma = 5/3$, but even fully ionized pressure dominated plasma will deviate significantly from this value in the presence of weak magnetic fields so that $\gamma = 4/3$ seems often more appropriate. The adiabatic index determines the radial dependency of the entropy and thus of convective energy flux through the transition. We expect broader transition regions δ for smaller γ.

The radial force balance is plotted in figure 5.3. The structure of the SSD part
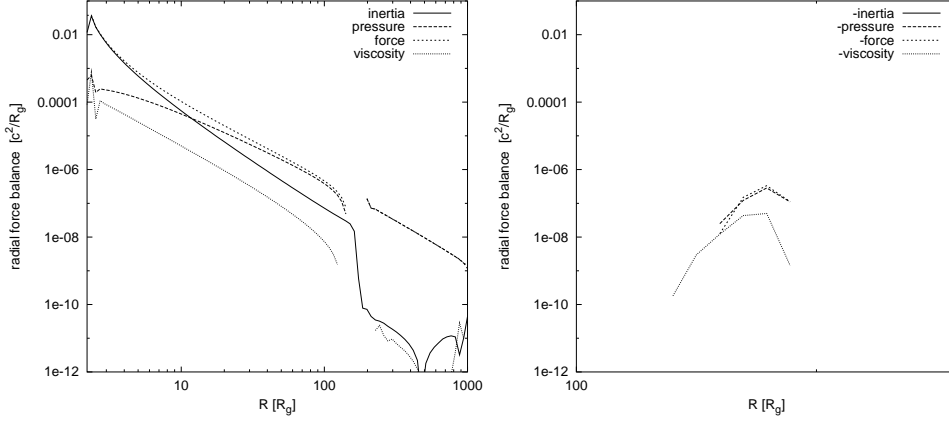
Figure 5.3: Radial force balance of ADAF-SSD transition model (here $R_{tr} = 160\,R_g$). The individual terms of the radial momentum equation are inertia $\Sigma v_R \partial_R v_R$ (*solid*), pressure gradient $-\partial_R P$ (*dot-dashed*), effective gravity $-\Sigma(\Omega^2 - \Omega_K^2)R$ (*dashed*), and internal viscous stress $(\boldsymbol{\nabla}\cdot\tau)_R$ (*dotted*). The left panel shows contributions with positive sign. In the transition region all forces but inertia change sign. This is shown in a close-up on the transition region in the right panel.

is given – as expected – by exact balance of effective gravity and radial pressure gradient, i.e. $g_{eff} = -\Omega_K^2 R + \Omega^2 R = -1/\Sigma \partial_R P$. Inertia and viscous stress are completely negligible. In the ADAF the sum of pressure gradient and effective gravity is balanced by inertia, only in the innermost parts, where the flow is transonic, does gravity take over and the pressure gradient is almost negligible.

The situation in the transition region is again different. Effective gravity changes sign as does the pressure gradient. This is a direct consequence of the super-keplerian rotation. Surprisingly, force balance is established with the internal viscous stress $(\boldsymbol{\nabla}\cdot\tau)_R$ rather than inertia (which does not change sign and drops off sharply). The internal viscous stress is a non-neglible contribution to the force balance in the transition region. With our symmetry assumptions, the only non-vanishing contribution to the radial internal stresses is the τ_{RR}-component of the total stress tensor. In this regard our model is more complete than previous calculations in the literature, including Manmoto and Kato (2000), who consider the $\tau_{R\phi}$-component in the angular momentum equation, only. We conclude that it is essential to include all components of the stress tensor for a complete understanding and consistent modeling of ADAF-SSD transition models.

5.3 Energy budget of the transition

So far we did not solve the full energy equation nor the radiative transfer equation. A self-consistent model requires solving the full system (2.53-2.72). Nonetheless it is interesting to contrast both approaches. Figure 5.4 shows
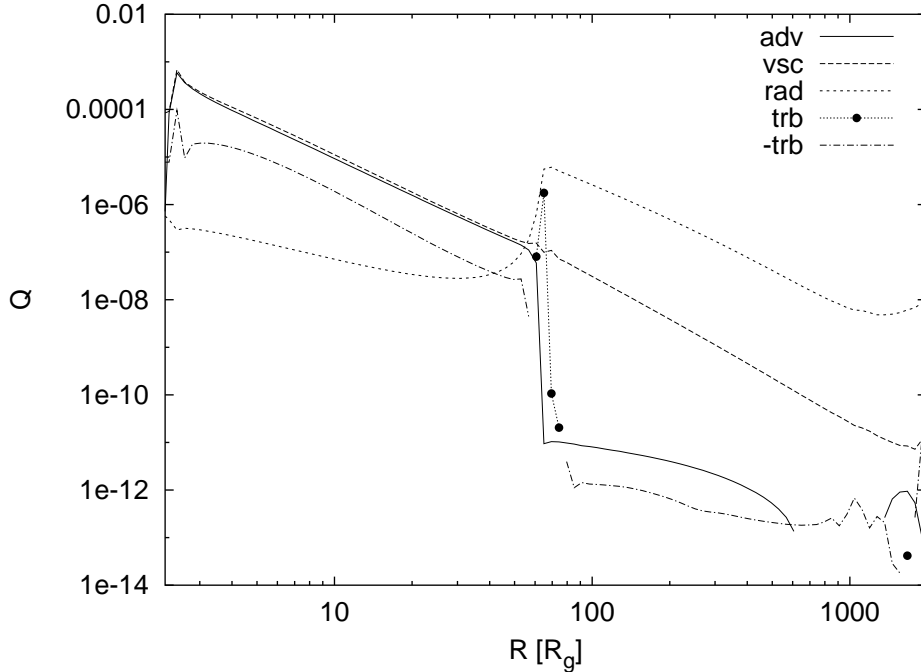
Figure 5.4: Energy balance of "dynamical approach" ADAF-SSD solutions where the transition radius is a free parameter (here $R_{tr} = 60\,R_g$). The contributions are advective cooling Q^-_{adv} (*solid*); viscous heating Q^+_{vsc} (*long dashed*); turbulent convective transport Q^+_{trb} (*dotted*) and $-Q^+_{trb}$ (*dot-dashed*). The radiative cooling rate Q^-_{rad} (*short dashed*) is not (self-consistently) included in the calculations and only shown for comparison. The numerical resolution in the transition region is poor as indicated by the dots on top of Q^+_{trb}.

the individual contributions to the energy balance for the purely dynamical approach, while 5.5 illustrates the energy balance for the full system.[1]

In the inner ADAF advective cooling Q^-_{adv} and viscous heating are of the same order of magnitude while turbulent convective energy transport is only a minor but non-negligible contribution. Turbulent convection transfers energy outward as expected. Radiative cooling in the inner ADAF part is dynamically negligible as seen from figures 5.4 and 5.5

In the outer SSD part we have previously assumed that viscous heating and radiative cooling balance exactly. This is clearly not the case and hence the "dynamical approach" model fails to reproduce the correct solution. There the plasma is still much to hot and cooling does not match heating. The exact treatment shows that the plasma is rapidly cooled down to its equilibrium state as can be seen in figure 5.5.[2] Advective cooling and turbulent convection are completely negligible in the SSD, both for the dynamical approach and the full

---

[1]The results of the dynamical approach have been used as initial conditions for the full self-consistent modeling.

[2]The outermost parts did not reach equilibrium at the time of this snapshot, but do so at later times.
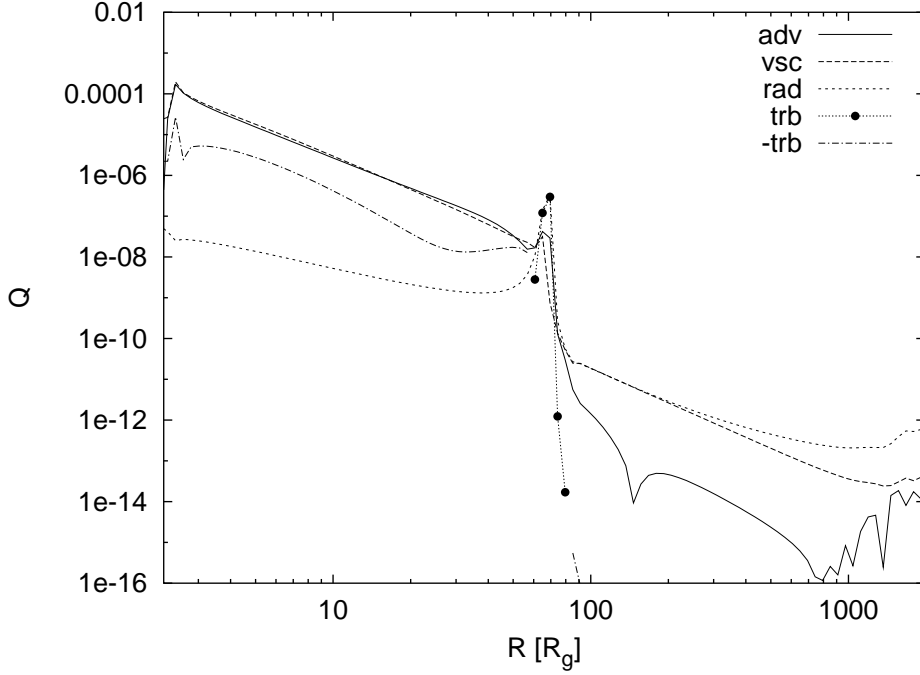
Figure 5.5: Energy balance of self-consistent ADAF-SSD solutions (here $R_{tr} \approx 60\,R_g$). The contributions are advective cooling Q_{adv}^- (*solid*); viscous heating Q_{vsc}^+ (*long dashed*); turbulent convective transport Q_{trb}^+ (*dotted*) and $-Q_{trb}^+$ (*dot-dashed*). The radiative cooling rate Q_{rad}^- (*short dashed*) is treated self-consistently by solving the full system. The numerical resolution in the transition region is poor as indicated by the dots on top of Q_{trb}^+.

model.

The most interesting part is the transition region. There advective cooling drops off by 3-4 orders of magnitude. The flow is much slower in the outer parts. Turbulent convection on the other hand changes sign and rises steeply. This is due to a sudden drop of temperature in the transition which implies a very low and ineffective energy flux. Energy is accumulated by convective transport in the transition region. The only possibility to shed this energy surplus is by increased radiative losses. As seem in figure 5.5 the radiative cooling rate also increases strongly in the transition region and does provide the needed cooling mechanism. The exact treatment shows that radiative cooling Q_{rad}^- and turbulent convection balance to a high degree in the transition region. The strong increase of the radiative cooling rate is even observed in the dynamical model, though it does not exactly balance Q_{trb}^+ as expected. (We note that our model could benefit from higher resolution in the transition region by better resolving the large gradients of all physical variables.)

The energy density of the radiation field u is plotted in figure 5.6. It is strongly peaked in the transition zone as expected. Radial diffusion from the adjacent SSD deposits lots of photons in the transition region. A second maximum is located near the inner boundary.
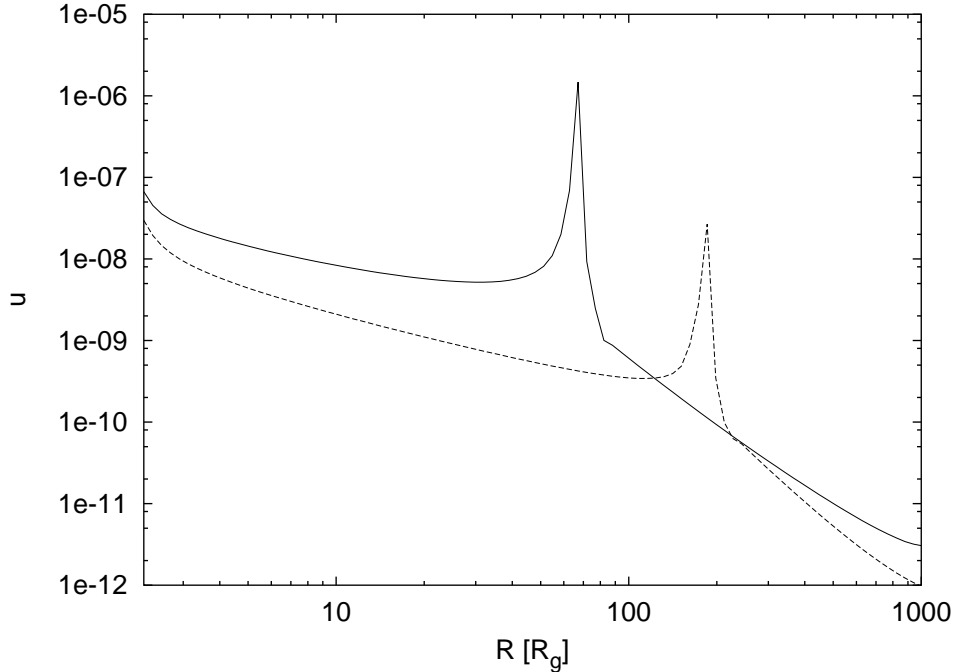
Figure 5.6: Radiation field energy density u of ADAF-SSD models with different transition radii $R_{tr} = 60\,R_g$ (*solid*) and $R_{tr} = 160\,R_g$ (*dashed*). A prominent peak appears in the transition radius. A second maximum is located near the inner boundary.

Further insight into the energetics of the transition region is revealed by studying the balance of sources and sinks of the radiation field u. The corresponding cooling and heating rates are shown in figure 5.7. In the SSD part thermal sources $Q^+_{src} = Q^-_{rad}$ and radiative losses through the upper and lower disk surfaces Q^-_{esc} are perfectly balanced. Radial diffusion does not play any role. In the ADAF part thermal sources are only a minor contribution. The bulk of photons is injected radially from the transition region and streams through the optically thin flow. Only at the inner boundary are Q^+_{src} and $-Q^-_{diff}$ comparable. In the transition region the radial diffusion rate changes sign, such that the radial diffusion flux takes its local minimum. Q^-_{diff} peaks sharply and balances the thermal sources. Most of the radiation thus originates from the transition region. It is either radiated directly or streams through the ADAF and escapes ultimately near the black hole.

The energetical structure of ADAF-SSD transitions is thus far from being simple. On one hand turbulent convection transfers internal energy from the innermost ADAF into the transition region and hence heats the cold SSD material. Simultaneously the radiation field is supplied with thermal photons from the transition region. The intensity of the radiation field on the other hand is further amplified by radial injection of photons from the cold SSD. This obviously delicate balance of multiple cooling and heating channels is what determines the position of the transition radius.
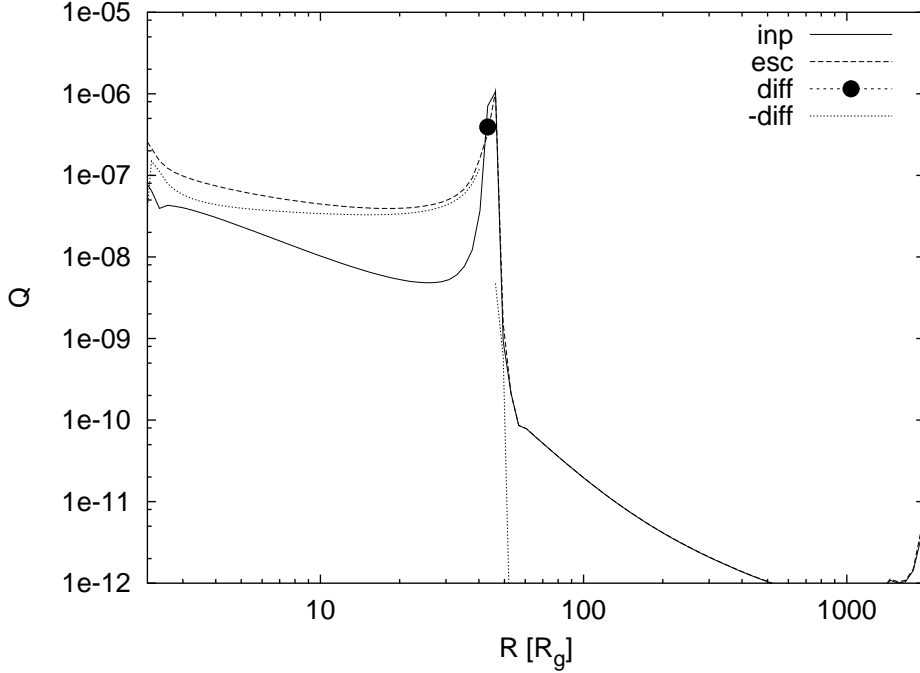
Figure 5.7: Balance of inputs and outputs of the photons in ADAF-SSD transition models (here $R_{tr} = 40\,R_g$). The individual contributions are thermal sources Q^+_{src} (*solid*), vertical irradiation through the surfaces Q^-_{esc} (*long dashed*) and radial diffusion Q^-_{diff} (*short dashed*) and $-Q^-_{diff}$ (*dotted*), respectively. In the ADAF part thermal sources are only a minor contribution, photons are instead injected radially from the transition region and stream through the ADAF. Only near the inner boundary is Q^+_{src} comparable with $-Q^-_{diff}$. In the SSD part radial diffusion does not play any role. Photons escape through the surface of the disk. In the transition region radial diffusion changes sign and peaks strongly to balance the thermal sources. In this snapshot, this is barely resolved as indicated by the dot on top of Q^-_{diff}.

5.4 Location of the transition radius

Honma (1996) and especially Manmoto and Kato (2000) were the first to consider stationary ADAF-SSD transitions with turbulent convective transport as main ingredient. They found strong dependency of the possible location of the transition R_{tr} on mass accretion rate $\dot{m}$ and the parameter α_T/α (see figure 5.8). Surprisingly they found many possible transition radii for a given parameter set $(\dot{m}, \alpha, \alpha_T, \gamma)$.

For large accretion rates these are continously distributed between a maximum and a minimum R_{tr}. Even more surprising, when $\dot{m}$ is small, however, there is a forbidden zone between them (see right panel of figure 5.8). They also found, that ADAF-SSD transitions are only possible if α_T is larger than some critical value, i.e. $\alpha_T > 0$. For large α_T/α the range of possible transition radii is wide. For smaller α_T/α this range narrows until the maximum and the minimum
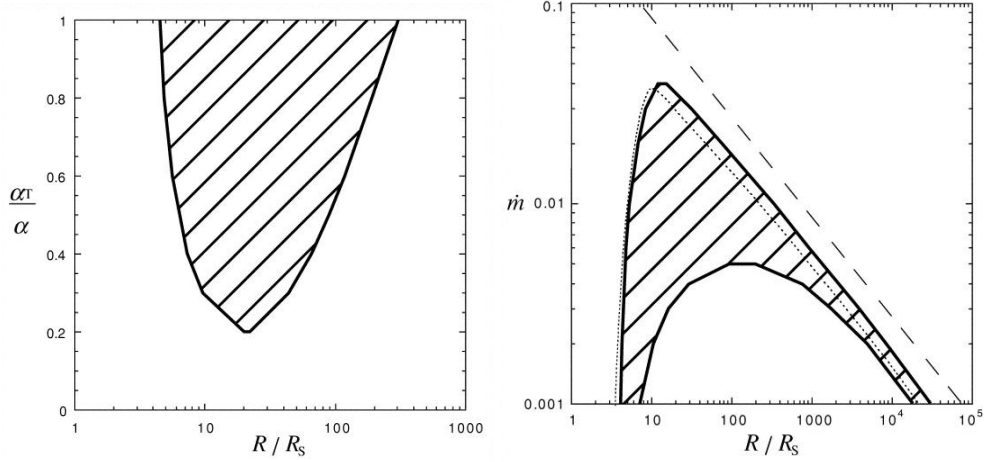
Figure 5.8: Location of the possible transition radii R_{tr} (*indicated as dashed area*) as function of α_T/α (left panel) and $\dot{m}$ (right panel). For the left panel $\alpha = 0.4$ and $\dot{m} = 0.01$, for the right panel $\alpha_T = \alpha = 0.4$ have been used. See discussion in the text. Figure adopted from (Manmoto and Kato, 2000).

transition radius coincide. For lower values of α_T/α a ADAF-SSD transition model is no longer found and the SSD extends down to the immediate vicinity of the black hole.

To understand this behavior lets take again a look at the energy flux near the transition region. Let $W(R)$ be the vertical integrated energy flux, which is the sum of fluxes related to kinetic, thermal and gravitational energy and fluxes due to viscous heating and convective transport, respectively (see eq. 3.32). Then the energy equation can be summarized as

$$\frac{1}{R}\frac{d}{dR}(RW) = -Q_{rad}^-. \tag{5.1}$$

If the the transition is to occur at radius R_{tr}, the relation

$$2\pi R_{tr}(W_{ADAF} - W_{SSD}) = 2\pi R_{tr}\int Q_{rad}^-\,dR \equiv 2\pi R_{tr}W_{rad} \tag{5.2}$$

must be satisfied at the transition radius R_{tr}, where the integration is performed over the narrow transition region. Here, W_{ADAF} and W_{SSD} are the vertical integrated energy fluxes just inside and outside of the transition.

As has been shown in chapter 3.3, $W_{ADAF} - W_{SSD}$ is mainly given by W_{trb} and the transition radius R_{tr} will thus be given approximately by

$$W_{trb}(R_{tr}) = W_{rad}(R_{tr}). \tag{5.3}$$

This is illustrated in figure 5.9, where we show a ADAF-SSD model with $R_{tr} \approx 60R_g$ on the left panel and $W_{trb}(R_{tr})$ and $W_{rad}(R_{tr})$ as functions of R_{tr} on the right panel. From the right panel we see, that condition for a transition (eq 5.3) is satisfied at two radii – the maximum and minimum transition radius.
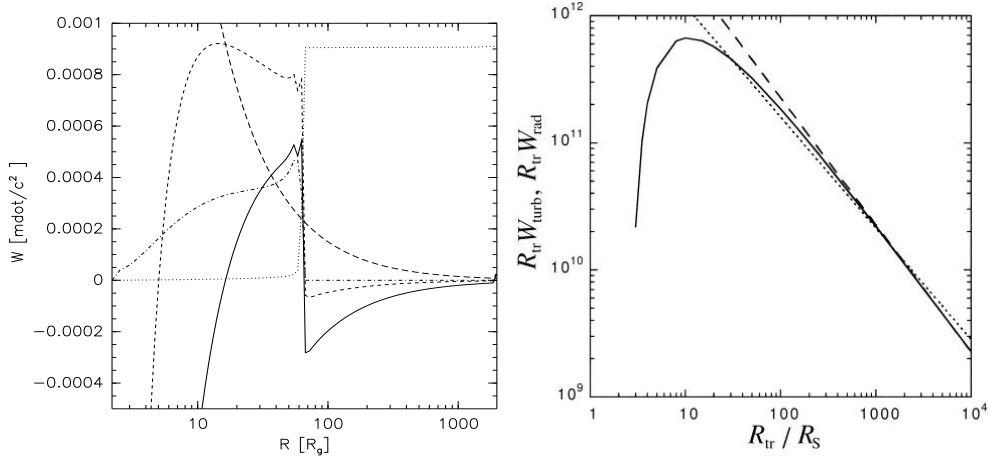
Figure 5.9: Energy flux W in ADAF-SSD models. The left panel shows total energy flux through the disk for a model with $R_{tr} \approx 60R_g$. Plotted are the energy flux of the ADAF W_{ADAF} (*short dashed*) and the SSD W_{SSD} (*long dashed*), their difference $W_{ADAF} - W_{SSD}$ (*solid*), which is approximately given by the turbulent flux W_{trb} (*dot-dashed*) and the radiation energy flux W_{rad} (*dotted*). The right panel is adopted from (Manmoto and Kato, 2000) and shows the dependency of W_{trb} (*solid*) and W_{rad} (*dotted*) on R_{tr}, if the transition is assumed to occur at R_{tr}. There are two possible transition radii where $W_{trb} = W_{rad}$.

So far we have only accounted for two possible locations of the transition. This due to the fact that we have neglected the influence of radiative cooling in the ADAF part in our analysis. If this is taken into account, the flow can adjust itself such that part of the turbulent convective energy is radiated in the ADAF part and need not be radiated in the transition zone. This effect broadens the interval of possible transition locations in the sense that radiation is strong enough to allow a transition in the vicinity of the maximum and minimum transition radius, also. This is also seen in the left panel of figure 5.9, where immediately inward of the transition W_{trb} (or W_{ADAF}) is still larger than W_{SSD}, such that their difference is still positive. Hence if part of W_{trb} would be radiated, the transition condition could also be satisfied for smaller radii (down to approx $R \approx (30 - 40)R_g$, where $W_{ADAF} < W_{SSD}$) than the present transition radius $R_{tr} \approx 60R_g$.

Radiative efficiency in the ADAF does strongly depend on the accretion rate $\dot{m}$, since density and optical depth scale with $\dot{m}$. It is most effective for large $\dot{m}$ and the transition is possible for a wide range of radii. For lower accretion rates only a small part of W_{trb} can be radiated and the possible locations of transition are restricted to values near to the minimum and maximum value, respectively. Hence even the prohibited zone the possible transition radius interval can be understood from this rather simple analysis.

From figure 5.8 we see that the spacing between the minimum and maximum transition radius grows with increasing α_T/α. This quantity is a measure for

61

the relative strength of turbulent heating Q_{trb}^+ to advective cooling Q_{adv}^-. Only if it is larger than a certain value does convection in the ADAF transport enough energy outward such that $W_{ADAF} > W_{SSD}$ – a necessary condition for ADAF-SSD transitions – in the first place. Hence there are no transitions for small values of α_T/α. If α_T/α grows, there is an increasing amount of energy supplied to the outer SSD, such that the minimum transition radius is locate far inward, where W_{trb} is still rising, or far out, where W_{trb} is dropping again relative to W_{rad}. In this way the dependency of the location of the transition radius on α_T can be understood, also.

We conclude by summarizing that after choosing a parameter set $(\dot{m}, \alpha, \alpha_T, \gamma)$, the transition condition 5.2 can be either not satisfied at all, hence a pure SSD solution, or satisfied for a range $\mathrm{R}_{tr}(min) \leq \mathrm{R}_{tr} \leq \mathrm{R}_{tr}(max)$. The reason is the availability of different cooling channels which allow for a thermal equilibrium for different transition radii R_{tr}, where the availability and effectivity of the cooling channels depend on $(\dot{m}, \alpha_T/\alpha)$.

Chapter 6

Time-dependent ADAF-SSD Transitions

This chapter is devoted to the time-dependent longterm evolution of ADAF-SSD transition models. The general behavior of our simulations is described first and we identify several properties of the solution. Some of these properties are discussed in detail before we conclude by revisiting the subject on possible locations of the transition radius. Throughout this chapters we measure time in units of keplerian orbital revolution times $P_K(R) = 2\pi R/v_K(R)$, either at the outer radius P_K, or at the transition P_K^{tr}.

6.1 The general picture

The longterm evolution of self-consistent ADAF-SSD transition models has been studied for a number of parameters. We used the models of the hydrodynamical approach as initial conditions. That is, our initial conditions do exhibit a transition from an inner ADAF to an outer SSD at a certain radius R_{tr}. Thus we cannot say anything about the onset of the transition or the mechanism which causes such transitions in the first place. We can only state whether self-consistent global solutions with transition at R_{tr} are possible and if so, how they evolve in time. We are specifically interested if the transition radius changes with time, i.e. $R_{tr} = R_{tr}(t)$.

We note that in the hydrodynamical simulations the transition radius was defined by being the radius inward of which we assumed $Q_{rad}^- = 0$ and outward of which $Q_{rad}^- = Q_{vsc}^+$, respectively. That is in the language of Narayan and Yi (1994), $f = 1$ for $R < R_{tr}$ and $f = 0$ for $R > R_{tr}$. The transition radius was a free parameter which had to be explicitly specified. In contrast here to, in our self-consistent models the transition radius does change according to the adjustment of the flow and has to be determined. For technical reasons[1] we use

---

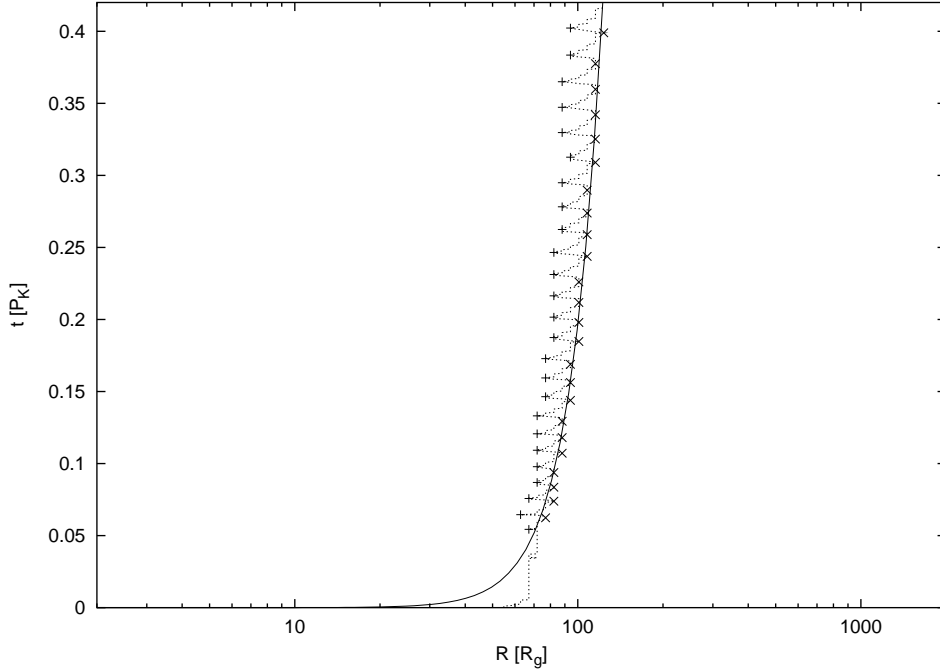[1]and also because this is what is usually done in the literature (eg. Manmoto and Kato, 2000)

Figure 6.1: Location of the transition radius R_{tr} (*dotted*) in time. The crosses $+$ and stars $\times$ mark the innermost and outermost position of the transition. The latter is fitted by an analytical function (*solid*) and identified with the intrinsic location of the transition, while the former is treated as a perturbation due to the oscillations in the transition region.

a slightly different definition of the transition radius based on the optical depth and define it as the radius at which the optical depth is unity, i.e. $\tau_R(R_{\mathrm{tr}}) = 1$. Conceptually this should be the same, at least in the limit of infinite numerical spatial resolution. In practice there might be small quantitative differences.

We further define the transition region by the radius interval where the rotation is super-keplerian, i.e. $l > l_K$. This is, according to the second connection condition (see section 5.1), a necessary condition for the existence of narrow ADAF-SSD transitions. We refer to the radial extent of the transition region as δ.

This said, let us turn to figure 6.2, which illustrates the evolution of a ADAF-SSD transition model where the transition was initially located at $R_{\mathrm{tr}}(0) \approx 60\,R_{\mathrm{g}}$. The transition is perhaps most easily seen in the temperature distribution, where the temperature changes from very high (orange) to very low (blue) without noticeable intermediate values. The transition zone is shown in the lower left panel, where only the transition region is colored. The total time shown is $t = 0.42\,P_K$, approximately half a keplerian orbital revolution at the outer boundary, this corresponds to roughly 80 orbital periods at the initial transition radius ($t = 78\,P_K^{tr}(60)$).

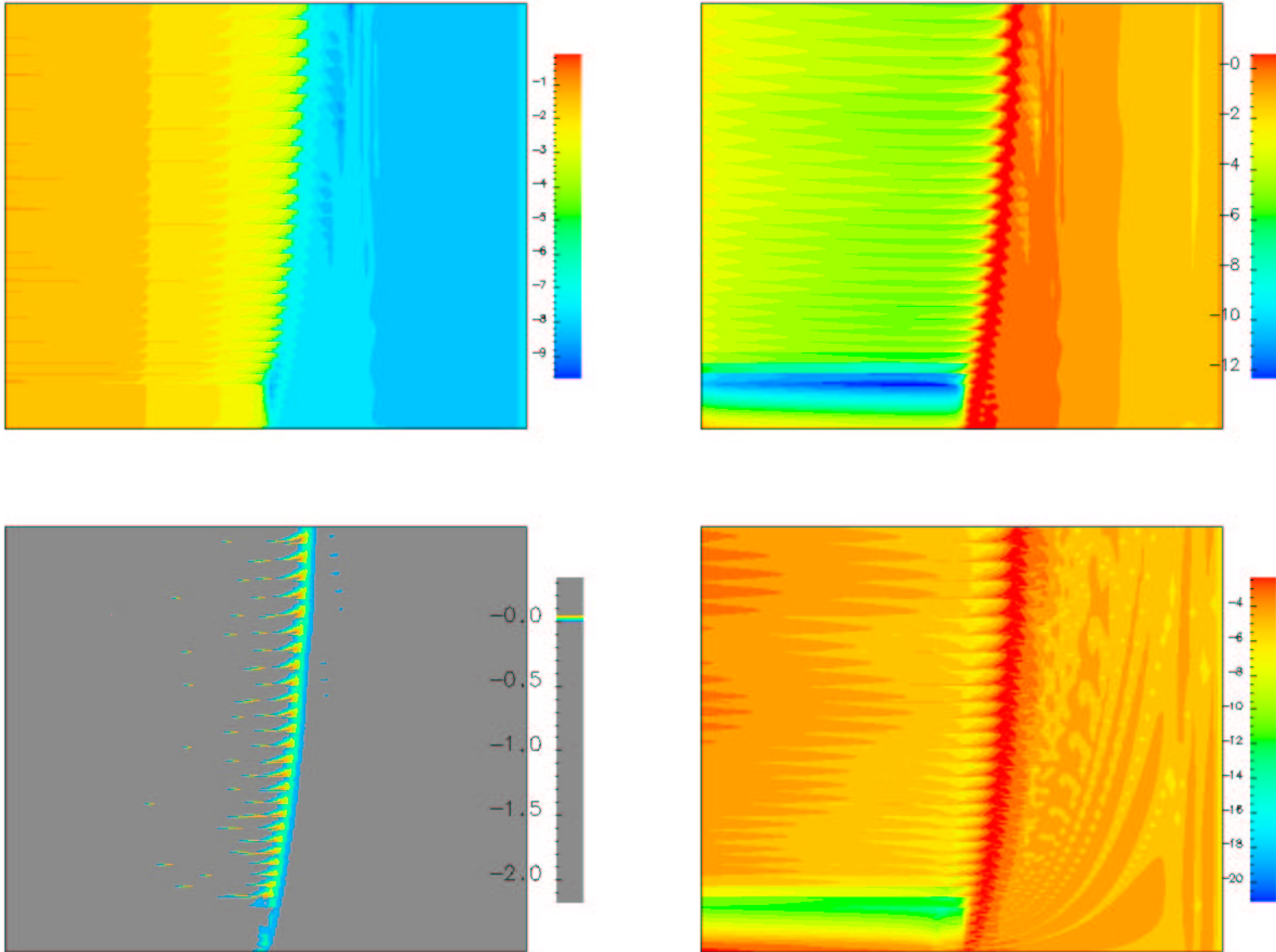It is immediately evident that both, the location of the transition radius (see

Figure 6.2: Evolution of ADAF-SSD transition models. On each panel radius $R = (2\mathrm{R_g} \cdots 2000\mathrm{R_g})$ increases from left to right on a logarithmic scale, while time $t = (0 \cdots 0.42\,P_K)$ runs from bottom to top on a linear scale. The individual panels show logarithm of temperature $\log T$ (upper left), logarithm of density $\log \rho$ (upper right), specific angular momentum l/l_K in units of the keplerian value l_k in the zone of super-keplerian rotation, ie. the transition zone (lower left) and logarithm of vertically integrated radial momentum density $\log p_R$ (lower right).
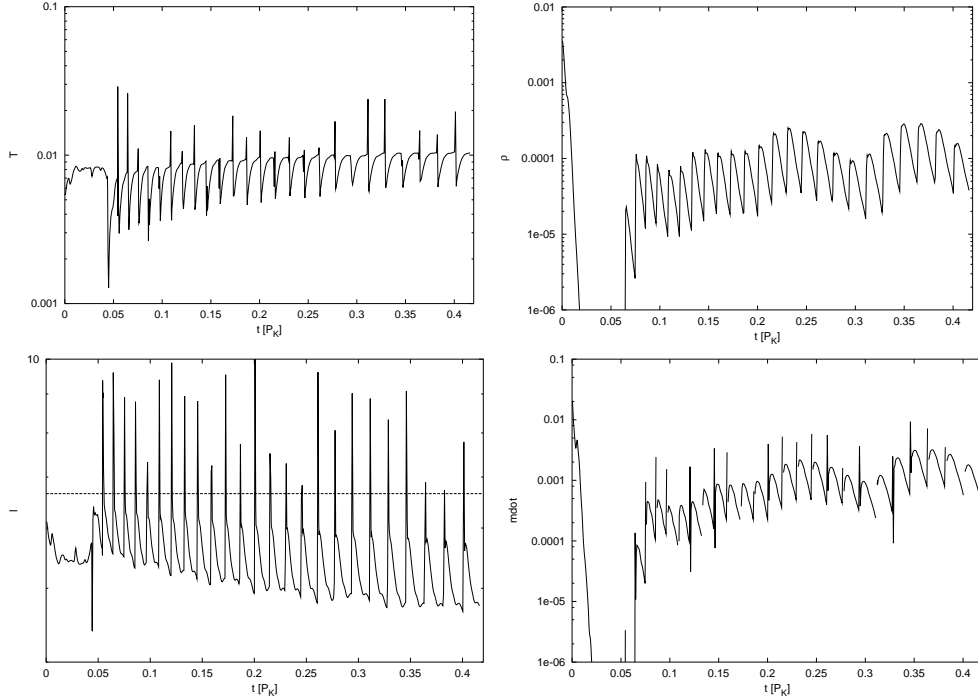
Figure 6.3: Evolution of ADAF-SSD transition models as function of time at a fixed radius $R = 40R_g$ inward of the transition. The individual panels show temperature T (upper left), density ρ (upper right), specific angular momentum l (*solid*) and the keplerian value l_k (*dashed*) (lower left) and accretion rate $\dot{m}$ (lower right).

also figure 6.1) and the radial extend δ of the transition zone, vary in time. We distinguish two major phase. The first is characterized by nearly constant transition radius. During this phase the flow tries to relax the imposed initial condition into a physical self-consistent global solution of the system of equations one uses. We call this the *relaxation phase*. In the course of this phase, momentum density p_R or mass accretion rate $\dot{m} \propto p_R R$ and density ρ drop continuously. This is because no matter is injected from the SSD into the ADAF, but rather accumulated in the transition region. The plasma in the ADAF part is rapidly drained and vanishes through the inner boundary. One could say that during this relaxation process, the ADAF and the SSD are not thermally and dynamically connected, but rather separated by an unphysical discontinuity.

This phase is computationally very costly as the time-step is very low. Some models do never leave this phase and cease to converge at all or do so at unacceptable low time-steps only. In this case no physical ADAF-SSD transition at or near to the initial transition radius is possible in our model.

The relaxation phase ends with the first blob of matter invading the ADAF from the SSD and restoring the mass accretion rate to its nominal value. One would expect that the further evolution of the model goes on continously along series of quasi-stationary solutions, where the transition radius and the other
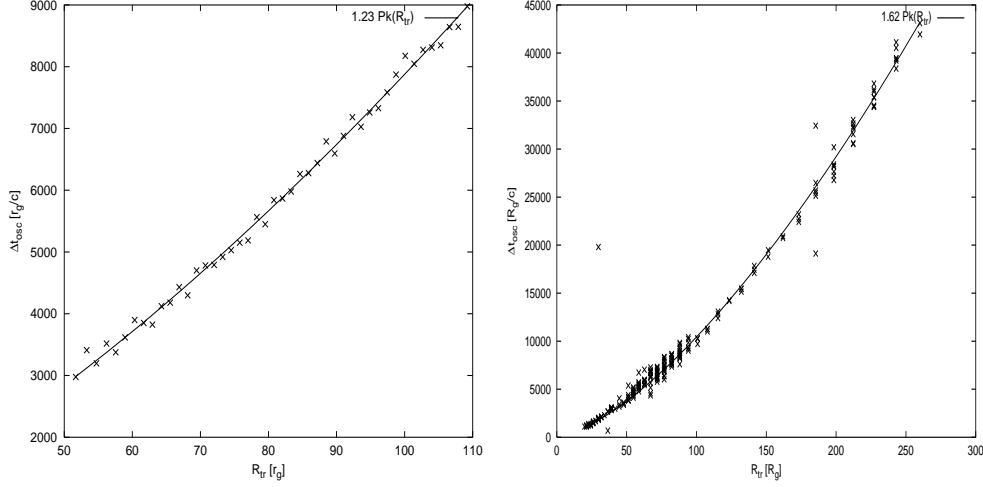
66

Figure 6.4: Dependence of the time interval between oscillation events Δt_{osc} on the transition radius R_{tr}. The left panel shows the result of a specific model with parameters $(\dot{m}, \alpha, \alpha_t/\alpha, \gamma) = (0.023, 0.4, 1, 1.5)$. For the right panel the data of all models has been combined into one large pool.

flow parameters change slowly on the viscous timescale. The numerical simulations show the contrary. Rapid variations on the local dynamical timescale (comparable to the orbital revolution time P_K^{tr}) of the flow variables in the transition region are observed. The transition region is highly unstable and the transition radius R_{tr} oscillates rapidly around its equilibrium value (this is best seen on figure 6.1). Due to this behavior we call this the *oscillation phase*.

These oscillations in the transition region seem to have their origin in instabilities arising in the transition region. Close examination of the data reveals that the instabilities are also present during the relaxation phase, though they are difficult to perceive in the images due to the low contrast and the inappropriate scaling of the time axis. It has been long known that instabilities, both stable and unstable, are present in cold standard disks (see Nowak and Lehr, 1998; Wagoner, 1999, for reviews on this topic).

Matter inflow rate $\dot{m}$ from the SSD to ADAF is not continuous but modulated with the same pattern as the oscillations. It seems that blobs of cold matter periodically invade the ADAF from the transition region. During this injection the transition region as defined by $l > l_K$ reaches far into the ADAF.

Apart from this rapid oscillations, the location of the transition radius also drifts outward slowly. The SSD shrinks in radial size, while the ADAF grows. In the present model the transition radius moves from initially $R_{tr}(0) = 54\,R_g$ to $R_{tr}(0.42\,P_K) = 123\,R_g$. The radial outward drift velocity decreases with increasing R_{tr} or increasing time. That is, the transition moves slower outward at late times. This behavior is perceived in all models and is the most enigmatic feature.

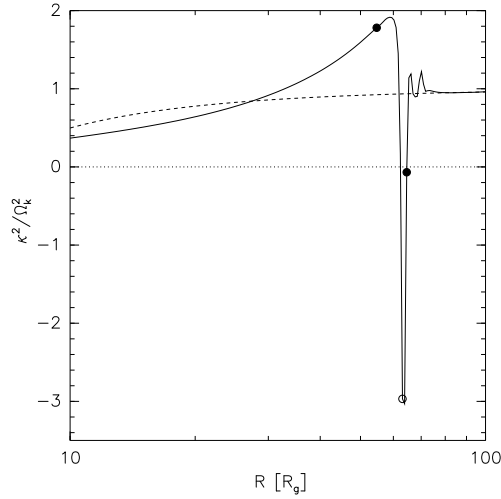This particular model ceased to converge at $t = 0.42\,P_K$, where the time-step

Figure 6.5: Epicyclic frequency in the transition region as a function of radius R. The solid line represents the square of the epicyclic frequency κ^2 in units of the keplerian angular velocity Ω_K^2 as calculated from one of our models. The dashed line corresponds to a flow with pure keplerian rotation $\Omega = \Omega_K$. The inner and outer limits of the transition region are marked with filled circles, while the location of the transition radius is indicated by the open circle.

dropped drastically from $\Delta t \approx \Delta t^{CFL}$ to $\Delta t = 0$ and the code threw a numerical exception. In the parameter range which has been studied, we did not find any model which converged for all times. We argue that this is not a numerical problem but rather a breakdown of the physical model, i.e. at some point there is no physical solution to the system of equations (or physical model) and the parameters $(\dot{m}, \alpha, \alpha_t, \mathrm{R_{tr}})$ we – or in the case of $\mathrm{R_{tr}}$ the flow itself – chose. This is an important issue and will be discussed while reexamining the location of the transition radius in section 6.3.

6.2   Oscillations in the transition region

Our numerical models show rapid variations of the transition radius $\mathrm{R_{tr}}$ as shown in figure 6.1. They look very regular and their period increases with increasing transition radius. To analyze this behavior quantitatively we identified the minimum and maximum transition radius during an oscillation event as indicated in figure 6.1 by the crosses and stars, respectively. The outer radius was treated as the generic or true location of the transition and fitted by an analytical function yielding $\mathrm{R_{tr}}(t)$, while the inner one as a perturbation due to the oscillation event. Next we calculated the time interval between two oscillations Δt_{osc} as marked by the position of the minimal transition radii.

Figure 6.4 shows the dependence of Δt_{osc} on the assumed true transition radius $\mathrm{R_{tr}}(t)$. The period between oscillation events coincides very well with the local
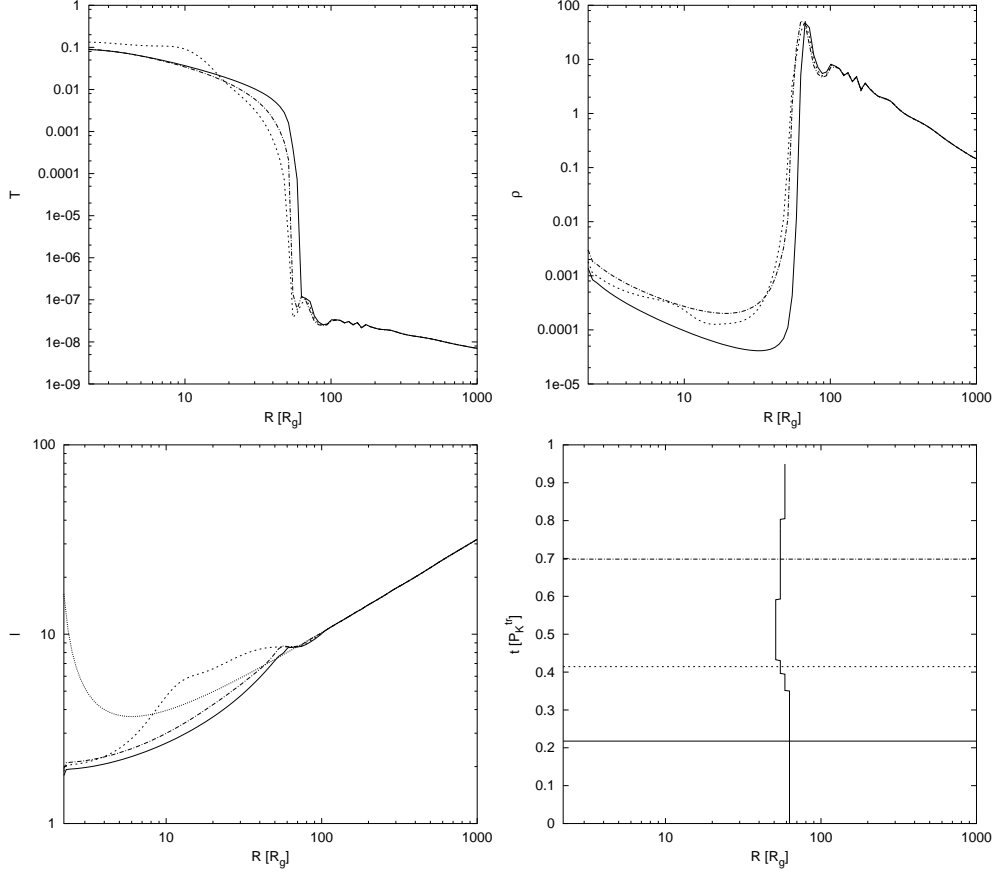
Figure 6.6: Snapshots during an oscillation event. The lower right panel indicates the location of transition radius in the $R - t$ plane. The horizontal lines indicate the time of the snapshots for the other three panels. The first snapshot (*solid*) is taken before the oscillation event; the second (*dashed*) during the oscillation roughly at the time of the reflection at the sonic point; the third snapshot (*dot-dashed*) is taken while the flow relaxes into its unperturbed configuration. The remaining panel show temperature T (upper left), density ρ (upper right) and specific angular momentum and the keplerian value (lower left).

Keplerian orbital revolution time $P_K^{tr}(\mathrm{R_{tr}}(t))$ times a numerical factor a of the order of $\mathcal{O}(1)$. The numerical factor is $a = 1.23 \pm 0.03$ [2] and does not depend systematically on the initial transition radius $\mathrm{R_{tr}}(0)$, nor the model parameters $(\dot{m}, \alpha_t, \alpha)$. To demonstrate this, we collect the data from all our models into one pool and recover the same relation as shown in the right panel of figure 6.4. It is immediately evident that one function fits all models simultaneously. The slight difference of the numerical factor has purely technical reasons. We cannot calculate a common analytical fit to the true transition radius for all models and thus plotted Δt_{osc} against the last known maximum transition radius (the

[2]The given error is the statistical scatter between different models.
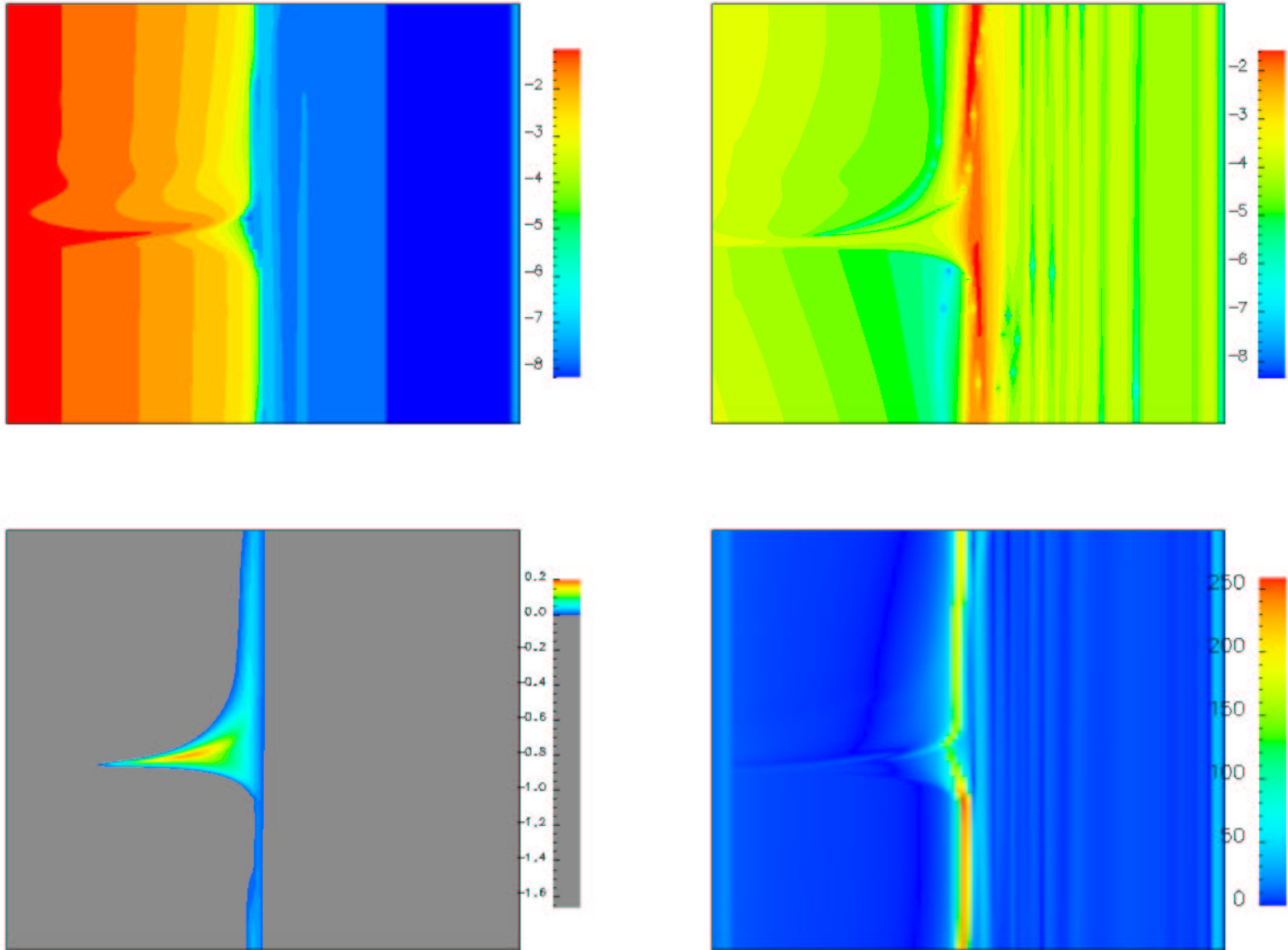
Figure 6.7: Dynamics of the oscillations in the ADAF-SSD transition region. On each panel radius $R = (2R_g \cdots 2000R_g)$ increases from left to right on a logarithmic scale, while time $t = (0 \cdots 0.92\, P_K^{tr}(62))$ runs from bottom to top on a linear scale. The individual panels show logarithm of temperature $\log T$ (upper left), logarithm of vertically integrated radial momentum density $\log p_R$ (upper right), specific angular momentum l/l_K in units of the keplerian value l_k in the zone of super-keplerian rotation, ie. the transition zone (lower left) and the total pressure gradient $\partial_R P_R$ in arbitrary units (lower right).

one marked by the stars $\times$ in figure 6.1).

The only parameter which seems to have a small influence on the proportionality factor a is the local numerical resolution, i.e. the spacing between adjacent grid nodes. We find higher values of $a = 1.35$ for lower numerical resolution, but the effect is only about 10% while the resolution is 50% worse.

Nonetheless we believe that these oscillations are not due to numerical instabilities, but rather due to physical instabilities in the transition region which do *not* depend on the global properties of the flow as a whole, e.g. $(\dot{m}, \alpha, \alpha_t, \gamma)$.

Let us assume that some physical quantity in the transition region is perturbed and obeys the wave equation, such that the amplitude of the perturbation will be proportional to $\exp(-\imath\omega t)$. In a rotating medium the wave frequency ω is bounded by the epicyclic frequency κ defined by

$$\kappa^2 = 2\Omega \left(2\Omega + R\frac{\partial\Omega}{\partial R}\right) \tag{6.1}$$

such that the perturbation will preferably grow or decay with $\omega^2 \approx \kappa_{max}^2$, where κ_{max} is the local extreme of κ. As Kato and Manmoto (2000) and Kato (2001) showed, whenever the specific angular momentum l decreases outward (like in the transition region), the flow is in principal subject to Rayleigh instabilities. Whether these instabilities develop a catastrophic growing mode or merely an oscillating, depends on the strength of the restoring and displacing forces, i.e. pressure and centrifugal force. This manifests itself in the epicyclic frequency. If $\kappa^2 < 0$ is negative the flow is locally and dynamically unstable such that the perturbation will grow and eventually develop a full scale instability. If $\kappa^2 > 0$ is positive however, the perturbation will merely oscillate with a frequency given by ω^2 near κ_{max}^2. Kato and Manmoto (2000) also showed that the perturbation, whether oscillating or growing, will be trapped within the transition region because ω will be less than the epicyclic frequency outside of the transition region and thus the perturbations do not propagate.

Figure 6.5 shows the situation in a typical model during the relaxation phase. In the outer parts of the transition region κ^2 has a negative maximum, i.e. a growing mode, which is only present in the relaxation phase and vanishes in the oscillation phase.[3] Simultaneously κ^2 has a positive maximum in the inner part of the transition region, such that the development of an oscillation is expected. From the figure we see that the oscillation frequency has an upper limit given by $\omega_{max}^2/\Omega_K^2 \approx 2$ which means that the oscillation period a has a lower limit given by $a_{min} = 1/\sqrt{2} = 0.70$. This is right order of magnitude and surprisingly close to the value $a = 1.23$ we found in our models.

We mentioned earlier that the perturbations in the transition region are supposed to be effectively trapped within the same. As usually, this simple picture

---

[3]These growing modes detach as perturbations from the transition region and move radially outward through the SSD and decay thereby slowly. This is most evident in the radial momentum plot (lower right) of figure 6.2, where 4-5 perturbations are seen as brighter orange regions.

does not survive the confrontation with numerical experiments entirely unharmed. The perturbation of the flow in the transition region back-reacts with the flow. Figure 6.7 illustrates the dynamical evolution of the flow during an oscillation event at high resolution in time, while figure 6.6 shows snapshots at three different points in time.

The oscillation event is initiated by a perturbation in velocity field and pressure gradient (as seen in the upper and lower right panel of figure 6.7 respectively) hitting the inner boundary of the transition region as defined by $l > l_K$. The perturbation leaks into the ADAF part while a blob of cold matter detaches from the transition region and invades the ADAF. In this way the ADAF is periodically refilled with matter. The ejected blob carries nearly constant angular momentum, such that the region of super-Keplerian rotation $l(R)/l_K(R) \approx l(\mathrm{R_{tr}})/l_K(R) > 1$ reaches far into the ADAF. The cold blob initially mixes with the hot ADAF plasma and the temperature profile is broadened near the transition region. When the perturbation reaches the sonic radius, it is reflected as an outgoing acoustic wave with higher temperature. In continuation the ADAF relaxes slowly back into its unperturbed state while the perturbation is advected radially. Hence the evolution of our models is strongly affected by the existence of oscillation in the transition region.

6.3   Location of the transition radius revisited

One of the main results of Manmoto and Kato (2000) was that the transition from an inner ADAF to an outer SSD is not allowed to happen at all radii. Rather the transition radius $\mathrm{R_{tr}}$ is limited to certain range of allowed locations. The range of the allowed transition radii is a function of the accretion rate $\dot{m}$, the fraction α_T/α and the viscosity paramater α.[4] The mass of the central black hole M and the ratio of specific heats γ might also have an influence, but this has not been studied systematically, neither by Manmoto and Kato (2000) nor in this work.

Formally, ADAF-SSD transition models live in a 4-dimensional parameter space $(\mathrm{R_{tr}}, \dot{m}, \alpha_t/\alpha, \alpha)$. Following Manmoto and Kato (2000) we use the generic values $(\dot{m}, \alpha_t/\alpha, \alpha) = (0.01, 1, 0.4)$ unless otherwise noted. Manmoto did only study steady ADAF-SSD models, while this work treats fully time-dependent models. In this sense our parameter space is 5-dimensional. But we rather interpret this as an evolution in time of our models within the 4-dimensional parameter space $(\mathrm{R_{tr}}, \dot{m}, \alpha_t/\alpha, \alpha)$. All models have $M = 10\,\mathrm{M_\odot}$ and $\gamma = 1.4$ in common. The rest of the model parameters of the calculated models are summarized in the following table.

---

[4]See chapter 5.4 for a discussion of these dependencies.
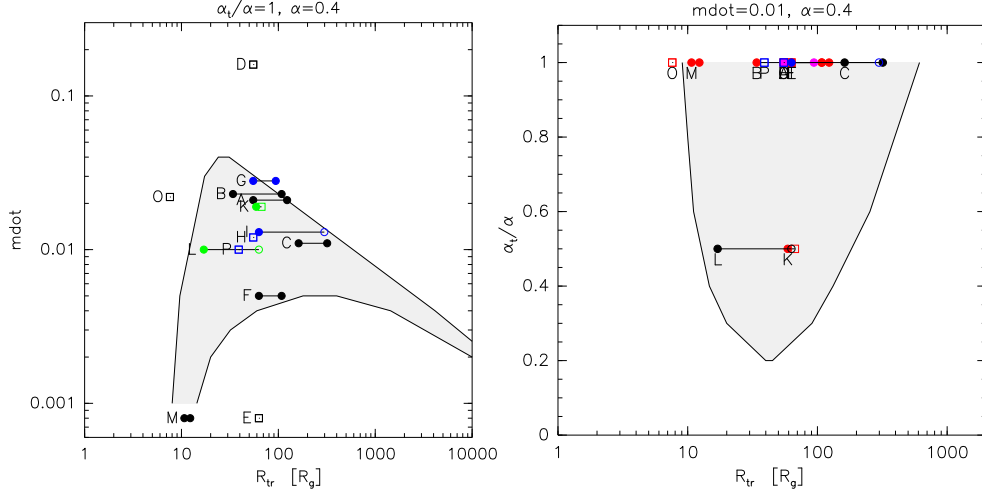
Figure 6.8: Evolution tracks of time-dependent ADAF-SSD transition models in the $(R_{tr}, \dot{m})$-plane (left panel) and the $(R_{tr}, \alpha_t/\alpha)$-plane (left panel). The shaded area indicates the allowed transition radii according to Manmoto and Kato (2000). All models evolve from left to right along the solid lines. The initial and final transition radii are marked by various symbols as described in the text. The color indicates that the model parameters deviate from the values given at the top, i.e. $\dot{m}$ (red), α_t (green), α (blue) or various (magenta). The individual models are identified with an uppercase letter next to the initial transition radius. (See text for detailed discussion.)

model	$(\dot{m}, \alpha_T/\alpha, \alpha)$	$R_{tr}{}^i[R_g]$	$R_{tr}{}^f[R_g]$	remarks
A	$(0.021, 1, 0.4)$	55	123	reaches $R_{tr}{}^{max}$
B	$(0.023, 1, 0.4)$	34	108	reaches $R_{tr}{}^{max}$
C	$(0.011, 1, 0.4)$	162	319	reaches $R_{tr}{}^{max}$
D	$(0.16, 1, 0.4)$	55		no transition
E	$(0.0008, 1, 0.4)$	63		no transition
F	$(0.005, 1, 0.4)$	63	108	reaches $R_{tr}{}^{max}$
M	$(0.0008, 1, 0.4)$	10.7	12.3	reaches $R_{tr}{}^{max}$
O	$(0.022, 1, 0.4)$	6.3		no transition
G	$(0.028, 1, 0.1)$	55	94	reaches $R_{tr}{}^{max}$
H	$(0.012, 1, 0.25)$	55		no transition
I	$(0.013, 1, 0.8)$	63	298	could run further
P	$(0.01, 1, 0.3)$	39		no transition
K	$(0.019, 0.5, 0.4)$	59	67	ceases to converge
L	$(0.01, 0.5, 0.4)$	17	55	could run further
J	$(0.0075, 0, 0.4)$	59	115	no turbulance, could run further
N	$(0.028, 0, 0.1)$	51	94	no turbulance, could run further

This 4-dimensional parameter space is visualized by 2-dimesional cuts. Manmoto and Kato (2000) explicitly showed cuts in the $(R_{tr}, \dot{m})$ and $(R_{tr}, \alpha_T/\alpha)$-planes at $(\alpha_T, \alpha) = (1, 0.4)$ and $(\dot{m}, \alpha) = (0.01, 0.4)$, respectively. We do likewise in figure 6.8. Due
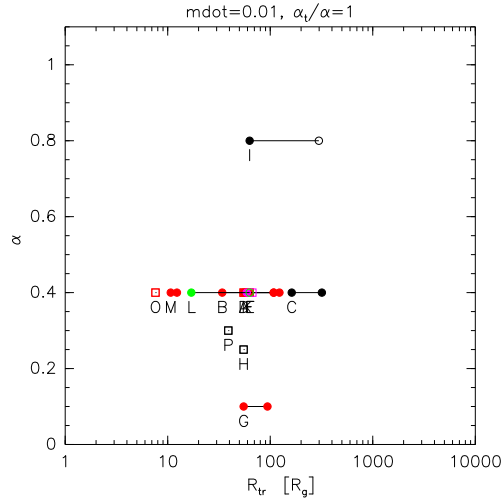
Figure 6.9: Evolution tracks of time-dependent ADAF-SSD transition models in the (R_{tr}, α)-plane. All models evolve from left to right along the solid lines. See caption of figure 6.8 for a key to the symbols and colors. (See text for detailed discussion.)

to the limited number of models available we show *projections* onto the respective plane, rather than cuts along the plane. Models which lie exactly on or near the respective plane are indicated by their black color. Models which lie outside of the plane are projected onto the plane and indicated in red or blue color.

Our models start with the transition radius initially located at $R_{tr}{}^i$. As our models enter the relaxation phase they will undergo one of three possible evolutions.

(1) the model never leaves the relaxation phase, either because it does not converge at all, or it does so only at unacceptable low time-steps $\Delta t \approx 0$. This is interpreted such that there is no transition allowed at or near $R_{tr}{}^i$. We mark these models with an open square at $R_{tr}{}^i$.

(2) The model eventually leaves the relaxation phase and enters the oscillation phase. These models are indicated with a filled circle at $R_{tr}{}^i$. The transition radius evolves in time and moves generally outward. We have found no example, where the transition radius moves inward for sustained period of time. The calculations are either artificially stopped at a final transitions radius $R_{tr}{}^f$ or reach a final transition radius $R_{tr}{}^f$, where the time-step again decreased dramatically, by themselves. In the former case the model could very well evolve to larger transiton radii, such that $R_{tr}{}^f$ is only a lower boundary (this is marked by an open circle at $R_{tr}{}^f$). While the latter case is interpreted as the transition having reached its outermost allowed location $R_{tr}{}^{max}$. At this point our physical model is assumed to break down in the sense, that no solution of the adopted system of equations with the parameter $R_{tr} > R_{tr}{}^{max}$ is available. This
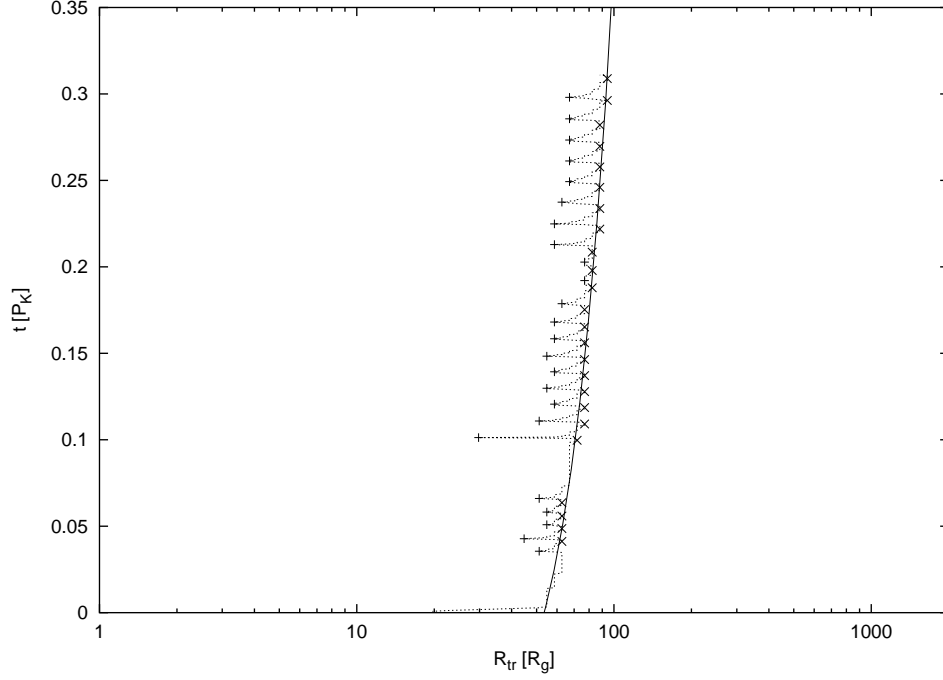
74

Figure 6.10: Location of the transition radius R_{tr} of model G (*dotted*) in time. The crosses + and stars × mark the innermost and outermost position of the transition. The latter is fitted by an analytical function (*solid*).

is indicated by a filled circle at $R_{tr}{}^f = R_{tr}{}^{max}$.

(3) either something peculiar happens during the oscillation phase, such that the model is deliberately not calculated further, or the code throws a numerical exception at some point. These models are indicated with a filled circle at $R_{tr}{}^i$ and an open square at $R_{tr}{}^f$.

Our models A through F, M and O lie exactly in the $(R_{tr}, \dot{m})$-plane shown in the left panel of figure 6.8. Thereof models D,E and O do not converge at all and we conclude, that no ADAF-SSD models are possible for these parameters. This is in agreement with Manmoto's allowed region. Models A,B,C,F and M reach their outermost transition radius. For A, B and M this is in perfect agreement with Manmoto. C and F deviate slightly, though if one takes into account, that $\dot{m}$ is also a function of time, this can be brought into accordance. Model M is some regard peculiar. This is the only model which reaches its outermost transition radius during the relaxation phase before the oscillations in the transition region proper start to leak into the ADAF. The range of allowed transition radii is simply so narrow, that our model evolves beyond that region within a few keplerian revolution times P_K^{tr} before oscillations have any chance to grow considerably. The remaining models are located outside of the considered plane as indicated by their color.

The $(R_{tr}, \alpha_t/\alpha)$-plane is very sparsely populated by our models (see right panel of figure 6.8. Only L has $\dot{m} = 0.01$ exactly. Therefore we plot those models,

which have approximately (within a factor of 1.5) the desired accretion rate, in black also. We did further only calculate models with either $\alpha_t/\alpha = 1$ or $\alpha_t/\alpha = 0.5$. Non withstanding we did not find any ADAF-SSD transition model which projects outside of the steady allowed region. On the other hand model K converges only at low time-steps Δt and slowly drops below our lower limit ($\Delta t = 10^{-3}\,\Delta t_{CFL}$) without any apparent reason and far away from any boundary of the allowed region. All other models can be accounted for, although none of them really defines an upper boundary to the transition radius in this particular plane.

Manmoto and Kato (2000) did not discuss any dependency of the possible locations of the transition radius on the viscosity parameter α and did only present models with the generic value $\alpha = 0.4$. Our results are illustrated in figure 6.9, which shows the $(\mathrm{R_{tr}}, \alpha)$-plane at $(\dot{m} \approx 0.01, \alpha_t/\alpha = 1)$. The situation here seems to be much more complicated. On one hand the range of allowed transition radii is very broad at $\alpha = 0.8$ and extends to at least as large radii as at $\alpha = 0.4$ (see models I and C respectivelly). On the other hand we do not find any transitions at $\alpha \approx 0.25$ (models P and H), while at even lower values, $\alpha = 0.1$ we do find again a transition in model G. Our model G is off-plane because of $\dot{m} = 0.028$, but this only worsens the situation, because the allowed region tends to broaden with decreasing $\dot{m}$ (at least at $\alpha = 0.4$). There seems to be a forbidden region, or at least a hole, between $\alpha = 0.4$ and $\alpha = 0.1$.

We find more indications for holes in the allowed region. Figure 6.10 shows the location of the transition radius of model G as a function of time. Again we find a slow radial outward drift and superimposed oscillations. But the oscillations are missing between $0.07\,P_K \leq t \leq 0.1\,P_K$ and to lesser extent at $t \approx 0.2\,P_K$. There the flow behaves much more like during the relaxation phase. This could be interpreted such that no transition is allowed at the respective locations, i.e, $R \approx 63\,\mathrm{R_g} \cdots 72\,\mathrm{R_g}$ and $R \approx 82\,\mathrm{R_g}$. We do not observe such behaviour for models with large α.

Chapter 7

Implications for the Spectral Properties

We have so far only briefly mentioned the properties of the radiation field in ADAF-SSD transitions. For the purpose of hydrodynamical simulations we are only interested in frequency integrated total cooling rates which enter the energy equation. We assume that it is sufficient to work with the appropriate frequency integrated opacities, namely the Rosseland mean κ_R and the Planck mean κ_P. This is a fair assumption since the temperature of the systems we are interested in is so high, that the plasma is fully ionized and effective cooling through individual spectral lines seems very unlikely.

Nonetheless the only possibility to test theoretical models is to compare them to observations. In order to do so we need to translate the hydrodynamical models into some appropriate spectral map of the source. This might be an image in a certain spectral filter if the source can be resolved observationally, or otherwise, as in this case, a spatially integrated total spectrum.

The outline of the chapter is as follows. We first present a recipe to calculate simple spectra from our hydrodynamical models and discuss limits of this procedure. In the second part we apply this to our models and study some aspects of the spectral properties of ADAF-SSD transitions.

7.1 Calculation of spectra

Following Narayan and Yi (1995b) and Manmoto et al. (1997) we consider three processes: bremsstrahlung, synchrotron radiation and Comptonization of soft photons. In order to obtain the spectrum generated by the accretion flow, we need to solve the global radiation transfer problem in the radial and in the vertical direction. We treat such complicated problems in a rather simplified way: (1) we assume a locally plane-parallel configuration at each radius, and (2) we separated the Compton scattering process from the rest of the radiation processes, ie., emission and absorption.

We first estimate the spectrum of the unscattered photons at a given radius by solving radiative diffusion equation in that direction. For the isothermal plane-parallel gas atmosphere the density is given by (eg. Frank et al., 1985)

$$\rho(z) = \rho(0) \exp\left(-\frac{z^2}{2H^2}\right). \tag{7.1}$$

Assuming the Eddington approximation, which is valid for isotropic radiation fields (and even for slightly non-isotropic, (see Rybicky and Lightman, 1979, ch. 1.8), the radiation field in the vertical direction is described by the radiative diffusion equation (Rybicky and Lightman, 1979, eq 1.121):

$$\frac{1}{3}\frac{\partial^2 J_\nu}{\partial \tau_\nu^2} = J_\nu + B_\nu, \tag{7.2}$$

where B_ν and J_ν are the source function for thermal emission and scattering, respectively. and τ_ν the optical depth from the surface of the accretion flow. There is no well defined surface of the accretion flow, since the density tends to zero with increasing z without ever being equal to zero. However, the optical depth τ_ν in the vertical direction is finite, and hence can be used the define the surface of the accretion flow. Note that $\tau_\nu = 0$ at the surface, $\tau_\nu = \tau_\nu^* = (\pi^{1/2}/2)\,\kappa_\nu(0)\,H$ at the equatorial plane and $\tau_\nu = 2\tau_\nu^*$ at the other surface.

The diffusion equation (7.2) can be solved with appropriate boundary conditions. We take

$$\frac{1}{\sqrt{3}}\frac{\partial J_\nu}{\partial \tau_\nu} = J_\nu \qquad (\tau_\nu = 0), \tag{7.3}$$

$$\frac{\partial J_\nu}{\partial \tau_\nu} = 0 \qquad (\tau_\nu = \tau_\nu^*). \tag{7.4}$$

The boundary condition at the surface assumes that there is no irradiation onto the surface of the accretion flow, while at the equatorial plane outward and inward radiative flux cancel each other. According to Manmoto et al. (1997), the solution of equation 7.2 with these boundary conditions is

$$J_\nu = B_\nu \left[1 - \frac{e^{-\sqrt{3}\tau_\nu}}{2}\left(e^{-2\sqrt{3}(\tau_\nu^* - \tau_\nu)} + 1\right)\right]. \tag{7.5}$$

The energy flux F_ν on the surface of the accretion flow is given by

$$F_\nu(0) = \frac{4\pi}{3}\frac{\partial J_\nu}{\partial \tau_\nu}\bigg|_{\tau_\nu=0} = \frac{2\pi}{\sqrt{3}}B_\nu\left[1 - \exp(-2\sqrt{3}\tau_\nu^*)\right]. \tag{7.6}$$

With the last equation the problem of vertical radiative transfer is essentially solved at each radius R. The total spectral luminosity is obtained by integrating over the surface of the disk. We did only consider the face-on case $\sin i = 1$ and thus

$$F_\nu = 4\pi \int_{disk} F_\nu(R)\,\mathrm{d}R. \tag{7.7}$$

So far our recipe to calculate spectra had to go without meat, the absorption co-
efficient κ_ν at the equatorial plane, which enters into the vertical optical depth
through $\tau_\nu^* \equiv (\pi^{1/2}/2)\,\kappa_\nu(0)H$. Assuming local thermodynamical equilibrium
(LTE), we can write $\kappa_\nu = \chi_\nu/(4\pi\,B_\nu)$, where $\chi_\nu = \chi_\nu^{brems} + \chi_\nu^{synch}$ is the emis-
sivity due to the bremsstrahlung and synchrotron radiation processes. These
are, among others, function of the electron temperature T_e.

Our models use a one-temperature description, where it is assumed, that energy
transfer between electrons and ions is efficient, such that $T_e = T_i = T$. In
contrast hereto, two-temperature models drop this strict assumption and allow
inefficient energy transfer between electron and ions, such that in general $T_e \neq$
T_i. Narayan and Yi (1995b) showed that the electron temperature deviates
from the proton temperature significantly only in the innermost region of an
ADAF, where the electron temperature saturates at about $T_e^{max} \approx 5 \times 10^9\,\mathrm{K}$
(Esin et al., 1997). The maximal electron temperature depends on the accretion
rate and the cooling model. It slightly increases with decreasing accretion rate
$\dot{m}$. Though Esin et al. (1997) gave no explicit dependency the approximation

$$T_e^{max} = 5 \times 10^9 \left(\frac{0.01}{\dot{m}}\right)^{1/2}\,\mathrm{K} \tag{7.8}$$

is a good estimate. We do not know of any reasonable procedure to otherwise
deduce the electron temperature T_e from the total temperature T a posteriori
and thus either use $T_e = T$ or use equation (7.8). On the other hand, at least for
the moment being, we only want to make a qualitative estimate of the spectral
properties of our models and not a thorough quantitative analysis – for which
our method would not be accurate enough anyway.

7.1.1 Bremsstrahlung emission

Narayan and Yi (1995b) argue that in the innermost hot region of ADAFs the
electron temperature is so high that electron-electron bremsstrahlung may dom-
inate electron-ion bremsstrahlung. Therefore the cooling rate due to brems-
strahlung emission q_{br}^- is written as

$$q_{br}^- = q_{ei}^- + q_{ee}^-. \tag{7.9}$$

We adopt the analytical expression given in (Stepney and Guilbert, 1983) and
use

$$q_{ei}^- = 1.25 n_e^2 \sigma_T c \alpha_f m_e c^2 F_{ei}(\Theta_e), \tag{7.10}$$

where n_e is the electron number density, α_f the fine structure constant, m_e
the electron mass, and σ_T the Thomson-scattering cross-section. The function
$F_{ei}(\Theta_e)$ is approximated by

$$
\begin{aligned}
F_{ei}(\Theta_e) &= 4\left(\frac{2\Theta_e}{\pi^3}\right)^{1/2}(1 + 1.781\,\Theta_e^{1.34}), & \Theta_e < 1 \\
&= \frac{9\Theta_e}{2\pi}[\ln(1.123\Theta_e + 0.48) + 1.5], & \Theta_e > 1,
\end{aligned}
\tag{7.11}
$$

where $\Theta_e = k_B T_e/(m_e c^2)$ is the electron temperature over the electron rest-mass energy. The electron-electron bremsstrahlung is calculated according to (Svensson, 1982), ie.

$$
\begin{aligned}
q_{ee}^- &= n_e^2 c r_e^2 \alpha_f c^2 \frac{20}{9\pi^{1/2}} (44 - 3\pi^2) \Theta_e^{3/2} \\
&\quad \times (1 + 1.1\Theta_e + \Theta_e^2 - 1.25\Theta_e^{5/2}), \qquad \Theta_e < 1 \qquad (7.12) \\
q_{ee}^- &= n_e^2 c r_e^2 \alpha_f c^2 24 \Theta_e (\ln 1.123\Theta_e + 1.28), \qquad \Theta_e > 1.
\end{aligned}
$$

With this cooling rate, we can write the emissivity χ_ν^{brems} as

$$
\chi_\nu^{brems} = q_{br}^- \bar{G} \exp\left(\frac{h\nu}{k_B T_e}\right), \qquad (7.13)
$$

where $\bar{G}$ is the Gaunt factor, which is given by (see Rybicky and Lightman, 1979)

$$
\begin{aligned}
\bar{G} &= \frac{h}{k_B T_e} \left(\frac{3}{\pi} \frac{k_B T_e}{h\nu}\right), \qquad \frac{k_B T_e}{h\nu} < 1 \\
\bar{G} &= \frac{h}{k_B T_e} \frac{\sqrt{3}}{\pi} \ln\left(\frac{4}{\zeta} \frac{k_B T_e}{h\nu}\right), \qquad \frac{k_B T_e}{h\nu} > 1,
\end{aligned}
\qquad (7.14)
$$

where ζ is a constant of the order of unity.

7.1.2 Synchrotron radiation

In the presence of magnetic field, charged particles will be accelerated along the field lines and loose energy due to synchrotron radiation. Our models do not include the evolution of any large scale magnetic fields. Small scale chaotic magnetic field could nonetheless make themselves felt through additional magnetic pressure without influencing the dynamical behavior otherwise. It is thus assumed that the magnetic field is in the order of the equipartition magnetic field. The magnetic pressure p_{mag} is then written as

$$
p_{mag} = \frac{(1-\beta)}{\beta} p_{gas} = \frac{B^2}{8\pi}, \qquad (7.15)
$$

where $\beta = p_{gas}/p$ is the fraction of gas pressure to total pressure. We set $\beta = 1/2$, ie. equipartition. From equation (7.15) we calculate the magnetic field strength B, which goes into the following expressions.

The optically thin synchrotron emissivity by a relativistic Maxwellian distribution of electrons was first considered in Pacholczyk (1970) and later improved upon by Narayan and Yi (1995b) who give the following analytical expression

$$
\chi_\nu^{synch} = 4.43 \times 10^{-30} \frac{4\pi n_e \nu}{K_2(1/\Theta_e)} I'\left(\frac{4\pi m_e c\nu}{3eB\Theta_e^2}\right) \qquad (7.16)
$$

where K_2 is a modified Bessel function and $I'(x)$ given by

$$
I'(x) = \frac{4.0505}{x^{1/6}} \left(1 + \frac{0.4}{x^{1/4}} + \frac{0.5316}{x^{1/2}}\right) \exp(-1.8899 x^{1/3}). \qquad (7.17)
$$

Although these formulae are only valid in for relativistic temperatures $\Theta_e > 1$, we use them at all temperatures. In our model the synchrotron emission always comes from the relativistic electrons in the tail of the Maxwell distribution, so this approximation is reasonable.

7.1.3 Comptonization

Comptonization is in general a very delicate problem as it is a intrinsically non-local process. Photons which where generated at some point in space travel for a fraction of the mean-free-path length and then are scattered off free electrons. Part of the energy of the electron may be transfered to the incident photon (Compton effect) or vice-versa (inverse-Compton effect).

We make use of the idea of the energy enhancement factor, which was derived by Dermer et al. (1991) and modified in part by Esin et al. (1996). The energy enhancement factor η is defined as the average energy boost of a photon, if the incident photon energy was $h\nu_i$ the outgoing photon will carry the energy $h\nu_o = \eta \, h\nu_i$. The prescription for η is

$$\eta = \exp(s(A-1))\left[1 - P(j_m + 1, As)\right] + \eta_{max}P(j_m + 1, s), \qquad (7.18)$$

where $P(a, x)$ is the incomplete gamma function, and

$$A = 1 + 4\Theta_e + 16\Theta_e^2, \qquad s = \tau_{es} + \tau_{es}^2 \qquad (7.19)$$

$$\eta_{max} = \frac{3k_B T_e}{h\nu}, \qquad j_m = \frac{\ln \eta_{max}}{\ln A}. \qquad (7.20)$$

A is the average increase of energy in each scattering by a Maxwellian distribution of electrons of temperature Θ_e, $\tau_{es} = 2n_e\sigma_T H$ the Thomson optical depth, j_m is the number of scatterings required for the maximal energy enhancement η_{max} and ν is the incident frequency of the photon.

Since the spectrum of soft photons, ie. synchrotron photons, strongly peaks at a frequency ν_p, it is s a first approximation sufficient to calculate η at ν_p, only. The peak frequency can be estimated from $\nu_p^2 = H\chi_\nu^{synch}c^2/(2\pi k_B T_e)$ (Esin et al., 1996), or directly taken from the numerical calculations. The photons which scatter more then j_m times do saturate and obey the Wien distribution $\sim \nu^3 \exp(-h\nu/k_B T_e)$ (see also Coppi and Blandford, 1990, for a detailed treatment of multiple scattering).

Often this treatment is too simple, specially if accurate predictions of X-ray flux at energies in excess of 10keV are necessary. In this case one must also take into account, that photon do not only move vertically, but also radially. Non-local scattering processes where the photons scatter at regions with different densities and temperatures will play a role. If such processes are to be modeled accurately, it is necessary to solve the Kompaneets equation (see eg. Hujeirat et al., 2002).

7.2 Spectral Properties

We calculated spectra for our models using the simple approach described in the previous section. We have neglected the comptonization of soft photons in all calculations. The reason will be discussed later.
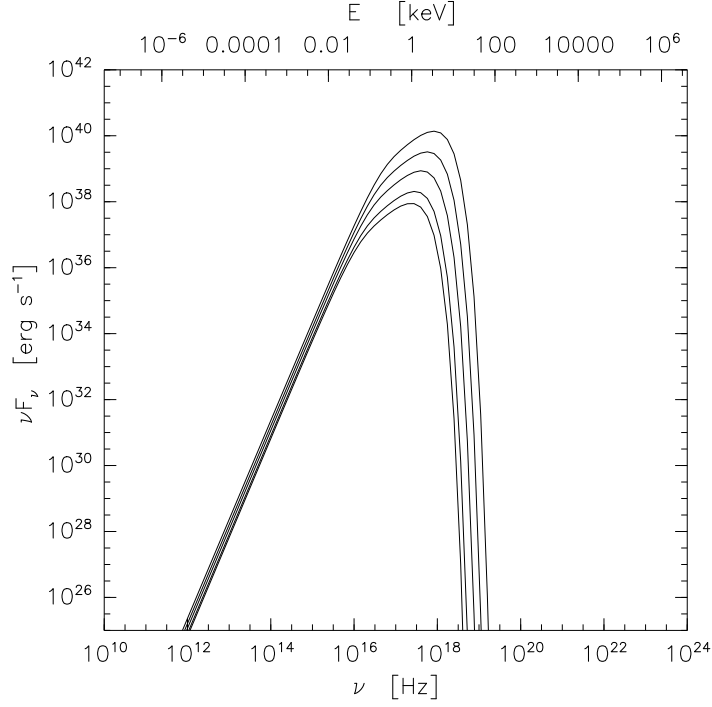
Figure 7.1: Spectrum of the standard disk for different accretion rates. The SSD extends from $R = 2 \times 10^3 \, \mathrm{R_g}$ down to the marginal stable orbit. The different lines correspond to the accretion rates $\dot{m} = (0.015, 0.03, 0.1, 0.3, 1)$ and increase from the bottom to the top line.
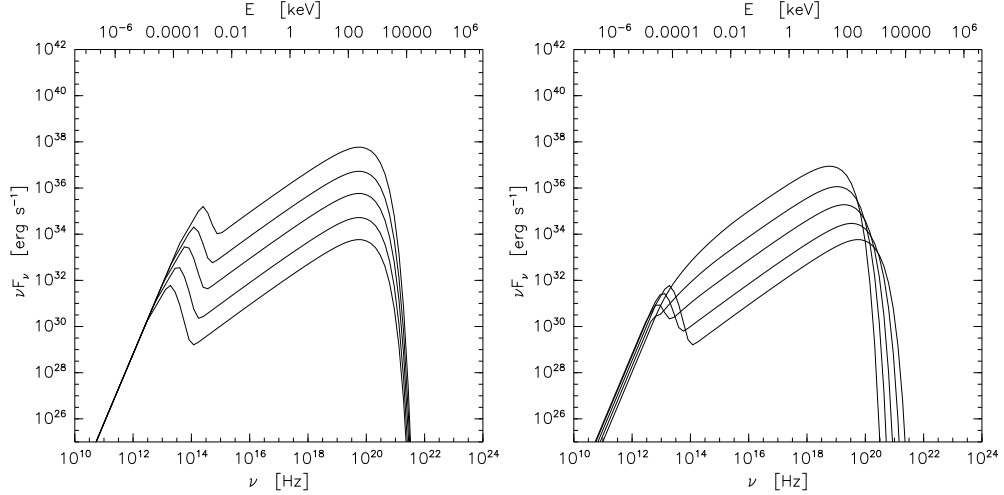

Figure 7.2: Influence of the electron temperature on the spectrum of a transonic ADAF at different accretion rates. For the left panel the electron temperature is taken to saturate at $T_e^m ax = 5 \times 10^9 \mathrm{K}$, while for the right panel T_e^{max} is given by equation (7.8). The different lines correspond to the accretion rates $\dot{m} = (0.015, 0.03, 0.1, 0.3, 1)$ and increase from the bottom to the top line.
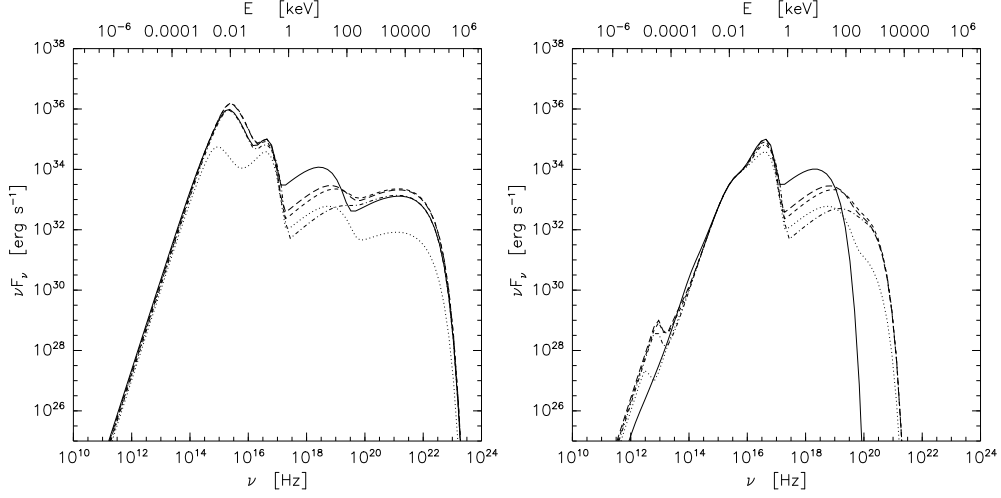
Figure 7.3: Spectra of ADAF-SSD transition models at different transition radii. The transition is located at $R_{tr} = 58R_g$ (*dotted*), $R_{tr} = 73R_g$ (*dot-dashed*), $R_{tr} = 83R_g$ (*short-dashed*), $R_{tr} = 93R_g$ (*long-dashed*) and $R_{tr} = 108R_g$ (*solid*), respectively. The left panel shows the spectra if the electron temperature is taken to be the proton temperature, i.e $T_e = T$. The right panel shows the spectra if T_e is limited by T_e^{max}, as described in the text.
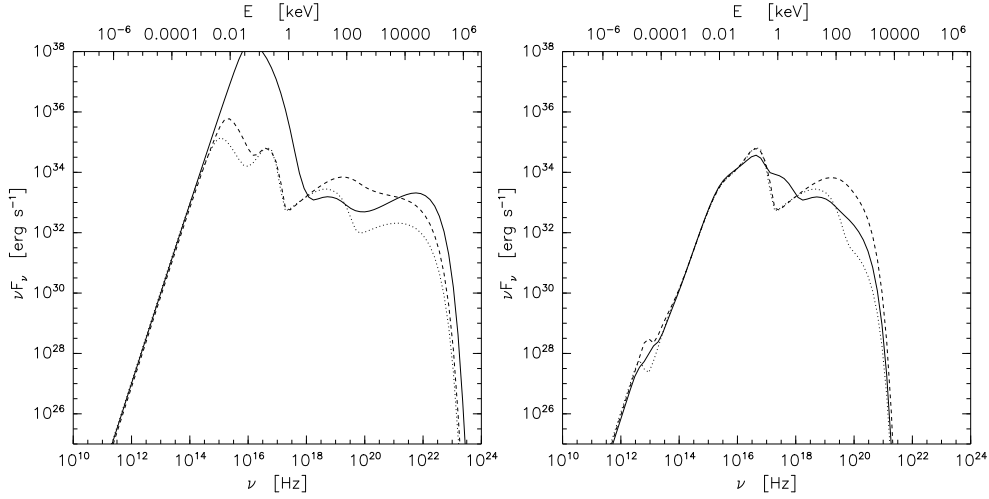

Figure 7.4: Influence of the oscillation event on the spectrum of ADAF-SSD transition models. The lines correspond to three points in time immediately before the oscillation event(*dotted*), during the relaxation back into the unperturbed state (*dashed*) and at the hight of the oscillation, respectively. These are the same points in time as in figure 6.6. The left panel shows the spectra if the electron temperature is taken to be the proton temperature, i.e $T_e = T$. The right panel shows the spectra if T_e is limited by T_e^{max}, as described in the text.

83

Figures 7.1 shows a comparison of the spectra of pure SSD models of different accretion rates $\dot{m}$. The SSD is optically thick at all radii, therefore the spectrum is a superposition of black-body emission of local temperature $T(R)$, sometimes referred to as multicolor blackbody. The SSD extends to the outer radius $R_{out} = 2 \times 10^3 \, Rg$, where the temperature is lowest. The temperature takes its maximum T_{max} near to the inner boundary. At the low-energy end $h\nu \ll kT(R_{out})$ the flux F_ν is proportional to ν^2 – the Rayleigh-Jeans law. While at high energy $h\nu \gg kT_{max}$ the flux cuts off as $\nu^3 \exp(-h\nu/kT)$ – the Wien law. The characteristic signature of the multicolor blackbody is the flat profile at intermediate frequencies. There the flux is proportional to $\nu^{1/3}$ (Frank et al., 1985). This intermediate section is more pronounced for higher fractions T_{max}/T_{out}. The local temperature $T(R)$ of a standard disk is an increasing function of accretion rate $\dot{m}$. Therefore the flux increases with the accretion rate also.

The spectrum of the ADAF consist of two components. At the low-energy end the synchrotron peak is centered around $\nu_p \sim 10^{13} \, \mathrm{Hz}$. The bremsstrahlung emission extends as a power law to its upper cut-off at $h\nu/k_b T \approx 1$. The peak frequency of the synchrotron emission shifts to lower energies with decreasing accretion rate. This is because $\nu_p \propto B$ scales with $\nu_p \propto \dot{m}^{1/2}$, by virtue of the assumption of equipartition.

The flux scales approximately as $F_\nu \propto \dot{m}^2$. It also is strongly affected by the temperature of the electrons. If the electron temperature is taken to be equal to the ion temperature, i.e. $T_e = T$, then the flux is over-estimated by at least 4 orders of magnitude. We argued that the electron temperature of the order of $5 \times 10^9 \mathrm{K}$, but depends also on the accretion rate $\dot{m}$. The peak frequency of synchrotron emission is affected by the saturation temperature of electrons. Figure 7.2 compares the the crude estimate $T_e^{max} = 5 \times 10^9 \mathrm{K}$ to the approximation given in equation (7.8). In the latter case both amplitude and peak frequency differ significantly from former case. The cut-off frequency of the bremsstrahlung emission varies strongly also. The amplitude of the flux is unaffected by electron temperature at intermediate frequencies only. But this region will in general be also populated by comptonized synchrotron photons, such that the total flux is again subject to the electron temperature. This is the reason why we did not include comptonization in our model spectra yet.

Barring the problem of the estimation of the electron temperature, our simple recipe reproduces the spectral components of ADAF and SSD quite well. Optically thick blackbody emission, bremsstrahlung emission and synchrotron radiation can be clearly separated and their depandence on the flow parameters is understood (see eg. Esin et al., 1997; Manmoto et al., 1997, for comparison). But their relative weight can only calculated accurately from 2-temperature models, where the electron temperature is allowed to differ from the ion temperature. We note, that the electron temperature increases with decreasing mass accretion rate, $\dot{m}$, such that at very low accretion rates, $\dot{m} \sim 10^{-6}$, the 1-temperature description is appropriate (Esin et al., 1996).

The spectra calculated from our ADAF-SSD transition models consist of three

components, the multicolor blackbody of the cold SSD, the synchrotron peak and the bremsstrahlung power law. Again we did not include comptonization. Figure 7.3 shows the spectrum of model B at varies transition radii, $58R_g \leq R_{tr} \leq 108R_g$. The multicolor blackbody component is merely affected, the difference of temperature at the inner edge of the SSD is simply to small ($T_{SSD}(R) \propto R^{-3/4}$). It is further obfuscated by warm gas in the transition region. The figure again compares the cases where the electron temperature is equal to the ion temperature or saturates, respectively. The difference is dramatic. While in the latter case the synchrotron emission from the ADAF is barely visible as small peak at $\nu \sim 10^{13}$ Hz, it almost exceeds the cold disk emission in the former case, such that a double peak structure emerges at $\nu \sim 10^{15}$ Hz. The same is true for the bremsstrahlung cut-off. Only at intermediate frequencies $\nu \sim 10^{18}$ Hz is the spectrum unaffected.

The last figure 7.4 illustrates the situation during an oscillation event. Especially the synchrotron emission is highly variable. Dense gas of high-pressure and thus magnetic field invades the ADAF from the transition region. In our simple analysis the electron temperature rapidly reaches its saturation value, while pressure and density are still high. This leads to a strong increase of the synchrotron emission. Whether this is visible over the cold blackbody emission depends crucially on the overall amplitude and the peak frequency, both given by the electron temperature in the transition region. Interestingly our model spectra pivote around $\nu \sim 10^18$ Hz or $h\nu \sim 10$keV such that the spectral slope is inverted, independent of the assumptions on T_e. We conclude by noting that accurate estimates of the electron temperature are crucial for the calculation of ADAF-SSD transition models.

Chapter 8

Discussion

8.1 Availability of ADAF-SSD transitions

One of the necessary connection conditions for ADAF-SSD transitions is that the total outward energy flux, W, of the ADAF is positive and larger than the corresponding energy flux of the SSD at the transition radius, i.e. ($W_{ADAF} > W_{SSD}$). Otherwise, the ADAF cannot supply the SSD with enough energy and both regions are not thermally connected. The standard ADAF model (Narayan and Yi, 1994) does not meet this requirement. The standard model was extended (Honma, 1996; Manmoto et al., 2000) to include outward convective energy transfer along the entropy gradient. This model could in principle remedy the situation, and indeed Manmoto and Kato (2000) found steady global ADAF-SSD transition models. They found that the transition is not allowed to happen at any radius, but limited to a certain range of allowed transition radii which depends on the model parameters ($\dot{m}, \alpha_T/\alpha$). They did not study the dependence on the viscosity parameter α.

This work presents a generalization of Manmoto's model for time-dependent flows. In our models the transition radius is allowed to vary as a function of time and thus the models evolve in the parameter space spawned by ($R_{\mathrm{tr}}, \dot{m}, \alpha_T/\alpha$). We found that the region of allowed transition radii of time-dependent models is consistent with steady models. One common result is that self-consistent ADAF-SSD transition models cannot exist below a certain minimal α_t/α. We do find models which technically converge for $\alpha_T = 0$, but their total outward energy flux W_{ADAF} does not exceed W_{SSD} at any radius, nor is it even positive at any radius. Also the flow switches from one grid node to the next from ADAF-like to SSD-like, without any intermediate values. This is not observed for any other model. The conclusion is that these models are not a physical solution to the problem, however a mathematical.

Our parameter study also includes variations of the viscosity parameter α. We found that the range of allowed transition radii at $\alpha = 0.8$ is at least as large as for $\alpha = 0.4$. This suggests that the allowed region broadens with increasing α. This is consistent with Honma's estimate of the outermost radius $R_{out} \propto \alpha^4 \dot{m}^{-2}$

at which convective turbulence still transfers energy outward (Honma, 1996). For intermediate values of $\alpha \approx 0.25$ we do not find ADAF-SSD transition models with $\dot{m} \approx 0.01$, as expected. Interestingly, for even lower $\alpha = 0.1$ we do again find a transition model. This model (G) is in some regard peculiar. It does not show continuous oscillations as observed in all other models, but rather seems to repeatedly re-enter what we called the relaxation-phase, during which the flow relaxes into a solution of the imposed system of equations. The radial dependence of the outward energy flux W varies strongly with time, but turbulence transfers enough energy outward to make it positive at all times. On the other hand it is less than the respective energy flux of a SSD for most times. Energy is accumulated at the outer parts of the ADAF until enough is stored to supply the SSD with the necessary flux. If such a situation is physically meaningful remains to be answered. The availability of ADAF-SSD transitions at low viscosity parameter α is thus inconclusive and needs further study.

8.2 The evolution of the transition radius

Our models show that the location of the transition radius R_{tr} is a function of time. Surprisingly, our models do not evolve smoothly through a series of quasi-stationary states, and neither does the transition radius change slowly. We observed two effects: (1) a slow radial drift of the transition radius, which is always directed outward and (2) rapid perturbations, during which the location of the transition moves rapidly inwards and in continuation relaxes slowly back into its undisturbed configuration. We call this behavior *oscillation event*.

The latter are most likely not due to numerical instabilities. We showed that the frequency of the oscillations, ω, is in the range expected from analysis of rotational instabilities in the transition region (Kato and Manmoto, 2000). We find that ω is near the local maximum of the epicyclic frequency κ_{max}. The value of κ_{max} depends on the relative strength of restoring and displacing forces, i.e. pressure gradient and centrifugal force, in the transition region.

The purpose of (Kato and Manmoto, 2000) was to explain the quasi-periodic oscillations (QPO), observed in a number of X-ray transients, by trapped low-frequency oscillations in the transition region. They were particularly interested in the system GRS 1915+105 which shows a QPO with varying frequency $15 \text{Hz} - 1 \text{Hz}$. Markwardt et al. (1998) suggest that the transition radius changes from $10 R_g$ to $2 R_g$ and causes the change of the QPO frequency. Kato and Manmoto (2000) noted that this would yield $\omega / \Omega_K \sim 10^{-2}$. The frequency of the oscillation events in our models are much larger $\omega / \Omega_K \sim \mathcal{O}(1)$ and cannot account for the QPO is this system (unless our models behave differently at such low transition radii).

There are two possibilities to solve this dilemma. (1) Our models also show, apart from the oscillation events, variability on larger timescales with a similar amplitude. We suspect, that this is due to higher modes of the oscillations in the transition region, though this has not been investigated in detail. Such higher

modes could very well produce a QPO of the right frequency. (2) the maximum epicyclic frequency κ_{max} is very sensitive to the gradients of angular momentum or pressure, respectively. Our models have generally low resolution in the transition region, such that the gradients are underestimated. This results in a epicyclic frequency, which is to high. Another aspect of the same problem is the procedure of vertical integration itself. It is thereby assumed that H/R is constant and the vertical integration thus commutates with derivatives with respect to R. In the transition region this assumption is obviously not satisfied and corrections to the equations are necessary. But even so, the vertical structure of the transition region can in principle not be modeled accurately with height-integrated equations. We feel that this and the modeling of convective energy transport are the weakest points of our model. Both could be remedied with 2-dimensional simulations.

The radial outward drift of the transition region is not well understood also. Narayan and Yi (1995b, and others) showed that there is an upper limit R_c to the radial extent of an ADAF. At every radius $R > R_c$, the optical depth is larger than unity and radiative transfer is efficient, such that the ADAF solution is no longer available and the flow transits to a SSD. Inward of R_c both types of solutions are available in principle. Narayan and Yi (1995b) further argued that the ADAF should extent as far as possible. That is, whenever there is an ADAF solution available at a radius R, the flow will switch to the ADAF mode. This hypothesis is known as the *strong ADAF principle*. Indeed our models do support this principle. The transition radius $R_{tr}(t)$ does always move outward until it reaches the outermost allowed location.

But why should nature prefer an ADAF over a SSD? One possible answer is related to the entropy of ADAF and SSD, respectively. For a given set of parameters, the specific entropy of the ADAF is, at any reasonable radius R, larger than the specific entropy of the SSD. If ADAF and SSD are connected at some radius, the specific entropy s will decrease outward at the interface. In our model we assumed that energy in transported along the negative entropy gradient. So the interface will always be supplied with energy from the inside. As long as this energy surplus cannot be completely shed by radiative processes, the transition region will be heated nearly to its virial temperature and the flow switches to the ADAF mode. The SSD is slowly evaporated radially at the transition to the inner ADAF. This process does not stop until radiative energy shedding in the transition region completely dominates energy supply by convection – exactly the definition of the outermost allowed transition radius.

If this picture is correct and the specific entropy gradient is indeed the driving force behind the radial drift of the transition region, then one would expect that the rate at which the transition radius R_{tr} changes, is proportional to the entropy gradient at R_{tr}, i.e.

$$\ddot{R}_{tr}(t) \propto \frac{\partial s}{\partial R_{tr}}. \tag{8.1}$$

This is currently investigated and will be published in a future work (Gracia et al., 2002).

In this context it would also be interesting to investigate if the flow properties down-stream of the transition could be related to properties up-stream of the transition by means of conserved quantities, at least in the steady limit. One of them is certainly the mass accretion rate $\dot{m}$. Another is possibly the total energy including contributions of the radiation field or some conversed energy flux. Such relations would in some sense correspond to generalized Rankine-Hugoniot relations. One could start to look for such relations at the outermost allowed location for the transition where the structure of energy budget and force balance in the transition is less complicated.

8.3 Possible transition mechanisms

The physical mechanism which causes a transition from an outer SSD to an inner ADAF, in the first place, is not subject of this work. This is a long standing issue and has been much debated in recent times, though there is upto now no conclusive theory. We will try to sketch some of the proposed models.

One idea is the vertical evaporation of the SSD (Meyer and Meyer-Hofmeister, 1994). Thereby it is assumed, that the SSD is sandwiched between a hot, friction-heated corona from above and from below. Vertical electron heat conduction could supply the cold disk with enough energy as to heat the plasma. The disk would then thicken vertically, become more tenuous and eventually the optical depth is so low, that the flow is radiative inefficient. The flow is then advection dominated. The efficiency of vertical heat transfer is a function of radius. Meyer et al. (2000) predict the maximum efficiency at some $100 R_g$. A transition farther in is inconsistent with their model. At high accretion rates, the cold disk will survive until the last stable orbit. Różańska and Czerny (2000) followed along similar tracks and investigated the conductive and radiative coupling of the hot corona with the underlying cold disk and come to very similar conclusions.

Shapiro et al. (1976) showed that the standard cool disk is thermally and viscously unstable if the total pressure is dominated by radiation rather than gas. They proposed a new hot solution (called after the authors SLE-disk), where electrons and ions have different temperatures. This solution was calculated under the assumption that radiative cooling and viscous heating still balance locally, but cooling mainly affects the electrons, while heating the ions. This solution later turned out to be thermally unstable by itself. Recently Gu and Lu (2000) proposed that the thermally unstable thin disk would not switch to the also unstable SLE solution, but rather to the stable ADAF solution. By using a bridging formula, to describe radiative cooling in the optically thick and thin case simultaneously, they were able to build global ADAF-SSD models.

Another proposal was again made by Narayan and Yi (1995b) based on the vertical structure of the standard disk. They argued, that the upper layers of a cold thin disk will always be tenuous and thus has poor radiative cooling

efficiency. If viscosity dissipates any energy in this low-density optically thin material, the gas has no way of radiating the energy and has to heat up. This is exactly the thermal instability described by Shapiro et al. (1976), but applied to the upper layers of the disk, rather than to the radial innermost region. The gas will heat to the virial temperature and switch to the ADAF accretion mode forming a differentially rotating corona onto the cold disk. Once the top layer of the disk has been boiled of in this way, the process will start anew. In this way the disk surface will be boiled off until the whole cold disk is turned into a hot ADAF. This mechanism depends on the vertical structure, in particular the viscous dissipation of the cold disk.

8.4   Concluding remarks

This work presents the first time-dependent self-consistent ADAF-SSD transition models using height-integrated equations. The physical mechanism, which makes the transition from an inner ADAF to an outer SSD possible is outward convective energy transport from the ADAF into the transition region.

Our results confirm the availability of ADAF-SSD transitions in the $(\dot{m}, \alpha_T/\alpha)$ parameter space obtained from steady state models (Manmoto and Kato, 2000). The availability of such solutions as a function of α has been studied, also. Our results indicate that the region, where the solution is available, might be larger for time-dependent models than for steady state models. We conclude that our model is at present state is fit to further explore the available parameter space, e.g. (γ, M).

Our models show for the first time explicitly that ADAF-SSD transitions are dynamically unstable. An outward decreasing specific angular momentum causes the flow to be subject to Rayleigh instabilities. Oscillating modes of frequency close to $Omega_K$ are excited in the transition region. They leak radially in to the ADAF, but do not propagate into the SSD. These oscillations give rise to rapid periodic modulations of the flow properties in the ADAF, which could possibly be identified with QPOs observed in X-Ray transient systems. At present our models seem to over-estimate the oscillation frequency. This is due to the limited numerical resolution, both radially and vertically. 2-dimensional models could drastically improve this.

Our models do also show that, though the transition is possible at a wide range of locations, the flow prefers the outermost possible radius. This confirms the "strong ADAF principle" hypothesis of Narayan and Yi (1995b). Again convective energy transfer is the clue to understanding. The SSD is radially evaporated until the transition reaches its outermost allowed location.

Our calculations treat convective energy transport in a simplified way and introduce a free parameter α_T. 2-dimensional or 3-dimensional calculations could make this parameter obsolete. This would also address uncertainties regarding the causality of diffusive nature of convective energy transport. Furthermore the vertical structure of the transition region would also become accessible.

We present a recipe to calculate simple spectra from our hydrodynamical models. These turn out to be over-simplified. Our models do not distinguish between temperature of electrons and ions, such that the resulting spectra are only qualitative estimates, but do not allow sophisticated quantitative analysis or predictions of spectral properties of ADAF-SSD transition models. For this a two temperature description is essential. Comptonization of soft photons is believed to be crucial for the complete understanding of the high-energy spectra of X-ray transients. This process can only be accurately taken into account if the vertical structure of the flow is known.

We conclude by noting, that our models accurately describe the dynamical properties of ADAF-SSD transition models. The quantitative analysis of instabilities of the transition region needs improved numerical resolution, i.e. 2-dimensional models. While quantitative analysis of the spectra of ADAF-SSD transition models need a 2-temperature description. Both extensions could in principle be done without obvious obstacles and will be initiated as future work.

Appendix A

Convection Dominated Accretion Flow

So far we have included convection as an energy transport mechanism only. But convective eddies could also transport angular momentum. Unfortunely there is upto now no consensus on how it operates. Even the direction in which angular momentum is transported – inward or outward – is under debate.

Ryu and Goodman (1992) showed that linear modes in a convectively unstable thin accretion disk transfer angular momentum inwards if the entropy in an accretion disk is stratified vertically. Kley et al. (1993); Stone and Balbus (1996) used numerical simulations to study the nonlinear version of the problem. They found that angular momentum was transported either very weakly inward or not at all. These are significant results, but their relevance to ADAFs is a little uncertain. As NY emphasized, the entropy gradient in a SSD model is in the vertical direction, whereas the angular momentum gradient in the horizontal direction. In ADAFs, on the other hand, both the entropy gradient and the angular momentum gradient are in the radial direction. This might conceivably cause some differences in the physics.

Despite these theoretical studies, the basic question of how angular momentum transport actually operates in a convective ADAF remains open (see also Klahr et al., 1999; Arlt and Rüdiger, 2001; Rüdiger et al., 2002, for recent studies on the subject). Specifically, it is unclear how important azimuthal pressure perturbations are in these systems, and whether angular momentum is transported inward or outward. Only future three-dimensional numerical simulation will answer this question. One empirical fact is worth noting; the convection zone in the Sun is closer to being in a state of constant angular velocity than a state of constant angular momentum.

Narayan et al. (2000) (hereafter NIA) studied convection angular momentum transport in ADAFs. Their first improvement was to employ mixing-length theory to determine the parameter $\alpha_T = \alpha_T(\alpha, c_0)$. Under certain assumptions α_T is no longer a free parameter, but a function of α and the temperature

T which enters through the normalization c_0^2. The second and most important improvement was to allow inward angular momentum transport. They found a totally new branch of accretion solutions, which they called convective-dominated accretion flow (CDAF). Their self-similar analytical solution will be briefly discussed here.

Following NIA we seek a self-similar solution which satisfies the following scalings for angular velocity Ω and isothermal sound speed c_s:

$$\Omega = \Omega_0 \, \Omega_K \propto R^{-3/2}, \qquad c_s^2 = c_0^2 \, v_K \propto R^{-1} \tag{A.1}$$

exactly as in the NY solution. Furthermore we allow ρ and v_R to scale as:

$$\rho = \rho_0, R^{-a}, \qquad v_R = v_0 \, R^{a-2} = v_0 \, R^{a-3/2} \, v_K, \tag{A.2}$$

where a is free parameter. The original self-similar solution is obtained if $a = 3/2$. However under appropiate conditions a very different solution is possible, which has $a = 1/2$.

In the radial momentum equation, we assume for simplicity that $v_R^2 \ll v_K^2$, which corresponds to the condition that the Shakura-Sunyaev viscosity coefficient is small $\alpha \ll 1$. This allows us to ignore the ram-pressure term $v_R \partial v_R / \partial R$ in the radial momentum equation (3.10) which then simplifies to a simple ballance between gravity, centrifugal forces and thermal pressure gradient. This gives

$$\Omega_K^2 R - \Omega^2 R = -\frac{1}{\rho}\frac{d}{dR}\rho c_s^2, \tag{A.3}$$

which leads to the condition

$$\Omega_0^2 = 1 - (a+1)c_0^2. \tag{A.4}$$

We make further use of the convective energy flux F_{trb} as defined in equations (3.23)-(3.24) and quote NIA in stating

$$K_T = \alpha_T \frac{c_s^2}{\Omega_K} = \frac{L_M^2}{4}\,(-N_{eff}^2)^{1/2}, \tag{A.5}$$

where L_M^2 is the characteristic length scale of convection and N_{eff} the effective Brunt-Väisälä frequency for a differentially rotating medium (for details see Narayan et al., 2000, and references therein). NIA find that

$$N_{eff}^2 = \left\{ -\frac{(1+a)[(\gamma+1) - (\gamma-1)a]}{\gamma}c_0^2 + 1 \right\} \Omega_K^2. \tag{A.6}$$

From this last equation it is obvious, that α_T is no longer a free parameter, but a function of c_0^2 – still to be determined – and implicitly α.

As previously discussed, transfer of angular momentum by convection is a complex subject. We consider two extreme possibilities. In one limit we assume,

that convection behaves like normal viscosity, meaning that we write the flux of angular momentum as

$$\dot{J}_T = \alpha_T \frac{c_s^2}{\Omega_K} \rho R^3 \frac{d\Omega}{dR}. \tag{A.7}$$

This corresponds to the assumption that the convective angular momentum transport is oriented down the *angular velocity* gradient, i.e. that convection tries to drive a system towards a state of uniform rotation. For $\Omega \propto \Omega_K$, it corresponds to outward transport of angular momentum. Equation (A.7) also assumes that the diffusion constant for angular momentum transport is equal to that for energy transport, hence the use of the same constant α_T. In this case the only valid self-similar solution is the one found by NY. Only the relations between the constants c_0^2, Ω_0 and v_0 are slightly modified over (3.28) - (3.30) due to the inclusion of (3.25).

An alternative possibility is that the convective angular momentum flux scales as

$$\dot{J}_T = \alpha_T \frac{c_s^2}{\Omega_K} \rho R \frac{d(\Omega R^2)}{dR}. \tag{A.8}$$

This means that the convective angular momentum flux is oriented down the *specific angular momentum* gradient, i.e. that convection tries to drive a system toward a state of uniform specific angular momentum. For $\Omega \propto \Omega_K$, it corresponds to inward transport of angular momentum. Since advection moves angular momentum inward, and since we have assumed that convection also moves angular momentun inward, the only way to have a consistent self-similar accretion solution is for α viscosity to move an equivalent amount of angular momentum outward. If the parameter α is very small ($\alpha < \alpha^c$), the viscous flux is unable to cope with the inward flux due to convection, and there is no consistent accretion solution. NIA showed that the critical value is

$$\alpha^c = \alpha_T^c = \frac{l_m^2}{20} \left(\frac{5 - 3\gamma}{\gamma} \right)^{1/2}, \tag{A.9}$$

where α_T^c is the value of the convective α_T when $\alpha = \alpha^c$. However, when α is small, a completely different solution with $a = 1/2$, $\rho \propto R^{-1/2}$ is possible. This is a *non-accreting* solution with $v_R = 0$ (at least in the limit of perfect self-similarity), which is generally referred to as "convective envelope" or "convection-dominated accretion flow" (hereafter CDAF). Figure A.1 illustrates the dependancy of α_T on α and the availability of the various solution regimes.

Since $v_R = 0$ in this solution, the advected angular momentum flux $\dot{J}_{adv}$ vanishes. Therefore we must have $\dot{J}_{vsc} + \dot{J}_T = 0$. This leads to the following condition on c_0^2:

$$\alpha = \frac{1}{3} \alpha_T = \frac{l_M^2}{27\sqrt{2}c_0^2} \left[\frac{3(\gamma + 3)}{4\gamma} c_0^2 - 1 \right]^{1/2}. \tag{A.10}$$

If α and thus α_T are very small, we have a flow which is marginally stable to convection, with $c_0^2 = 4\gamma/3(\gamma + 3)$. This last equation allows us to solve for α_c

as a function of α and γ. Interestingly, there is a consistent solution only if α is less than a critical value α^{c2}. This critical value is obtained by setting c_0^2 equal to the largest value allowed $c_0^2 = 2/3$ (as follows from equation (A.4)). This gives

$$\alpha^{c2} = \frac{1}{3}\alpha_T^{c2} = \frac{l_M^2}{36}\left(\frac{3-\gamma}{\gamma}\right)^{1/2}. \tag{A.11}$$

Note that the CDAF is technically no accretion flow at all, but rather a static configuration. In practice however the central black hole will accrete a small amount of mass from the inner parts of the convective envelope, which will have to be replenished from the outer parts and thus will drive a small amount of accretion. In contrast to the prior discussed real accretion flows, where the mass accretion rate is determined by the conditions on the outside, in the convective envelope the accretion rate is determined entirely by the conditions on the inner boundary and therefore also sensitive to the position of the inner boundary. Similar to the extended convective ADAF presented in section 3.3 the convective envelope has a significant outward flux of energy carried by convection. The energy flux is constant and originates near the center, where a fraction of binding energy of the residual accreted matter is diverted outward and transported to large radii.
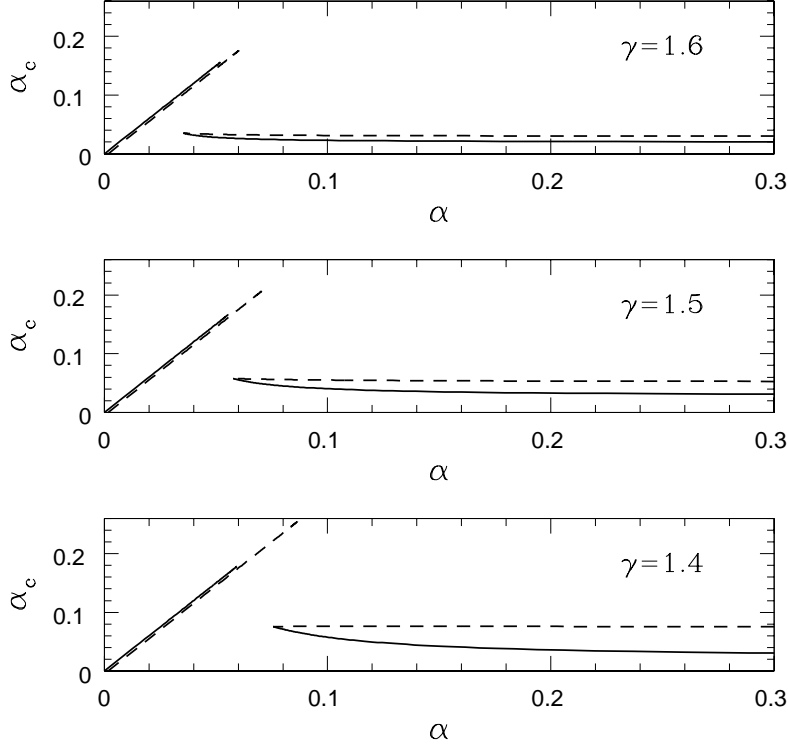
Figure A.1: Variation of the convective coefficient α_c as a function of the viscosity coefficient α for three values of the adiabatic index γ. The lines on the right refer to a solution of the self-similar form derived by NY, in which the density scales as $\rho \propto R^{-3/2}$. This solution is only available for α greater than a critical value α^c, which depends on γ. The line on the left correspond to the envelope solution discussed in the text, in which $\rho \propto R^{-1/2}$. This solution is only available for α less than a critical value α^{c2}, which again depends on γ. The solid lines correspond to the height-integrated version of the theory as used in the main text of NIA (this work also), while the dashed lines correspond to a more detailed analysis described in the appendix of NIA. Figures adopted from Narayan et al. (2000).

Bibliography

M. A. Abramowicz, I. V. Igumenshchev, and J. Lasota. A note on the conditions for SSD-ADAF transitions. *Monthly Notices Royal Astronomical Society*, 293: 443+, February 1998.

R. Arlt and G. Rüdiger. Global accretion disk simulations of magneto-rotational instability. *Astronomy and Astrophysics*, 374:1035–1048, August 2001.

R. D. Blandford and M. C. Begelman. On the fate of gas accreting at a low rate on to a black hole. *Monthly Notices Royal Astronomical Society*, 303: L1–L5, February 1999.

S. K. Chakrabarti. *Theory of transonic astrophysical flows*. Singapore: World Scientific Publication, 1990, 1990.

X. Chen, M. A. Abramowicz, J. Lasota, R. Narayan, and I. Yi. Unified description of accretion flows around black holes. *The Astrophysical Journal Letters*, 443:L61–L64, April 1995.

P. S. Coppi and R. D. Blandford. Reaction rates and energy distributions for elementary processes in relativistic pair plasmas. *Monthly Notices Royal Astronomical Society*, 245:453–507, August 1990.

J. P.. Cox and R. T. Guili. *Principles of stellar structure*, volume 1. Gorgon and Breach, New York, 1968.

T. de Zeeuw. Evidence for Massive Black Holes in Nearby Galactic Nuclei. In *Black Holes in Binaries and Galactic Nuclei*, pages 78+, 2001.

C. D. Dermer, E. P. Liang, and E. Canfield. Luminosity enhancement factor for thermal Comptonization and the electron energy balance. *The Astrophysical Journal*, 369:410–421, March 1991.

A. Eckart and R. Genzel. Stellar proper motions in the central 0.1 PC of the Galaxy. *Monthly Notices Royal Astronomical Society*, 284:576–598, January 1997.

A. A. Esin, J. E. McClintock, J. J. Drake, M. R. Garcia, C. A. Haswell, R. I. Hynes, and M. P. Muno. Modeling the Low-State Spectrum of the X-Ray Nova XTE J1118+480. *The Astrophysical Journal*, 555:483–488, July 2001.

A. A. Esin, J. E. McClintock, and R. Narayan. Advection-dominated Accretion and the Spectral States of Black Hole X-Ray Binaries: Application to Nova MUSCAE 1991. *The Astrophysical Journal*, 489:865+, November 1997.

A. A. Esin, R. Narayan, W. Cui, J. E. Grove, and S. Zhang. Spectral Transitions in Cygnus X-1 and Other Black Hole X-Ray Binaries. *The Astrophysical Journal*, 505:854–868, October 1998.

A. A. Esin, R. Narayan, E. Ostriker, and I. Yi. Hot One-Temperature Accretion Flows around Black Holes. *The Astrophysical Journal*, 465:312+, July 1996.

J. Frank, A. R. King, and D. J. Raine. *Accretion power in astrophysics.* Cambridge and New York, Cambridge University Press, 1985, 283 p., 1985.

J. Gracia. Bildung von schwarzen Löchern bei hoher Rotverschiebung. Diploma thesis, University of Heidelberg, 1998.

J. Gracia, J. Peitz, and M. Camenzind, 2002. in preparation.

W. Gu and J. Lu. Bimodal Accretion Disks: Shakura-Sunyaev Disk-Advection-dominated Accretion Flow Transitions. *The Astrophysical Journal Letters*, 540:L33–L36, September 2000.

F. B. Hildebrand. *Introduction to Numerical Analysis.* New York, McGraw-Hill, 1956.

C. Hirsch. *Numerical Computation of Internal and External Flows*, volume 1. John Wiley & Sons, 1988a.

C. Hirsch. *Numerical Computation of Internal and External Flows*, volume 2. John Wiley & Sons, 1988b.

F. Honma. Global Structure of Bimodal Accretion Disks around a Black Hole. *Publ. of the Astronomical Society of Japan*, 48:77–87, February 1996.

A. Hujeirat. IRMHD: an implicit radiative and magnetohydrodynamical solver for self-gravitating systems. *Monthly Notices Royal Astronomical Society*, 298:310–320, July 1998.

A. Hujeirat, M. Camenzind, and A. Burkert. Comptonization and synchrotron emission in 2D accretion flows. I. A new numerical solver for the Kompaneets equation. *Astronomy and Astrophysics*, 386:757–762, April 2002.

F. Hujeirat and R. Rannacher. . *Int. J. Numer. Meth. Fluids*, 28:1+, 1998.

S. Ichimaru. Bimodal behavior of accretion disks - Theory and application to Cygnus X-1 transitions. *The Astrophysical Journal*, 214:840–855, June 1977.

S. Kato. Basic Properties of Thin-Disk Oscillations. *Publ. of the Astronomical Society of Japan*, 53:1–24, February 2001.

S. Kato and T. Manmoto. Trapped Low-Frequency Oscillations in the Transition Region between Advection-dominated Accretion Flows and Standard Disks. *The Astrophysical Journal*, 541:889–897, October 2000.

S. Kato and K. E. Nakamura. Transition Radius from Cooling-Dominated to Advection-Dominated Regimes in Two Temperature Disks. *Publ. of the Astronomical Society of Japan*, 50:559–566, December 1998.

C. Keller. private communication, 2000.

C. Keller. *in preparation*. PhD thesis, University of Heidelberg, 2002.

H. H. Klahr, T. Henning, and W. Kley. On the Azimuthal Structure of Thermal Convection in Circumstellar Disks. *The Astrophysical Journal*, 514:325–343, March 1999.

W. Kley, J. C. B. Papaloizou, and D. N. C. Lin. On the Angular Momentum Transport Associated with Convective Eddies in Accretion Disks. *The Astrophysical Journal*, 416:679+, October 1993.

L.D. Landau and E.M. Lifshitz. *Fluid Mechanics*. Pergamon Press, 1959.

E. P. Liang. Multi-wavelength signatures of galactic black holes : observation and theory. *Physics Reports*, 302:67–142, 1998.

T. Manmoto and S. Kato. Transition from Standard Disk to Advection-dominated Accretion Flow. *The Astrophysical Journal*, 538:295–306, July 2000.

T. Manmoto, S. Kato, K. E. Nakamura, and R. Narayan. Dynamics of the Transition from a Thin Accretion Disk to an Advection-dominated Accretion Flow. *The Astrophysical Journal*, 529:127–137, January 2000.

T. Manmoto, S. Mineshige, and M. Kusunose. Spectrum of Optically Thin Advection-dominated Accretion Flow around a Black Hole: Application to Sagittarius A *. *The Astrophysical Journal*, 489:791+, November 1997.

C. Markwardt, J. Swank, and R. E. Taam. Variable Frequency QPOs from the Galactic Microquasar GRS 1915+105. *American Astronomical Society Meeting*, 30:1288+, December 1998.

F. Meyer, B. F. Liu, and E. Meyer-Hofmeister. Evaporation: The change from accretion via a thin disk to a coronal flow. *Astronomy and Astrophysics*, 361: 175–188, September 2000.

F. Meyer and E. Meyer-Hofmeister. Accretion disk evaporation by a coronal siphon flow. *Astronomy and Astrophysics*, 288:175–182, August 1994.

D. Mihalas and B. W. Mihalas. *Foundations of radiation hydrodynamics*. Oxford University Press, 1984.

R. Narayan, D. Barret, and J. E. McClintock. Advection-dominated Accretion Model of the Black Hole V404 Cygni in Quiescence. *The Astrophysical Journal*, 482:448+, June 1997a.

R. Narayan, I. V. Igumenshchev, and M. A. Abramowicz. Self-similar Accretion Flows with Convection. *The Astrophysical Journal*, 539:798–808, August 2000.

R. Narayan, S. Kato, and F. Honma. Global Structure and Dynamics of Advection-dominated Accretion Flows around Black Holes. *The Astrophysical Journal*, 476:49+, February 1997b.

R. Narayan, J. E. McClintock, and I. Yi. A New Model for Black Hole Soft X-Ray Transients in Quiescence. *The Astrophysical Journal*, 457:821+, February 1996.

R. Narayan and I. Yi. Advection-dominated accretion: A self-similar solution. *The Astrophysical Journal Letters*, 428:L13–L16, June 1994.

R. Narayan and I. Yi. Advection-dominated accretion: Self-similarity and bipolar outflows. *The Astrophysical Journal*, 444:231–243, May 1995a.

R. Narayan and I. Yi. Advection-dominated Accretion: Underfed Black Holes and Neutron Stars. *The Astrophysical Journal*, 452:710+, October 1995b.

I. D. Novikov and K. S. Thorne. Astrophysics of Black Holes. In C. DeWitt and B. DeWitt, editors, *Blackholes*, pages 343+, 1973.

M. Nowak and D. Lehr. Stable oscillations of black hole accretion discs. In *Theory of Black Hole Accretion Disks*, pages 233+, 1998.

A. G. Pacholczyk. *Radio astrophysics. Nonthermal processes in galactic and extragalactic sources.* Series of Books in Astronomy and Astrophysics, San Francisco: Freeman, 1970, 1970.

B. Paczynsky and P. J. Wiita. Thick accretion disks and supercritical luminosities. *Astronomy and Astrophysics*, 88:23–31, August 1980.

J. Peitz and S. Appl. Viscous accretion discs around rotating black holes. *Monthly Notices Royal Astronomical Society*, 286:681–695, April 1997.

D. Potter. *Computational Physics*. New York, John Wiley & Sons, 1973.

E. Quataert and A. Gruzinov. Constraining the Accretion Rate onto Sagittarius A* Using Linear Polarization. *The Astrophysical Journal*, 545:842–846, December 2000.

A. Różańska and B. Czerny. Vertical structure of the accreting two-temperature corona and the transition to an ADAF. *Astronomy and Astrophysics*, 360: 1170–1186, August 2000.

G. Rüdiger, R. Tschäpe, and L. L. Kitchatinov. Negative Reynolds stress generation by accretion disc convection. *Monthly Notices Royal Astronomical Society*, 332:435+, May 2002.

M. J. Rees, E. S. Phinney, M. C. Begelman, and R. D. Blandford. Ion-supported tori and the origin of radio jets. *Nature*, 295:17–21, January 1982.

H. Riffert and H. Herold. Relativistic Accretion Disk Structure Revisited. *The Astrophysical Journal*, 450:508+, September 1995.

G. B.. Rybicky and A. P. Lightman. *Radiative processes in astrophysics*. New York, John Wiley & Sons, 1979.

D. Ryu and J. Goodman. Convective instability in differentially rotating disks. *The Astrophysical Journal*, 388:438–450, April 1992.

N. I. Shakura and R. A. Sunyaev. Black holes in binary systems. Observational appearance. *Astronomy and Astrophysics*, 24:337–355, 1973.

S. L. Shapiro, A. P. Lightman, and D. M. Eardley. A two-temperature accretion disk model for Cygnus X-1 - Structure and spectrum. *The Astrophysical Journal*, 204:187–199, February 1976.

H. C. Spruit, T. Matsuda, M. Inoue, and K. Sawada. Spiral shocks and accretion in discs. *Monthly Notices Royal Astronomical Society*, 229:517–527, December 1987.

S. Stepney and P. W. Guilbert. Numerical FITS to important rates in high temperature astrophysical plasmas. *Monthly Notices Royal Astronomical Society*, 204:1269–1277, September 1983.

J. M. Stone and S. A. Balbus. Angular Momentum Transport in Accretion Disks via Convection. *The Astrophysical Journal*, 464:364+, June 1996.

J. M. Stone and M. L. Norman. ZEUS-2D: A radiation magnetohydrodynamics code for astrophysical flows in two space dimensions. I - The hydrodynamic algorithms and tests. *The Astrophysical Journal Supplement*, 80:753–790, June 1992.

R. Svensson. Electron-Positron Pair Equilibria in Relativistic Plasmas. *The Astrophysical Journal*, 258:335+, July 1982.

Y. Tanaka and N. Shibazaki. X-ray Novae. *Annual Review of Astronomy and Astrophysics*, 34:607–644, 1996.

K. S. Thorne and R. H. Price. Cygnus X-1 - an interpretation of the spectrum and its variability. *The Astrophysical Journal Letters*, 195:L101–L105, February 1975.

R. W. Wagoner. Relativistic diskoseismology. *Physics Reports*, 311:259–269, 1999.

F. Yuan, S. Markoff, and H. Falcke. A Jet-ADAF model for Sgr A*. *Astronomy and Astrophysics*, 383:854–863, March 2002.

Thank you ...